INVESTIGATION OF COHERENT STRUCTURE IN THE SIMILARITY REGION OF THE PLANAR TURBULENT JET USING POD AND WAVELET ANALYSIS

Stanislav Gordeyev

July 1999

Abstract

The coherent structure in the self-similar region of a turbulent planar jet at moderate Reynolds number was experimentally investigated by application of wavelet-based techniques and the Proper Orthogonal Decomposition (POD). Three rakes containing a total of 24 X-wire probes were used to acquire the required u', v' and w' velocity fluctuation time-series data. The measurements were performed for different spanwise separations between the rakes (i.e. different spanwise wavenumbers) at several streamwise locations. The POD technique was used to extract average coherent structures and their associated energy. Coherent structures are defined as spatial POD modes. The results show that the POD modes exhibit self-similar behavior for $x/D > 60$ (D is the nozzle width), which proves that the dynamics of the jet is self-similar. Projection of the POD modes onto instantaneous realizations of the flow field provides instantaneous shape of the coherent structure in the spatio-temporal domain. Two different kinds of structure were found in the jet: planar spanwise vortices and more complex spanwise periodic structures, topologically similar to an array of spanwise vortices. Among other things, a distinct intermittent behavior of these structures is observed. The results provide important and unique information about the topology of structures in the planar jet and lead to a better understanding of the jet physics.

Contents

List of Figures

LIST OF SYMBOLS

Roman symbols

a	dilatation parameter or scale
b	local jet half-width
c	temporal coefficient
$C(g)$	admissibility constant
C_1	virtual origin of the jet
C_2	velocity virtual origin of the jet
$CE(n)$	Cumulative Energy up to n-th POD mode
D	nozzle width
$E(a)$	energy at scale a
$E\{f\}, \overline{f}$	averaging procedure
f	frequency
$f(x)$	arbitrary continuous function
$\tilde{f}$	Wavelet transform of function f
$\hat{f}$	Fourier transform of function f
f_s	sampling frequency
F_g	Wavelet transform of function f
$FT\{f\}$	Fourier transform of function f
$g(x)$	Wavelet mother function
k	spatial wavenumber
h	step in z-direction for correlation measurements
H	separation between the rakes in three-rake experiment

k_1	jet spreading rate constant
k_2	velocity decaying rate
L_z	characteristic size of structures in z-direction
$L(\mathbf{u})$	Linear operator, acting on $\mathbf{u}$
M	number of probes per rake
n	POD mode number
N	number of resolved POD modes
N_b	number of blocks
N_p	number of measurement point per block
N_z	number of spanwise stations
N_z^e	$= 2N_z + 1$
NL	Non-linear matrix operator
$NS(\mathbf{u})$	Symbolic form for Navier-Stokes equations
$Q(\mathbf{u}, \mathbf{u})$	Quadratic operator, acting on $\mathbf{u}$
r	parameter in Morlet wavelet
R	cross-correlation matrix
$Re = UD/\nu$	Reynolds number
$RE(n)$	Relative Energy of n-th POD mode
s, s'	spatio-temporal parameter
S	Spectral cross-correlation matrix
$St = fb/U_{\max}$	Strouhal number
t, t'	temporal coordinate
T	duration of the block
T_{cor}	average time-delay of passing structures
u, u_1	streamwise velocity component
$u_{\min}$	threshold value

$\overline{u'v'}$	Reynolds stress
U_0	initial jet velocity
$U_{\max}$	local maximum velocity
U	mean u-component
v, u_2	crosstream velocity component
w, u_3	spanwise velocity component
$w(y)$	weighting function
$\mathbf{w}$	weighting vector
$\mathbf{W}$	weighting matrix
$WT\{f\}$	Wavelet transform of function f
x, x'	streamwise spatial coordinate
X_α	Fourier transform of $S_{\alpha\alpha}$ in y-direction
y, y'	crosstream spatial coordinate
z, z'	spanwise spatial coordinate

Greek symbols

α, β	indices with values 1,2,3
γ	dissipation coefficient
$\Delta t = t = t'$	temporal coordinate difference
Δy	distance between probes at one rake for two- and three-rake experiments
$\Delta y_1 = \Delta y/2$	distance between probes at one-rake experiment
$\Delta y_{\max}$	maximum allowed distance between the probes at the rake to avoid aliasing in y-direction
$\Delta z = z - z'$	spanwise coordinate difference
λ	2-rake POD eigenvalue
$\tilde{\lambda}$	non-dimensional POD eigenvalue

Λ	macroscale for velocity component
μ	1-rake POD eigenvalue
$\omega = 2\pi f$	angular frequency
$\pi = 3.14159...$	π-number
ϕ	2-rake spatial POD eigenmode
$\Phi_{\alpha\beta}$	Fourier transform of $S_{\alpha\beta}$ in z-direction
ψ	1-rake spatial POD mode
ρ_{11}	normalized cross-correlation
τ	shift parameter
θ	average slope of velocity streamlines in the first POD mode

Subscripts, Superscripts and Abbreviations

$\prime$	mean-subtracted velocity components
rms	Root-Mean-Square value of the velocity component
(n)	mode number
CS	Coherent Structure
CTA	Constant Temperature Anemometry
$Im[\ ]$	Imaginary part
POD	Proper Orthogonal Decomposition
$Re[\ ]$	Real part
VITA	Variable Interval Time Averaging
WAG	Windowed Average Gradients

ACKNOWLEDGMENTS

Chapter 1

INTRODUCTION

The fact that many turbulent flows are not completely random, but possess large-scale, spatially-correlated motions or *coherent structures* (CS) was experimentally discovered in the middle of the century (Theodorsen [136], Townsend [140], Brown & Roshko [32], Winant & Browant [147]). Since then coherent structures have been studied quite extensively and have been shown to be an important factor governing the macrocharacteristics of turbulent flows, like mass and heat transfer and mixing properties. At this juncture there is no universally agreed upon definition for the term coherent structure. For example, among others, Hussain [80], [81], [82] has introduced one possible definition of coherent structure as a connected turbulent fluid mass with instantaneously phase-correlated vorticity over its spatial extent and thereby emphasized vorticity as a characteristic measure of coherent structures. Extending Reynold's idea of decomposing turbulent flow into the mean part and the fluctuating component, he proposed a triple-decomposition of the flow into a mean flow, coherent structures and incoherent turbulence. Also he proposed possible origins of coherent structures and their time evolution as a strange attractor in phase space. Cantwell [35] in 1981 reviewed research into organized motion in different types of turbulent flows and discussed possible ways to investigate the dynamics of coherent structures. Particularly, their applications in transition and control of mixing were described.

Decomposition of the flow into a mean part, a number of coherent structures or modes and small-scale turbulence looks attractive from the point of view that it could provide a different way to describe the flow dynamics. The system can be thus modeled as a finite number of modes interacting with the mean flow, small-scale turbulence and between themselves (intermodal interactions). However, despite progress in this area, the coherent structure approach still has not generated new turbulence models that embody the coherent structure concept. One of the difficulties in using the coherent structure approach lies in limited information about coherent structures and their properties like topology, dynamics and evolution.

From the experimental point of view, coherent structure identification requires sophisticated equipment, considerable computer resources to process the large amount of experimental data required for their characterization and proper mathematical tools to interpret and analyze the results. One of the possible candidates for experimental investigation of coherent structure dynamics is turbulent jets.

Turbulent jets appear in many practical applications. Further, the simple geometry and boundary conditions make jets really attractive for fundamental investigations into turbulence. The research reported in this document will focus on the coherent structure in the planar

turbulent jet. In the following section an introduction to the structure of a turbulent planar jet is presented.

1.1 Previous studies of the structure of the turbulent planar jet

A planar turbulent jet can be divided into three regions, presented schematically in Figure 1.1. In the *initial region* closest to the nozzle exit the jet consists of two transitioning planar shear layers (with velocity ratio of unity) which bound a central core of irrotational flow (known as the potential core). As a result of sequential vortex pairing events and the associated mixing transition, the shear layers widen with downstream distance and the potential core is engulfed near $x/D \approx 4$. The near field of the planar jet is unique in that the shear layers on opposite side of the jet contain large scale, spanwise coherent vorticity of opposite sign. The merging of the shear layers near the tip of the jet potential core gives rise to a complex *interaction region* which extends to approximately $x/D = 10$ where the jet begins to reach a state dynamical equilibrium and the mean velocity profiles begin to exhibit evidence of self-similar behavior. In other words, the mean velocity profiles become congruent when scaled by the local centerline velocity $U_{\max}(x)$ and the local mean velocity half-width $b(x)$. This region is called a *self-similar region*. Since the jet decays and widens in the streamwise direction, $U_{\max}$ and b are functions x/D. Second-order moments of the velocity also exhibit self-similarly in the region, but typically the onset occurs further downstream. Well-documented measurements in planar jets are presented in Bradbury [29] and Gutmark & Wignanski [71], for instance.
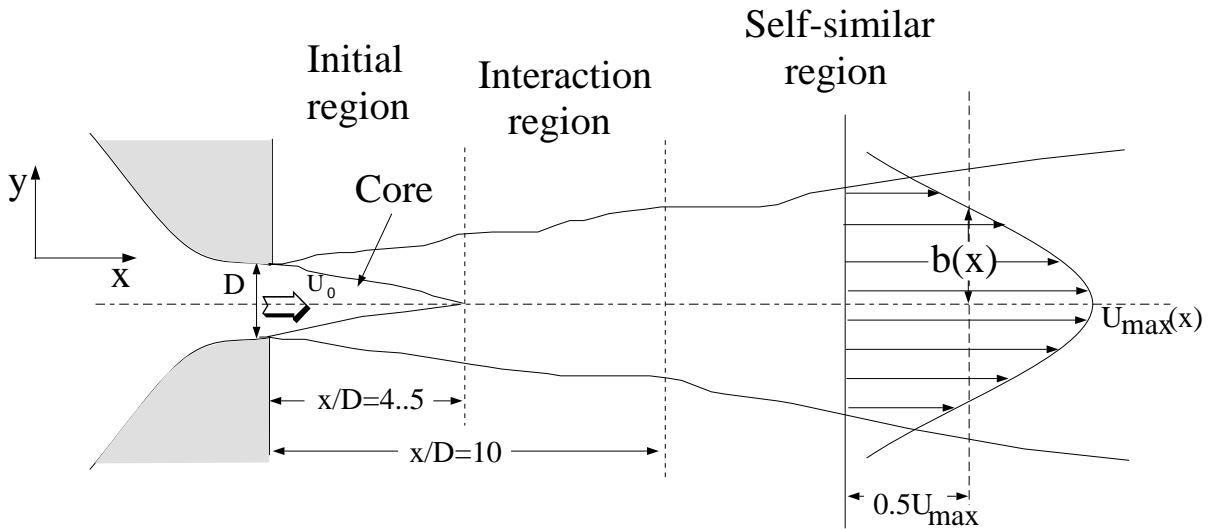
Figure 1.1: Jet regions and definition of the self-similar variables.

One of the first indications of large-scale structure in the plane turbulent jet was the "jet flapping phenomenon" first reported by Goldschmidt and Bradshaw [59] and later by Everitt and Robins [46] and Cervantes and Goldschmidt [36]. This involved the observation of negative correlation between streamwise velocity fluctuations measured simultaneously by hot-wire probes placed on opposite sides of the jet centerline. The term "flapping" is actually a misnomer

which stems from early interpretations of this phenomenon in which it was suggested that the jet flaps much as a flag does. A lateral oscillation of the mean velocity profile was proposed as the cause of the negative time-average correlation. In contrast, Oler and Goldschmidt [115] suggested that such correlation measurements are consistent with the presence of large-scale coherent structures in the similarity region of the planar jet in the form a self-preserving anti-symmetric array of counter rotating spanwise vortices. Correlation measurements by Antonia et al [7] are supportive of such an antisymmetric structural array concept and showed that the apparent flapping could indeed be explained in terms of the passage of vortical structures past the fixed probe pair and was not associated with bulk lateral displacement of the jet. Antonia et al [7] also noted that the existence of an anti-symmetric structural pattern was not in conflict with the earlier observations of both Gutmark and Wygnanski [71] and Moum Kawall and Keffer [113] which showed the independent, three dimensional random motion of the turbulent/non-turbulent interface on opposite sides of the jet. Detailed iso-correlation contour maps based on both streamwise and lateral velocity fluctuations as obtained in different jet facilities by Mumford [114], Antonia et al [8] and Thomas and Brehob [138] exhibit a remarkable likeness and appear consistent with the existence of a large-scale structural array in the planar jet similarity region. The study by Antonia et al [8] was performed in a heated jet and the existence of laterally coherent temperature fronts was used as the basis for a conditional sampling scheme. The resulting coherent structure topology inferred from this method was suggestive of an antisymmetric structural array. The temperature fronts were found to be associated with the diverging separatrix connecting adjacent structures on the same side of the jet. The contribution of the coherent and random motions to momentum and heat transport were found to be comparable. Mumford [114] used an iterative pattern recognition technique in order to investigate the topology of the large-scale structure in the turbulent plane jet. An initial structural template, whose form was motivated by conventional correlation measurements, was convolved with experimental realizations of the flow and subsequently modified as required by an optimization constraint until convergence was reached. The results suggested the existence of multiple roller-like structures whose axes extend in either the direction of mean flow homogeneity or in the direction of strain associated with the mean velocity gradient. The existence of multiple structural forms in the flow was suggested by Antonia et al [7] and Thomas and Brehob [138] to account for the limited spanwise integral macroscales in the similarity region.

Space-time correlation functions formed between streamwise or lateral component velocity fluctuations measured simultaneously on opposite side of the planar jet are found to be quasi-periodic. As such, a local time scale, τ_c, may be defined as the average time-delay between successive correlation function maxima or minima. Studies by Cervantes and Goldschmidt [36], Antonia et al [7], Thomas and Goldschmidt [139] and Thomas and Brehob [138] in different test rigs all exhibit the same constant Strouhal number,

$$\frac{b}{\tau_c U_M} = 0.1 \tag{1.1}$$

where b is the local jet mean velocity half-width and U_M is the local jet centerline velocity. This suggests that the underlying large-scale component of the flow scales in accord with the requirements for global flow similarity, i.e. that, $\tau_c \sim x^{3/2}$, where x is the streamwise spatial coordinate. More recent theoretical work performed by Ewing [48] has shown that the equations governing the propagation of the two-point velocity correlation tensor in the planar jet admit to self-similar solutions.

The convective velocity of the large-scale structural array has been estimated in studies [60], [7] and [138] using a variety of two-point measurement techniques. These studies are in general agreement, suggesting that the large-scale structural array propagates at approximately 60% of the local centerline mean velocity.

Thomas and Goldschmidt [139] considered the development of coherent structures throughout both the initial, interaction and similarity regions of the planar jet. The structures were noted to form and interact symmetrically in the transitional jet shear layers prior to the end of the potential core. Spanwise integral macroscales showed that the structures exhibit substantial two-dimensionality in the initial region. When the shear layers merged beyond the jet potential core, a restructuring of the flow was observed to occur which led to a loss in spanwise two-dimensionality on average and the formation of the self-preserving anti-symmetric structural pattern described above. Antonia et al [7] also found that structures initially formed and interacted symmetrically in the initial region, with the shear layer interaction near the tip of the jet core triggering the formation and apparent dominance of the antisymmetric structural pattern downstream. The planar jet interaction region has been the focus of detailed studies by Weir et al [145] and Browne et al [33]. The latter study characterized the redistribution of turbulence quantities in the interaction region of the plane jet as "*dramatic*" with a complex and violent interaction between initially symmetric jet shear layer vortices noted.

Although many details regarding the coherent structure's topology, origin, evolution, mutual interaction and role in the flow field dynamics are still unclear, there can be little doubt from the studies cited above that a significant coherent structure resides in the planar jet similarity region. Further, this structure appears to originate from the shear layer interaction near the tip of the jet core. The resulting structural topology may well be complex since studies have suggested both rollers aligned in the spanwise direction as well as in the direction of strain associated with the mean velocity profile.

1.2 Application of Proper Orthogonal Decomposition to extract structures

A variety of conditional sampling techniques are widely used to investigate coherent structures in flows. One shortcoming of these techniques is that they require some a priori knowledge about the shape of structure. On the contrary, the *Proper Orthogonal Decomposition (POD)*, proposed by Lumley [101], [102] provides an unconditional procedure of decomposing a flow into an infinite series of the orthogonal modes. This technique computes these modes from the velocity two point cross-correlation matrix. Thus, the shape of the modes depends on the particular flow field. The series form the most optimum set in a sense that it possess the fastest convergence among all possible orthogonal sets. In other words, that first mode contains the most possible energy, the second mode keeps the most of the energy remaining and so on. The velocity field can be represented as a sum of the modes. Because of the fastest convergence property, the number of energetically significant modes is minimum. Since there is no unique definition of the coherent structure, one can define coherent structures as POD modes, like Lumley did in [102].

If most of the energy of the flow is contained within the first few POD modes, one can use a truncated number of the POD modes as a basis set. Projecting them on the Navier-Stokes

equations, one can reduce the system of PDEs down to a low-order system of ODE's, where the rest of the modes can be modeled by a dissipative term. This low-order model can be realtively easily analyzed comparing with the original PDE system. We'll discuss this issue in detail in Chapter 8.

As the flow can be presented as a sum of interacting coherent structures, any information about the shape, origin and evolution of the structures leads to a better understanding of the underlying physics. If the number of the most energetic structures is small, a low-dimensional model of the turbulent jet can be built as a non-linear interaction between POD modes or structures. Yet, up to the author's knowledge, no research had been made to investigate *POD modes in the self-similar region of a planar turbulent jet.* One of the questions about the planar jets is as follows: Provided that all mean quantities are self-similar, is the dynamics of the planar jet in the self-similarity region self-similar as well? Are coherent structures in the jet self-similar? Theoretical work performed by Ewing [48] has shown that the equations for the evolution of the two-point correlation matrix admit self-similar solutions in the jet. This provide a necessary condition for the POD modes to be self-similar. Preliminary POD measurements done by Gordeyev & Thomas [64] has extracted large pseudo two-dimensional vortex-like POD modes existing in the region. They appear to have self-similar shapes. This reference seems to be the only application of the POD technique to investigate the self-similar region of the planar jet.

1.3   Application of wavelet transform to analyze the coherent structure

POD gives only average information about POD modes, because it is based on the time averaged velocity correlations. Projection of POD modes back to the instantaneous flow field can provide information about an instantaneous shape of the structures. In general, coherent structures appear to be well-localized in time and space and exhibit distinct intermittent behavior. One way to analyze them is to use *the wavelet transform.* In recent years the wavelet transform [69] has appeared as an extension of Fourier transform. It utilizes basis functions localized in a time-frequency domain and shows a clear superiority in investigating temporally intermittent signals. Wavelet-based temporal reconstruction of POD modes provides valuable information about instantaneous shape and dynamics of the underlying structures. For the modeling it means a fair and rigorous comparison between the model predictions and the actual temporal dynamics of structures in the jet.In the author's opinion, a proper combination of POD and wavelet transform gives a powerful way of investigating a spatio-temporal evolution of the structures existing in the planar turbulent jet.

An investigation of the dynamics of the structures leads to a better understanding of the physics of the planar jets and, as one of possible applications could provide more efficient jet control strategies. The ability to control the characteristics of jet (noise radiation, mixing properties, heat transfer, to name a few) would benefit numerous engineering applications. Despite progress in investigating the planar jet coherent structures, no dynamical models utilizing information about coherent modes in the planar jets has been constructed so far.

1.4   Thesis organization

In this thesis a rigorous experimental technique of extracting spatial information about coherent structures in a planar jet is presented. The thesis is organized as follows. Research objectives are stated in Chapter 2. A brief theory of POD and wavelet transform with short reviews of their applications in aerodynamics are given in Chapters 3 and 4. In Chapter 5 the experimental set-up and measurement techniques are presented and disscussed. In Chapter 7 the results are described. The POD modes are shown to be self-similar ones. Using the wavelet decomposition, an instantaneous topology of the structures is obtained. In Chapter 8 possible ways and potential problems of constructing a dynamical model of the planar jet in the self-similar region are outlined and briefly discussed.

Chapter 2

RESEARCH OBJECTIVES

The objective of the research is to experimentally investigate the topology and dynamics of large-scale coherent structures in the self-similar region of a planar jet using both of Proper Orthogonal Decomposition (POD) and wavelet analysis techniques. The cross-spectral matrix is experimentally measured and the POD modes are extracted by applying POD theory. *In this work coherent structures are defined as dominant POD modes.* The use of POD allows one to extract an average shape of large-scale structures. Since the jet mean characteristics reveal a self-similar behavior, the question of whether the POD modes behave in a self-similar matter arises. Similarity of the modes implies self-similarity of the jet dynamics, since the flow can be decomposed into a series of the modes. Galerkin projection of the first few most energetic and therefore the most dynamically important POD modes into governing equations gives a low-dimensional nonlinear system of equations for the temporal evolution of the modes. The optimality of POD guarantees that the number of equations is minimal. One can hope that the number of equations would be reasonably small to apply standard mathematical tools to analyze the system. Keeping more modes in the truncated expansion would lead to a greater number of equations, but provides a better description of the dynamics of the jet. One of the fundamental question is 'How many modes need to be kept in order to realistically model the jet dynamics? The proposed research will seek to answer this question.

The model describes the dynamical behavior of the jet in terms of the temporal evolution of the modes. To obtain the experimental data regarding the temporal evolution of the modes, the modes are projected back to the instantaneous velocity field, using wavelet reconstruction technique. Comparing the modeled evolution of the modes with that experimentally determined can provide a sound verification of the quality of the modeling. Also, a detailed analysis of the experimentally obtained temporal coefficients itself can provide useful information about the underlying dynamics of the structures. The wavelet transform can provide answers to questions regarding the temporal dynamics of the structures like

1. Do the structures exhibit periodic or intermittent behavior in time?

2. What is the variation in the instantaneous size of the structures?

3. Do they travel alone or in packets?

This information is vital to the turbulence modeling of the jet.

Chapter 3

BRIEF OVERVIEW OF THE PROPER ORTHOGONAL DECOMPOSITION (POD)

3.1 Basic Theory

The mathematical background behind the POD is essentially the Karhunen-Loève (KL) procedure, Karhunen [86], Loève [99]. The basic idea is to describe a given statistical ensemble with the minimum number of deterministic modes. Let $u(s)$ be a random generalized process with s as a parameter (spatial and/or temporal). We would like to find a deterministic function $\phi(s)$ with a structure typical of the members of the ensemble in some sense. One way to do it is to maximize the projection of $u(s)$ into $\phi(s)$. Mathematically, a functional in the following form needs to be maximized,

$$\frac{\left\langle |(u, \phi)|^2 \right\rangle}{(\phi, \phi)} = \lambda \geq 0 \tag{3.1}$$

where $\langle \cdot \rangle$ is the averaged or expected value, $(\cdot, \cdot)$ is a scalar product. The classical methods of the calculus of variations with a restriction $(\phi, \phi) = 1$ gives the final result for ϕ [77],

$$\int R(s, s')\phi^*(s')ds' = \lambda\phi(s) \tag{3.2}$$

The equation (3.2) is a homogeneous Fredholm integral equation of the second kind. Here $R(s, s') = \langle u(s)u^*(s') \rangle$ is an integrable cross-correlation Hermitian matrix or tensor between two points s and s' and the asterisk denotes a complex conjugate. The solution of (3.2) forms a complete set of a square-integrable orthonormal functions $\phi_n(s)$ with associated eigenvalues λ_n [108]. Any ensemble of random generalized functions can be represented by a series of orthonormal functions with random coefficients, the coefficients being uncorrelated with one another:

$$u = \sum_{n=1}^{\infty} c_n\phi_n, \quad \langle c_n c_m \rangle = \delta_{nm}\lambda_m \tag{3.3}$$

These functions are the eigenfunctions of the autocorrelation with positive eigenvalues.

The cross-correlation tensor itself can be presented in terms of the orthogonal functions as

$$R(s, s') = \sum_{n=1}^{\infty} \lambda_n \phi_n(s) \phi_n^*(s'), \tag{3.4}$$

Finally,

$$\langle (u, u) \rangle = \int R(s, s) ds = \sum_{n=1}^{\infty} \left\langle |(u, \phi_n)|^2 \right\rangle = \sum_{n=1}^{\infty} \lambda_n \tag{3.5}$$

Thus, the eigenvalues provide the energy content of the various eigenfunctions (modes). Moreover, since the modes were determined by maximizing λ (the energy of a mode), the series (3.3) converges as rapidly as possible. This means that it gives an optimal set of basis functions from all possible sets in terms of energy convergence.

If the averaging is performed in time domain, $\langle \cdot \rangle = 1/T \int_0^T (\cdot) dt$, then $u(t, \mathbf{x})$ (here t and $\mathbf{x}$ are time and space coordinates) can be represented as follows,

$$u(t, \mathbf{x}) = \sum_{n=1}^{\infty} c_n(t) \phi_n(\mathbf{x}), \tag{3.6}$$

where c's are temporal coefficients and ϕ's are the *spatial eigenfunctions or modes*.

The transformation (3.2)-(3.3) is the *POD transformation*. A more complete account of the theory can be found in [77], for instance.

Because of discretization of experimental data, a vector form of POD is widely used. In this case the integrations are replaced by a finite quadrature form. The signal u becomes an ensemble of finite-dimensional vectors, the correlation function R becomes a correlation matrix and the eigenfunctions are called eigenvectors.

On practical grounds, (3.3) or (3.6) usually is represented only in terms of a *finite* set of functions,

$$u \approx u_L = \sum_{l=1}^{L} c_l \phi_l \tag{3.7}$$

Number of modes L kept in the expansion depends on the error of approximation one is willing to accept.

3.2 Properties of POD

1. The generalized coordinate system defined by the eigenfunctions of the correlation matrix is optimal in the sense that the mean-square error resulting from a finite representation of the process is minimized. That is for any fixed L:

$$R_L = \int_0^T [u(t) - \sum_{n=1}^{L} c_n \phi_n(t)]^2 dt \to min \tag{3.8}$$

if and only if $\phi_n(t)$ are eigenfunctions of (3.2).

2. The random variables appearing in an expansion of the kind given by the equation (3.3) are orthonormal if and only if the orthonormal functions and the constants are respectively the eigenfunctions and the eigenvalues of the correlation matrix.

9

3. In addition to the mean-square error minimizing property, the POD has some additional desirable properties. Of these, satisfaction of the continuity equations is worth mentioning.

4. Algazi and Sakrison [6] show that Karhunen-Loéve expansion is optimal not only in terms of minimizing mean-square error between the signal and it's truncated representation (Property 1), but also minimizes the number of modes required to describe the signal for a given error.

5. For homogeneous directions POD modes are Fourier modes [102]. Thus, if a direction x in the flow is homogeneous, the correlation tensor between two points (x, y) and (x', y') depends only on $\Delta x = x - x'$,

$$R(x, x', y, y') = R(\Delta x, y, y') \tag{3.9}$$

and eigenmodes in x-direction are Fourier modes $\exp(ikx)$. Thus the problem (3.2) is decoupled into a set of one-dimensional problems for every Fourier wavenumber k,

$$\int \widehat{R}(y, y'; k)\varphi^*(y'; k)dy' = \lambda(k)\varphi(y; k) \tag{3.10}$$

where $\widehat{R}(y, y'; k)$ is Fourier transform of $R(\Delta x, y, y')$ in the x-direction, $\widehat{R}(y, y'; k) = \int R(\Delta x, y, y')e^{ik\Delta x}\Delta x$. The velocity decomposition (3.6) will become

$$u(x, y, t) = \sum_n \int c^{(n)}(t; k)e^{ikx}\varphi_\alpha^{(n)}(y; k)dk \tag{3.11}$$

Note that in this case φ's are known up to an arbitrary function $e^{if(k)}$, that is *the phase information in between modes is lost.* **All the phase information resides in the temporal coefficients $c^{(n)}(t; k)$. In order to find them, a projection back to an instantaneous flow is needed.** This can be done either experimentally using rakes of probes or theoretically using Galerkin projection. An example of the wavelet-based projection procedure is described in Chapter 4.

3.3   Practical applications and limitations of POD

In the case of a large number of spatial points, and consequently number of elements in the second-order correlation tensor, the approximating (3.2) or even (3.10) by a finite difference and solving the obtained matrix problem directly becomes practically impossible. Sirovich [129] pointed out that the temporal correlation matrix will yield the same dominant spatial modes, while often giving rise to a much smaller and computationally more tractable eigenproblem - *the method of snapshots.* Mathematically, for a process $u(t, x)$, instead of finding a spatial two-point correlation matrix $R_{ij} = 1/M \sum_{m=1}^{M}[u(x_i, t_m)u(x_j, t_m)]$, where N is a number of spatial points and solving (3.2) ($N \times N$-matrix), one can compute a temporal correlation $M \times M$-matrix A_{mn},

$$A_{mn} = \frac{1}{M} \int_V u(x, t_m)u(x, t_n)dx, \tag{3.12}$$

where M is number of temporal snapshots and calculate $\phi_i(x)$ from $u_m(x) = u(t_m, x)$ series as

$$\phi_i(x) = \sum_{m=1}^{M} b_{m,i} u_m(x) \tag{3.13}$$

where $b_{m,i}$'s are the solutions of the equation $\mathbf{A}\mathbf{b} = \lambda\mathbf{b}$. Usually $M \ll N$ and the computational cost of finding ϕ's can be reduced dramatically. The method of snapshots also overcomes the difficulties associated with the large data sets that accompany more than one dimension.

In [68] the limitations of POD with temporal averaging were discussed. It was shown that in this case the analysis uses only information that is close to a particular final state of the system and thus cannot be used for the system which has a several final states. Also it was pointed out that the analysis de-emphasizes infrequent events, although they could be dynamically very important (burst-like events in a turbulent boundary layer). Alternative averaging techniques were proposed and shown to be more informative in terms of investigating the system dynamics. Delville [44] pointed out that POD technique can be treated as a generalization of Fourier transform in inhomogeneous direction.

As it was pointed out before, in homogeneous directions the POD reduces to a Fourier-Stiltjes integral and gives Fourier modes as eigenmodes (Property 5). Because of an infinite span in time and/or space, these function are not well-suited to describe physically compact coherent structures (CS). Lumley [103] proposed a shot-noise method to reconstruct CS in these homogeneous direction. Recently Berkooz et al. [23] have proposed a usage of wavelets on homogeneous directions, although no clear advantage was achieved in this approach.

In an experimental context, the POD objectively extracts a complete set of spatial eigenfunctions (i.e. "modes") from the measured second-order cross correlation (or cross-spectral) matrix. The extracted modes serve as a set of optimal basis functions for expansion of the flow. The associated eigenfunctions are sometimes called *the characteristic eddies* of the turbulence field. The term was introduced by Lumley [118]. It is generally recognized that the empirical eigenfunctions extracted by POD are intimately related to the coherent structure although the exact relationship is debated. For example, it was noted by Lumley [103] that the first POD mode represents the coherent structure only if it contains a dominant percentage of the fluctuation energy. In other cases, POD modes give an optimal basis for flow decomposition but may have little to do with the physical shape of the underlying coherent structure. In this paper, we consider *the dominant POD modes as synonymous with the term coherent structure.*

Because of the large amount of computational and/or experimental work required to find the eigenvectors, the POD technique was virtually unused until the middle of the century. A historical note about POD is presented in Appendix A.1. Radical changes came with the appearance of powerful computers and the development of efficient algorithms to compute the eigenfunctions (like the method of snapshots, [129]). A really good review of POD application in turbulence can be found in [22]. A literature review on applications of POD to a variety of turbulent flows is given in Appendix A.2. As to other fields of science, POD (KL expansion) is used extensively in the fields of detection, estimation, pattern recognition [10], [54], and image processing as an efficient tool to store random processes [4], in system controls [93], [121], wind engineering [24], [25], to name just a few; because of the optimality of the expansion the KL decomposition is widely used in data compaction and reduction.

Relevant to POD techniques, conditional sampling techniques [9] are widely used to identify and describe coherent motions or structures in turbulent flows. Another unconditional extraction technique that is closely related to the POD is Linear Stochastic Estimation (LSE) [2], [3].

LSE, as well as the POD, use the cross-correlation matrix to extract structure from the flow. In [30] it is shown that LSE can be treated as a weighted sum of an infinite number of POD modes. Therefore LSE provides a representation of the coherent structure in terms of *a single characteristic flow pattern.*

The flow fields obtained from the type of conditional averages were referred by Adrian [3] to as 'conditional flow patterns', or, more briefly, '*conditional eddies*' in an effort to distinguish them clearly from physical coherent structures and 'characteristic modes' $\phi_n(\mathbf{x}, t)$ obtained from POD technique.

Chapter 4

WAVELET TRANSFORMATION

4.1 Brief theory

The wavelet transformation of the continuous signal $f(t) \in L^2(\mathbf{R})$ is defined the following way:

$$WT(\tau, a)\{f(t)\} = \widetilde{f}(\tau, a) = \frac{1}{\sqrt{a}} \int_{-\infty}^{+\infty} f(t)g^* \left(\frac{t-\tau}{a}\right) dt \tag{4.1}$$

where parameter a is called *dilatation or scale parameter*, τ is called *a shift parameter* and asterisk denotes a complex conjugate. The complex valued function $g(x)$ is called a *wavelet mother function* and satisfies the following conditions:

$$\int g(x)g^*(x)dx < \infty \tag{4.2}$$

$$C(g) = 2\pi \int_{-\infty}^{+\infty} \frac{|\widehat{g}(\omega)|^2}{\omega} d\omega < \infty \tag{4.3}$$

Here and everywhere below the hat sign ^ over a function denotes a Fourier transformation of the function,

$$\widehat{g}(\omega) = \frac{1}{\sqrt{2\pi}} \int_{-\infty}^{+\infty} g(x)e^{-i\omega x} dx \tag{4.4}$$

The condition (4.3) is called *the admissibility condition* and in the case of integrable functions $g(x)$ implies that $\int_{-\infty}^{+\infty} g(x)dx = 0$. The admissibility condition guarantees the existence of *the inverse wavelet transformation*,

$$f(t) = WT^{-1}(t)\left\{\widetilde{f}(\tau, a)\right\} = \frac{1}{C(g)} \int_{0}^{+\infty} \int_{-\infty}^{+\infty} \frac{\widetilde{f}(\tau, a)}{\sqrt{a}} g\left(\frac{t-\tau}{a}\right) \frac{da\, d\tau}{a^2} \tag{4.5}$$

Because of the local support in physical domain (4.2), the integration in (4.1) is evaluated over a finite domain, proportional to a and centered near τ. This property of the wavelet transformation allows one to analyze local characteristics of the signal at time τ and at scale a.

The wavelet transformation (4.1) can be rewritten in the Fourier space as follows

$$\widetilde{f}(\tau, a) = \sqrt{a} \int_{-\infty}^{+\infty} \widehat{f}(\omega)\widehat{g}^*(a\omega)e^{i\tau\omega} d\omega \tag{4.6}$$

and gives another highly useful interpretation of the wavelet transformation as a *multiple band-bass filtering* acting on the signal $f(t)$.

4.2 Summary of useful properties of wavelet transformation

1. Linear operator:

$$WT\{f_1 + f_2\}(\tau, a) = WT\{f_1\}(\tau, a) + WT\{f_2\}(\tau, a)$$

2. Commutative with differentiation:

$$\frac{d^n}{dt^n}[WT\{f\}(\tau, a)] = WT\left\{\frac{d^n f}{dt^n}\right\}(\tau, a)$$

3. *Parseval's theorem* - the energy of the signal can be decomposed in terms of the wavelet coefficients $\widetilde{f}(\tau, a)$ as

$$\int_{-\infty}^{+\infty} f(t)f^*(t)dt = \frac{1}{C(g)}\int_0^{+\infty}\int_{-\infty}^{+\infty}\widetilde{f}(\tau, a)\widetilde{f}^*(\tau, a)\frac{da\ d\tau}{a^2}$$

4. Energy at the scale a is defined as

$$E(a) = \frac{1}{C(g)}\frac{1}{a^2}\int_{-\infty}^{+\infty}\widetilde{f}(\tau, a)\widetilde{f}^*(\tau, a)d\tau$$

5. For any function $f(t)$ of homogeneous degree α at $t = t_0$, which is by definition $f(\lambda t) = \lambda^\alpha f(t)$ near $t = t_0$, the following property holds,

$$
\begin{aligned}
WT\{f\}(t_0, a) &= a^{\alpha+1/2}WT\{f\}\left(\frac{t_0}{a}, 1\right)\\
or \quad WT\{f\}(t_0, a) &\sim a^{\alpha+1/2} \quad as \ \ a \longrightarrow 0
\end{aligned}
$$

This property can be useful when analyzing a local continuity of the function $f(t)$. For instance, if the function is discontinuous at t_0, $\alpha = -1$.

6. The information provided by the complete set of the coefficients is *redundant*, which means there is a strong correlation between the wavelet coefficients,

$$\widetilde{f}(\tau_0, a_0) = \int\int p\left(\frac{\tau_0 - \tau}{a}, \frac{a_0}{a}\right)\widetilde{f}(\tau, a)\frac{da\ d\tau}{a^2},$$
$$where$$
$$p(\tau, a) = \frac{1}{C(g)}\frac{1}{\sqrt{a}}\int g^*\left(\frac{t - \tau}{a}\right)g(t)\ d\tau$$

This last property is not desirable when working with turbulence modeling, because it could give rise to non-physical coupling between the coefficients. One can construct the orthonormal basis of the functions $\{\psi_{ij}(x)\}$, complete in $L^2(\mathbf{R})$ and orthogonal to themselves when translated by a discrete step and dilatated by a power of 2:

$$\psi_{ij}(x) = 2^{j/2}\psi(2^j x - i)$$
$$\int \psi_{ij}(x)\psi_{kl}^*(x)dx = \delta_{ik}\delta_{jl}$$

14

The *discrete version of the wavelet decomposition*

$$f(x) = \sum_i \sum_j F_{ij} \psi_{ij}(x) , \; where$$

$$F_{ij} = \int f(x) \psi(x - 2^{-j}i)dx$$

removes the redundancy and thus minimizes the number of the wavelet coefficients F_{ij} in L^2-norm required to describe a given function $f(x)$. This transformation is attractive from computational point of view as an alternative candidate for the Fourier transformation of Navier-Stokes equations [52], [143]. the complete theory of discrete wavelet transforms can be found in [42], [43].

A variety of wavelet mother functions have been constructed as required for different applications. A few important wavelets worth of mentioning are:

Continuous wavelet transform

1. Morlet wavelet - a complex wavelet that is good for the analysis of local periodicity of a signal:
$$g(x) = \exp(irx - x^2/2) - \exp(-r^2/2 - x^2/2), \; r \geq 5$$

2. 'Mexican Hat' wavelet (Maar wavelet) - good for a search of local minima or maxima:

$$g(x) = \frac{d^2}{dx^2} \exp(-x^2/2)$$

3. First derivative of a Gaussian - localization of gradients:

$$g(x) = \frac{d}{dx} \exp(-x^2/2)$$

Discrete wavelet transform

4. Lemarie-Meyer-Battle (LMB) wavelet - explicit definition [104]

5. Daubechies compactly supported wavelet - recurrent definition [42]

Generalization of the wavelet transformation to a multi-dimensional case is straightforward ([50], for instance) and will be not discussed here.

4.3 Historical background

Historically the idea of generating the basis which possesses a locality property in both physical and Fourier spaces goes to quantum mechanics [19] and signal processing [55]. In aerodynamics an similar constructions can be found in work by Siggia [127] and Zimin [149]. In an attempt to build a model capable of predicting intermittent properties of small-scale turbulence, they proposed an algorithm of constructing a basis of *wave packets* which is local in Fourier and physical space. Independently Morlet [110], [67] applied a wavelet decomposition as a modification of Gabor elementary wavelets [55] in seismology. The first rigorous theory of wavelet

decomposition was done by Morlet and Grossmann in 1984 [69]. A discrete version of the wavelet transform was developed by Daubechies [42], [43]. An excellent presentation of wavelet theory as well as it's application in turbulence research was done by Farge in [50]. Another good reference source is the IEEE issue on wavelets [49] or Kaiser [84].

A literature review on applications of the wavelet transform in turbulent research is presented in Appendix A.3. A brief discription of other techniques similar to the wavelt transform is given in Appendix A.4.

Chapter 5

EXPERIMENTAL SET-UP

5.1 Flow-field facility

All the experiments were conducted in the planar jet facility located at the Hessert Center of the University of Notre Dame. A schematic of the facility is shown in Figure 5.1.The flow is driven by a centrifugal blower that supplies air to a cubic plenum chamber with dimensions of 1.2 m per side. Inside the plenum the air is forced to diffuse through a large layer of porous fiberglass insulation material which serves to both filter the air and decouple the flow from any blower pulsation. After leaving the plenum, the air enters a rectangular flow conditioning duct that leads to the nozzle assembly. The duct contains a section of honeycomb flow straighteners and a series of turbulence reducing screens of various mesh sizes. The jet is formed by a two-dimensional nozzle contraction that was constructed from aircraft foam which was then laminated with an acrylic material in order to achieve a smooth and polished finish. The nozzle contraction takes the form of a cubic polynomial contour with zero derivative end conditions. The nozzle has a contraction ratio of 16:1 and ends in a two-dimensional slot that is $D = 1.27$ cm in width and $H = 45.7$ cm in height giving an aspect ratio (height/width) of 36:1. It is in the longer dimension that the nozzle walls are contoured while the shorter dimension walls are flat. From the nozzle the air discharges to the surrounding ambient environment. The flow field is formed between two horizontal confining plates of dimension 2.4 m in the flow direction and 1.6 m in width which serve to keep the base flow two-dimensional in nature. Twin sheet metal face plates mounted flush with the nozzle exit plane extend laterally to the edge of the flow field and insure that entrained air enters the near field of the jet with negligible axial momentum component. All other sides of the flow field remain open. The entire setup is supported in a sturdy angle iron frame to which a computer controlled traversing mechanism is attached which provides precise hot-wire probe positioning in the three coordinate directions. A series of large screens surround the jet flow field facility in order to insure that any laboratory room air circulation has minimal effect on the planar jet flow field. It should be noted, however, that the jet was operated in a large laboratory space (353 m^2 floor area) so that any such effects on the flow were exceedingly small.

The nozzle exit velocity was $U_0 = 35$ m/sec with a corresponding Reynolds number based on nozzle slot width of $Re_D = 28,000$. The initial jet mean velocity profiles are flat (i.e. a "top-hat" shape) with the mean velocity variation across the nascent jet shear layers closely
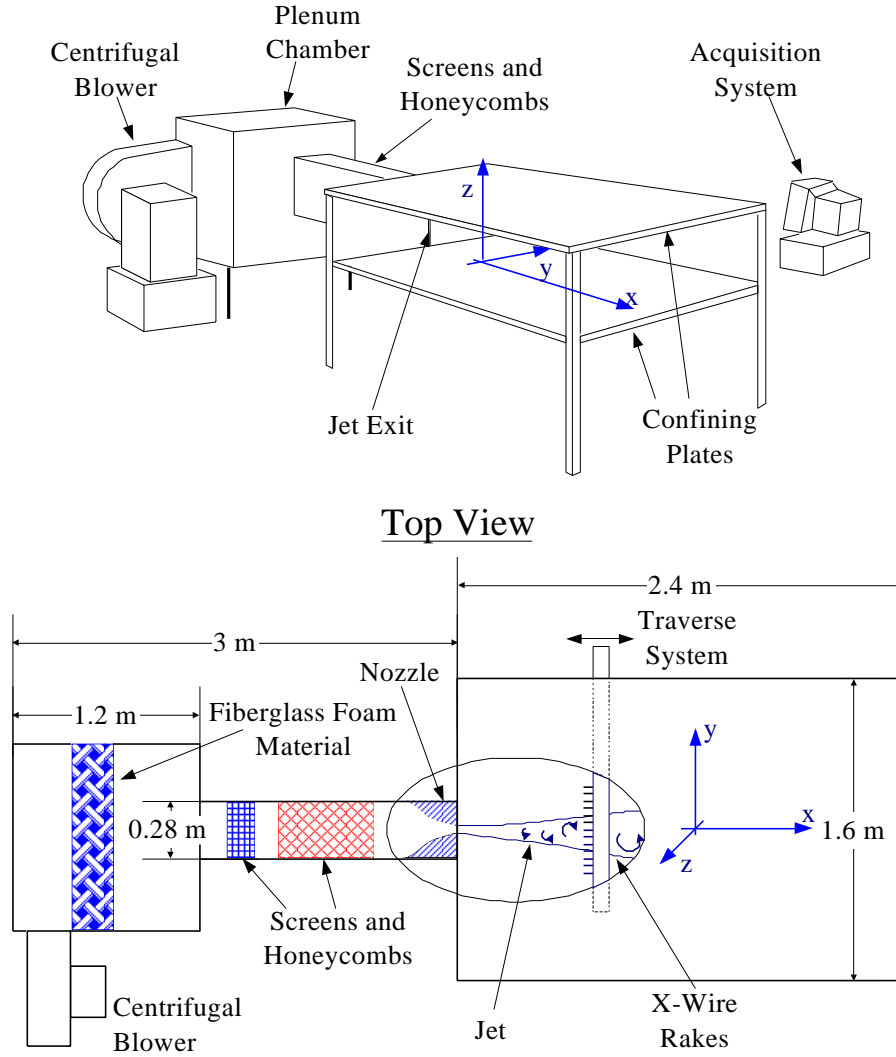
Figure 5.1: Schematic of the planar jet facility.

approximated by a classic hyperbolic tangent type of profile. The free shear layers at the nozzle lip are both laminar and have an initial momentum thickness $\theta_0 = 0.12$ mm.

The coordinate system is shown in Figure 5.1. In this thesis x will denote the streamwise spatial coordinate which is made non-dimensional by the nozzle slot width, D. The cross-stream spatial coordinate is y and is made non-dimensional by the local mean velocity half-width, $b(x)$. The half-width is defined as the distance from the jet centerline to the lateral location where the local mean velocity has fallen to one-half its centerline value. In the crosstream direction the origin $y = 0$ was taken at the centerline of the jet. The spanwise spatial coordinate extending in the direction of mean flow homogeneity is denoted z. The origin of the spanwise z-axis is chosen midway between the confining plates, with positive direction upward. The velocity components $(u_1, u_2, u_3) \equiv (u, v, w)$ correspond to the (x, y, z) coordinates, respectively.

5.2   Instrumentation

All velocity measurements were performed using constant temperature hot-wire anemometry X-wire probes allow one to measure two components of the velocity vector simultaneously at high sampling rates. The complete theory of hot-wire anemometry can be found elsewhere [61].

Up to 24 x-wires are used in the experimental work, so 48 constant temperature anemometers with low-pass filters were build in-house to reduce the cost. Appendix B provides a schematic of the electronic circuit board layout. All transducers were thoroughly tested against a commercial AA Lab Systems hot-wire anemometer and found to perform quite well within all the requirements of the experiments. The dynamic response of the transducers was found to be flat up to 50 kHz, which was sufficient for the goal of the experiments. The probes in use are hot-wire probes with "X"-orientation of two 5 μm diameter and 0.8 mm in length tungsten sensor wires inclined at 45 degrees to the probe axis (types A55P61 or AHWX-100) fabricated by Auspex Corporation. The spacing between the sensors is 0.9 mm. Each x-wire is connected by a thin co-axial cable (manufactured by Belden Wire and Cable Co., type 8700, NEC type CXC FT1) to the transducer. Output voltages from transducers are digitized by a MicroStar Laboratories simultaneous sample-and-hold Analog/Digital acquisition system MSXB. The system is capable of sampling up to 512 channels simultaneously. For 48 channels the acquisition system gives a maximum sampling rate of 33 kHz/channel with no detectable phase lag between channels. Low-pass filters on each transducer have an adjustable cut-off frequency in range 1-25 kHz. Digital data are logged to an external drive in a binary format and pre-processed on a Gateway 2000 computer with Pentium Pro 200 processor. All the primary data processing codes are written in C++ language. The data are subsequently downloaded to a SPARC Station 30 for further post-processing.

5.3   Calibration

In order to obtain the relationship between the velocity and the output voltage from the anemometer, a proper calibration of x-wires was performed. All x-wires were calibrated in the planar jet flow field facility by means of a small removable rotating table which simultaneously placed all of the x-wires into the potential core near the nozzle exit of the planar jet. See Figure 5.2 for the calibration set-up.The rotating table places all the x-wire sensors into the core of the jet, where the speed is constant. The table pivots the probes about an axis passing through the center of the X-array and thereby allows one to set a given angle between the probe axis and the oncoming uniform flow. During calibration the speed of the jet was set to 12 different values within the range from 0 to U_0 as measured by a Pitot-static probe connected to a U-tube micromanometer. The probe angle with respect to the oncoming flow was set to 11 different values within the range of -45 to $+45$ degrees. The output voltage from each anemometer was recorded for each velocity-flow angle combination. These data were used to create a look-up table to compute velocity vectors from the voltages measured during the experiment. The look-up table procedure is similar to the one described in [39] and [142]. Appendix C provides a complete description of the calibration procedure.
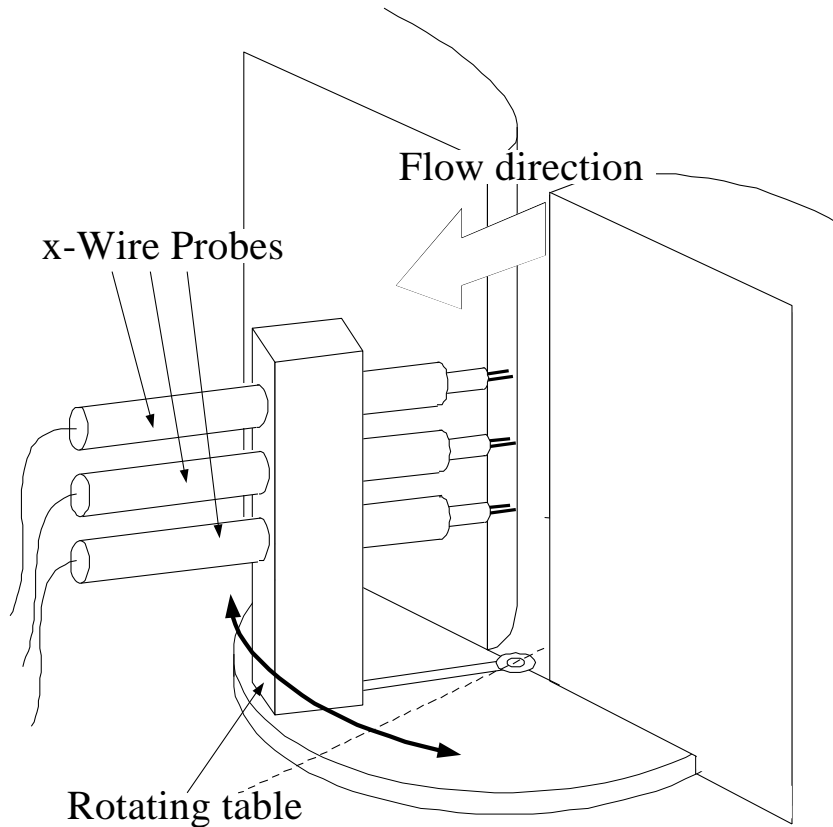
Figure 5.2: Schematic of the calibration set-up.

5.4 Flow field validation

The focus of this research is on the self-similar region of the planar turbulent jet and the measurement region spans the streamwise direction between $x/D = 50..90$. Figure 5.3a presents mean velocity profiles measured at several streamwise locations in the jet.The collapse of the profiles in the similarity coordinates U/U_{max} versus y/b is apparent. Figure 5.3b summarizes the streamwise variation of both the mean velocity half-width, $b(x)$, and the centerline velocity, $U_{max}(x)$ for the jet under investigation here. For $x/D > 10$ both quantities exhibit classic similarity scaling with $b(x)$ [1] well approximated by,

$$\frac{b}{D} = K_1 \left[\frac{x}{D} + C_1 \right] \tag{5.1}$$

with the measured *widening rate*, $K_1 = 0.1$, and the *geometric virtual origin* given by $C_1 = 0.071$. The local centerline velocity variation closely follows,

$$\left(\frac{U_{max}}{U_0} \right)^{-2} = K_2 \left[\frac{x}{D} + C_2 \right] \tag{5.2}$$

with the measured *mean velocity decay rate*, $K_2 = 0.22$, and the kinematic virtual origin $C_2 = -0.18$. These values of K_1 and K_2 are quite typical of those found in the open literature (see Chu [39] for a compilation of values). Published values for the virtual origins show considerable scatter and the study by Flora and Goldschmidt [53] has shown them to be strong functions of flow field initial conditions.
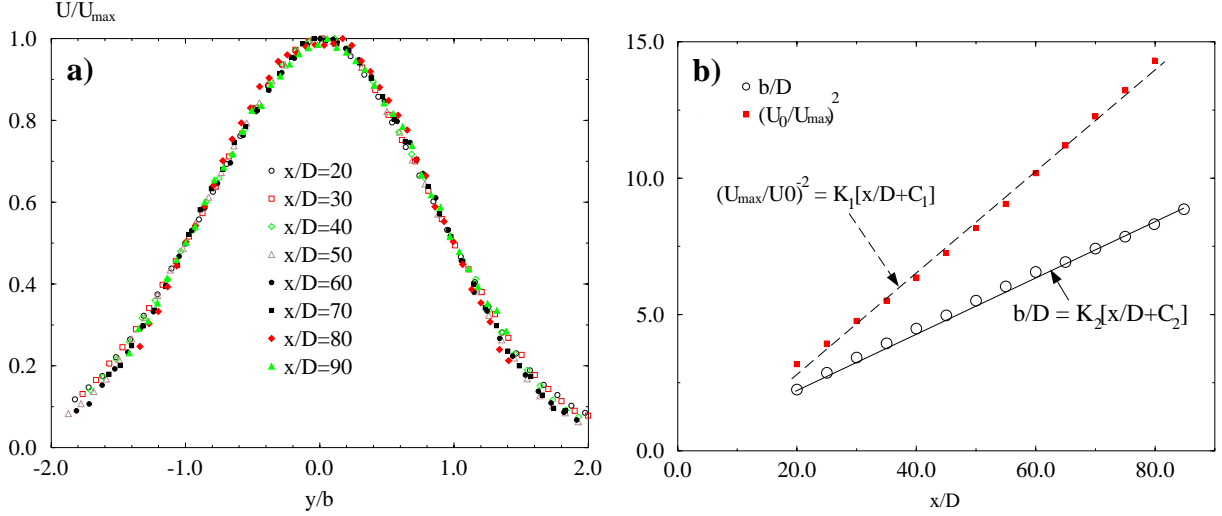
Figure 5.3: **a)** The crosstream variation of the normalized mean u-component velocity, **b)** streamwise variation of the local half-width b/D and the local maximum velocity U_{max}.
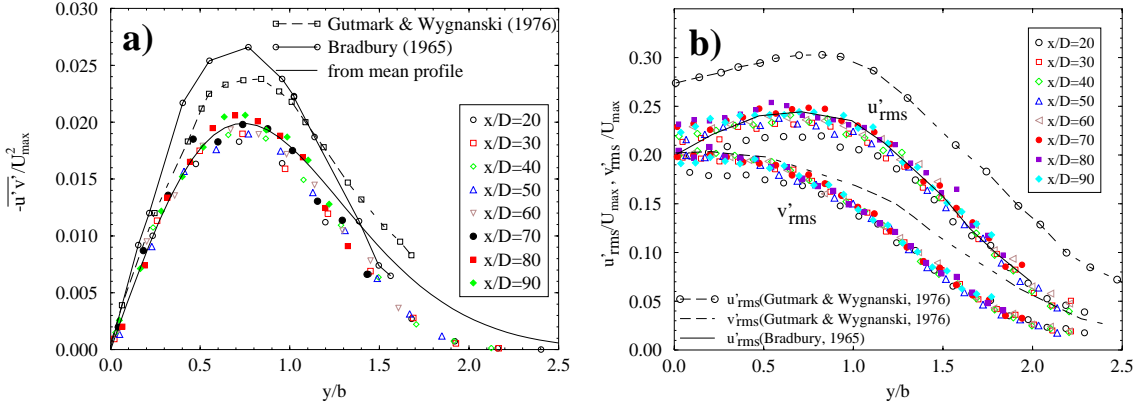
Figure 5.4: The normalized **a)** Reynolds stress $-\overline{u'v'}(x,y)/U_{max}^2(x)$ and **b)** $u'_{rms}(x,y)/U_{max}(x)$ and $v'_{rms}(x,y)/U_{max}(x)$.

It is well known that profiles of various turbulent moments typically require larger streamwise distances for the onset of self-similar behavior than does the mean velocity. Figure 5.4a presents profiles of the scaled Reynolds stress, $-\overline{u'v'}/U_{max}^2$ versus y/b as obtained at representative streamwise locations in the planar jet. Also shown for comparison are the Reynolds stress measurements of both Gutmark and Wygnanski [71] and Bradbury [29]. In addition, the Reynold's stress $-\overline{u'v'}$ is calculated from the velocity mean profile using the mass conservation and thin shear layer form of the momentum equations,

$$\frac{\partial U}{\partial x} + \frac{\partial V}{\partial y} = 0 \tag{5.3}$$

$$U\frac{\partial U}{\partial x} + V\frac{\partial U}{\partial y} = -\frac{\partial(-\overline{u'v'})}{\partial y} \tag{5.4}$$

The agreement is quite good for $y/b < 1$. Outside of this region a disparity between stress profiles is noticeable, and is most likely associated with intermittency effects near the edge of

21

the jet. Figure 5.4b presents measured profiles of scaled streamwise u_{rms}/U_{max} and lateral-component v_{rms}/U_{max} fluctuation intensities at several representative streamwise locations. From these measurements it was concluded that self-similarity for second-order statistics starts at approximately $x/D = 50$. Since the focus of this research is on coherent structure in the similarity region, the POD measurements were performed within the streamwise interval $50 \le x/D \le 90$. Although the jet facility allows measurements to be made at larger x/D, the low velocities associated with these stations give rise to larger relative uncertainties in multi-component hot-wire measurements. The streamwise range quoted above represents an optimum in the sense of achieving both self-similar jet behavior and minimal measurement uncertainty.

Chapter 6

MULTIPLE RAKE MEASUREMENTS

The experimental implementation of the POD requires the measurement of the spatial cross-correlation tensor at selected x/D locations throughout the similarity region of the jet. The process of obtaining the cross-correlation tensor is expedited by the use of cross-stream rakes of probes. This also allows one to obtain simultaneous velocity-time histories at multiple lateral locations across the jet which is also essential later if one is to reconstruct the temporal dynamics of the extracted POD eigenfunctions.

In this thesis results from three types of experiments are reported:

- The main *two-rake experiment* involves correlation measurements involving all three fluctuating velocity components at selected x/D planes in the similarity region of the jet as obtained by means of two spanwise-separated rakes of eight x-wire probes each. Both of the rakes are located at the same x/D location and are oriented in the cross-stream direction, parallel to each other. The two rakes are separated in the spanwise direction by a user selected distance Δz. The rakes are mounted on a computer-controlled traverse system which allows both their relative spanwise separation and mutual streamwise position to be controlled. The details are described in section 6.1.

- The *one-rake experiment* involved a single cross-stream rake of 16 x-wire probes. At each streamwise location investigated, this measurement was confined to a single line extending in the crosstream direction. The one-rake experiment was performed in support of the two rake experiment. By doubling the number of probes in the y-direction it allowed examination of spatial aliasing in the inhomogeneous coordinate, with the results presented in section 6.2. In addition, since many previous studies of the planar turbulent jet have focused on measurements in a fixed $x - y$ plane, it seems appropriate to compare POD eigenmodes extracted from the one and two-rake experiments. See section 6.3 for further details.

- The set of *three-rake measurements* was conducted to obtain a time record of velocity components. It allows one to investigate the shape of coherent structure in physical space by projecting the dominant POD modes onto the instantaneous velocity field. A description of the experimental procedure is given in section 7.7.

6.1 Two-rake experiments

6.1.1 Two-rake set-up

Measurements of (u, v) and (u, w) fluctuation velocity components at several planes $x/D = 50, 60, 70, 80, 90$ were done by using two rakes of x-wires with $M = 8$ evenly spaced probes on each rake. Due to a similarity in basic flow field geometries, our approach is patterned after that developed and successfully implemented by Ukeiley and Glauser [142], [45] for their study of the plane mixing layer. Figure 6.1 presents a schematic and photograph of these two x-wire rakes in the planar jet facility.
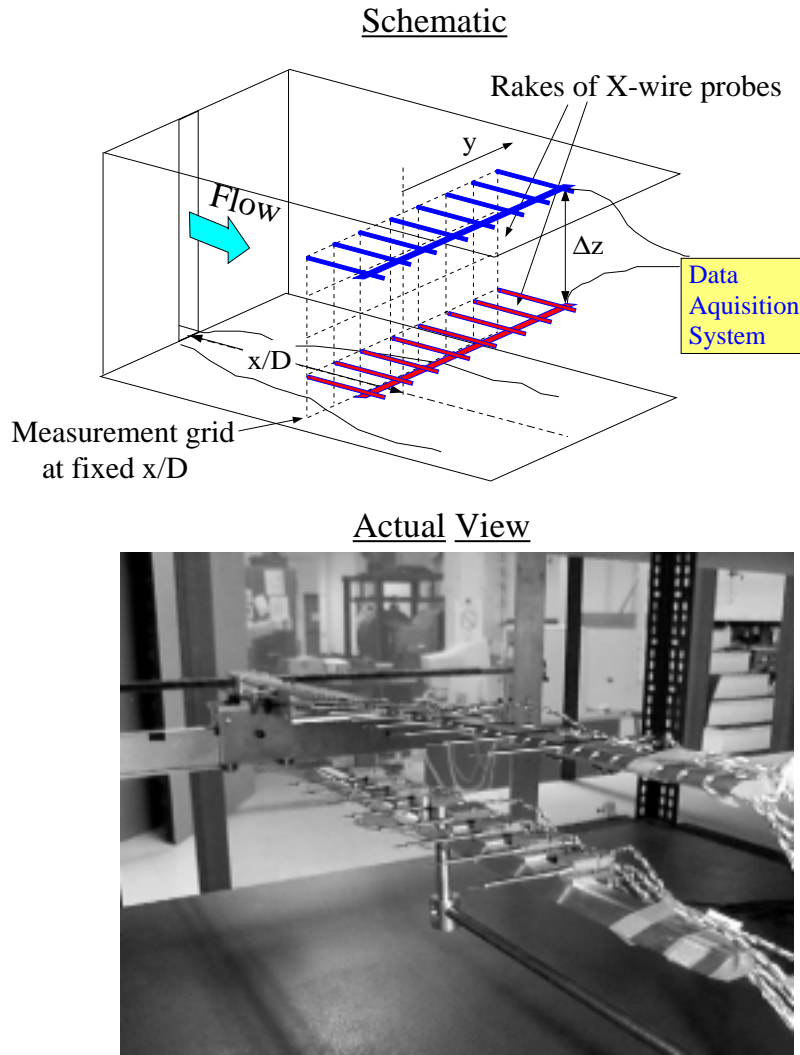
Figure 6.1: Orientation of the rakes in two-rake experiment.

Both rakes are positioned at the same streamwise location and are oriented in the cross-stream direction, parallel to each other. One rake is positioned on a manual traverse and another one is mounted on a computer-controlled traverse system. The traverse system allows one to control the location of the second rake with respect to the first one in the spanwise direction. Also both traverses move the rakes in the streamwise direction. Probes on rakes are aligned

24

in the streamwise direction and evenly spaced with $\Delta y = 5$ cm. One rake is centered between the confining plates, which corresponds to $z = 0$. The second rake is positioned below the first rake at $N_z = 15$ different equally spaced z-locations with the step $h = 1.9$ cm. Temporal and spatial aliasing issues are discussed in details in section 6.2. All x-wire sensors are oriented horizontally or vertically to measure either (u, v) or (u, w) components of the velocity vector, respectively.

6.1.2   Calculation of correlation matrices and POD modes

In this section we describe the basic procedure by which the POD eigenmodes and associated eigenvalues, introduced in Chapter 3 are extracted from the two rake experiment.

Correlation measurements involving the (u, v) and (u, w) velocity components were performed at several planes of constant x/D over the streamwise range $50 \leq x/D \leq 90$. We denote the cross-correlation tensor as,

$$R_{\alpha\beta}(y, y', z, z', t, t') = \langle u_\alpha(y, z, t)\, u_\beta(y', z', t')\rangle, \tag{6.1}$$

where $\langle \cdot \rangle$ denotes an ensemble average and Greek subscripts denote a fluctuating velocity component u, v or w. The velocity measurement $u_\alpha(y, z, t)$ corresponds to the first rake and $u_\beta(y', z', t')$ corresponds to the second. Because the flow is stationary in time and is assumed homogeneous in the spanwise direction (z), the cross-correlation matrix $R_{\alpha\beta}(y, y', z, z', t, t')$ depends on the relative coordinates $\Delta z = z - z'$ and $\tau = t - t'$. Using the property 5, Section 3.2, we perform the Fourier transform of $R_{\alpha\beta}$ *in time*,

$$S_{\alpha\beta}(y, y', \Delta z, f) = \int R_{\alpha\beta}(y, y', \Delta z, \Delta t)e^{-2\pi i f \Delta t}d\Delta t, \tag{6.2}$$

One can show that the cross-correlation matrix can be computed from Fourier Transforms of the individual velocity signals (Bendat & Pierson [21]),

$$S_{\alpha\beta}(y, y', \Delta z, f) = \lim_{T \to \infty} \frac{1}{T}\langle \hat{u}_\alpha^*(y, z, f)\hat{u}_\beta(y', z + \Delta z, f)\rangle \tag{6.3}$$

where $\hat{u}_\alpha(y, z, f) = \int_0^T u_\alpha(y, z, t)e^{-2\pi i f t}dt$ is Fourier transformation of the velocity vector for each block, T is a duration of the block and the asterisk denotes a complex conjugate. The x-wire probes are capable of measuring simultaneously either (u, v) or (u, w) components of velocity, therefore α and β are 1&2 or 1&3 respectively. The next step is to perform a *spatial* Fourier transformation in the homogeneous z-direction to get

$$\Phi_{\alpha\beta}(y, y'; f, k_z) = \int S_{\alpha\beta}(y, y', \Delta z, f)e^{-2\pi i k_z \Delta z}d(\Delta z), \tag{6.4}$$

where k_z is a spanwise wavenumber. This spectral correlation tensor will be a kernel in the integral equation to find POD modes for different f and k_z (see [102] or [77] for details),

$$\int \Phi_{\alpha\beta}(y, y'; f, k_z)\varphi_\beta^{(n)}(y'; f, k_z)dy' = \lambda^{(n)}(f, k_z)\varphi_\alpha^{(n)}(y; f, k_z) \tag{6.5}$$

Thus, the problem of finding POD modes is reduced to a set of one-dimensional integral equations (6.5) with f and k_z as parameters. The solution of (6.5) gives a complete set of orthonormal

eigenfunctions $\varphi_\alpha^{(n)}(y; f, k_z)$ with positive eigenvalues $\lambda^{(n)}(f, k_z)$. Any velocity realization can be represented as a sum of the eigenvalues,

$$u_\alpha(y, z, t) = \sum_{n=1}^{\infty} \int \int c(f, k_z) \varphi_\alpha^{(n)}(y; f, k_z) \exp(2\pi i f t) \exp(2\pi i k_z z) \, df \, dk_z \qquad (6.6)$$

The spectral correlation tensor $\Phi_{\alpha\beta}(y, y'; f, k_z)$ also can be expanded in terms of POD modes, similar to (3.4),

$$\Phi_{\alpha\beta}(y, y'; f, k_z) = \sum_{n=1}^{\infty} \lambda^{(n)}(f, k_z) \varphi_\alpha^{(n)}(y; f, k_z) \left\{ \varphi_\beta^{(n)}(y'; f, k_z) \right\}^* \qquad (6.7)$$

Finally, the eigenvalues $\lambda^{(n)}(f, k_z)$ represent the energy distribution of each POD mode in a frequency-wavenumber space.

6.1.3 Symmetries of S-matrix

Before considering details regarding the practical implementation of the above relationships, it is useful to point out certain symmetries possessed by the cross-spectral tensor when measured in the planar jet flow field. By the term "symmetries" we mean certain transformations of the physical variables which leave the flow invariant. Consideration of these symmetries leads to a simplification of the experiment. The particular symmetries in the planar jet worth mentioning are:

1. Invariance with respect to translations in both homogeneous directions: time and z-direction,

$$t \rightarrow t + const, \ z \rightarrow z + const \qquad (6.8)$$

   This property was used to simplify the multi-dimensional integral equation (3.2) to a number of one-dimensional integrals (6.5).

2. Reflections in the z-direction,

$$z \rightarrow -z, \ u \rightarrow u, \ v \rightarrow v, \ w \rightarrow -w \qquad (6.9)$$

   Application of (6.9) to (6.4) gives the following property of the cross-spectral matrix $S_{\alpha\beta}$,

$$S_{\alpha\beta}(y, y', \Delta z, f) = \pm S_{\alpha\beta}(y, y', -\Delta z, f), \qquad (6.10)$$

   where the minus sign should be chosen if either α or β is equal to 3, but not both. This symmetry allows one to restrict the measurements of the S-matrix to positive Δz only, which reduces the required data collection at a given streamwise location by a factor of two.

3. Physical symmetry in the y-direction,

$$y \rightarrow -y, u \rightarrow u, \ v \rightarrow -v, \ w \rightarrow w$$

   leads to following equality,

$$S_{\alpha\beta}(y, y', \Delta z, f) = \pm S_{\alpha\beta}(-y, -y', \Delta z, f). \qquad (6.11)$$

   The minus sign is chosen if α or β is equal to 2. Equation (6.11) says that the $S_{\alpha\beta}$-matrix exhibits a central symmetry about the origin $y = y' = 0$.

4. Symmetry with respect to the interchange of the probe pair,

$$
\begin{aligned}
(y, z) \quad &\leftrightarrow \quad (y', z') \\
S_{\alpha\beta}(y, y', \Delta z, f) \quad &= \quad S_{\alpha\beta}^{*}(y', y, -\Delta z, f)
\end{aligned}
\tag{6.12}
$$

For $\Delta z = 0$, this property implies that the $Re\{S_{\alpha\alpha}\}$ is symmetrical about the line $y = y'$, while $Im\{S_{\alpha\alpha}\}$ is antisymmetric. Combining (6.10) and (6.12), one can show that diagonal terms of the S-matrix are Hermitian, that is, $S_{\alpha\alpha}(y, y', \Delta z, f) = S_{\alpha\alpha}^{*}(y', y, \Delta z, f)$.

6.1.4 Numerical calculation of the Φ-matrix

A discrete windowed Fourier transform [21] of the digitized time-series velocity fluctuation data was used to compute (6.3),

$$
\begin{aligned}
\hat{u}_{\alpha}(y, z; n\Delta f) \quad &= \quad \Delta t \sqrt{\frac{8}{3}} \sum_{k=0}^{N_p - 1} w(k, N_p)\, u_{\alpha}(y, z; k\Delta t) \exp(-2\pi i k n / N_p), \\
n \quad &= \quad 0..N_p - 1
\end{aligned}
\tag{6.13}
$$

where Δt is the sampling interval, $\Delta f = 1/T = f_s/N_p$, f_s is the sampling frequency, $N_p = 2^p$ is the number of points per data block, T is the data block time duration and $w(k, N_p)$ is a suitably chosen windowing function to suppress side lobe spectral leakage. A number of windowing functions were tried early on with the best results obtained with the Hanning window [21],

$$
w(j, N) = 1 - \cos^2(j\pi/N), \quad j = 0..N - 1
\tag{6.14}
$$

which was selected for use in this study. The factor $\sqrt{8/3}$ appearing in (6.13) properly accounts for the signal content lost in the windowing process. In order to compute $\Phi_{\alpha\beta}(y, y'; f, k_z)$ via (6.4), the S-matrix was extended to negative Δz's by application of (6.10) and a discrete spatial Fourier transform was performed with a Hanning weighting function (6.14) to obtain,

$$
\begin{aligned}
\Phi_{\alpha\beta}(y, y'; n\Delta f, m\Delta k_z) \quad &= \quad \Delta z \sqrt{\frac{8}{3}} \sum_{k=-N_z}^{N_z} w(k, N_e)\{\pm S_{\alpha\beta}(y, y', kh, n\Delta f)\} e^{-2\pi i k m / N_e}, \\
m \quad &= \quad 0..(N_e - 1)
\end{aligned}
\tag{6.15}
$$

where $N_e = 2N_z + 1$, N_z is the number of z measurement locations at a fixed streamwise location, h is the spatial step size between consecutive z-locations, $\Delta k_z = 1/(N_e\, h)$. Again, only the first $(2N_z + 1)/2 = N_z$ points $m = 0.. N_z - 1$ are given unambiguously. A Fast Fourier Transform algorithm [21] was used compute both (6.13) and (6.15).

6.1.5 Numerical calculation of POD modes

The $\Phi_{\alpha\beta}$-correlation tensor is known at finite, equally spaced experimental points $\{y_i\}$, $i = 1, .., M$, where M is the number of the probes on one rake; for two-rake and three-rake experiments $M = 8$ and for one-rake experiment $M = 16$. Hence all the integrals (6.5) should

be replaced with a finite quadrature form. Appendix D provides the details on the numerical integrating procedure. The finite approximation of the integration (6.5) for M-vector $\varphi = \{\varphi(y_i)\}_{i=1}^{M}$ can be written in the following form,

$$\sum_{j=1}^{M} \Phi_{\alpha\beta}(y_i, y_j; f, k_z) w(y_j) \varphi_\beta^{(n)}(y_j; f, k_z) \Delta y = \lambda^{(n)}(f, k_z) \varphi_\alpha^{(n)}(y_i; f, k_z) , \qquad (6.16)$$

$$or \qquad \mathbf{\Phi}_{\alpha\beta} \mathbf{W} \varphi_\beta = \frac{\lambda}{\Delta y} \varphi_\alpha, \qquad (6.17)$$

where the $\mathbf{W}$-matrix is a *weighting* $[M \times M]$ matrix,

$$\mathbf{W} = \{\overbrace{\mathbf{w}, \; ..., \mathbf{w}}^{M-columns}\}, \quad \mathbf{w} = (0.5, \overbrace{1, 1, .., 1}^{M-2}, 0.5)^T \text{ -trapezoidal weighting } M\text{-vector,}$$

$\mathbf{\Phi}_{\alpha\beta} = \{\Phi_{\alpha\beta}(y_i, y_j; f, k_z)\}_{i,j=1}^{M,M}$ is the $[M \times M]$ Hermitian matrix and Δy is the spacing between probes in the rake. After multiplication the $\mathbf{\Phi}\mathbf{W}$-matrix is no longer a Hermitian matrix. Let's multiply (6.17) by $\mathbf{W}^{1/2}$ from the left and make some rearrangements,

$$\mathbf{W}^{1/2} \mathbf{\Phi}_{\alpha\beta} \mathbf{W} \varphi_\beta = \left(\mathbf{W}^{1/2} \mathbf{\Phi}_{\alpha\beta} \mathbf{W}^{1/2}\right) \left(\mathbf{W}^{1/2} \varphi_\beta\right) = \frac{\lambda}{\Delta y} \left(\mathbf{W}^{1/2} \varphi_\alpha\right)$$

$$or \qquad \widetilde{\mathbf{\Phi}}_{\alpha\beta} \; \widetilde{\varphi}_\beta = \frac{\lambda}{\Delta y} \widetilde{\varphi}_\alpha \qquad (6.18)$$

Now the $\widetilde{\mathbf{\Phi}}_{\alpha\beta} = \mathbf{W}^{1/2} \mathbf{\Phi}_{\alpha\beta} \mathbf{W}^{1/2}$ is a Hermitian matrix with $\lambda/\Delta y$ and $\widetilde{\varphi}_\alpha = \mathbf{W}^{1/2} \varphi_\alpha$ the corresponding eigenvectors and eigenvalues.

The matrix (6.18) was solved using the Hermitian Matrix Solver from the IMSL library for UNIX systems. After a back transformation $\varphi_\alpha = \mathbf{W}^{-1/2} \widetilde{\varphi}_\alpha$, a finite set of M orthogonal spatial modes at the discrete spatial points $\varphi_\alpha^{(n)}(y_i; f, k_z)$ with the corresponding eigenvalues $\lambda^{(n)}(f, k_z)$ are obtained.

Since the $\mathbf{\Phi}$-matrix is known only at discrete points in frequency-wavenumber space, $(f, k_z) = \{(n\Delta f, m\Delta k_z)\}$, $n = 0..N_p/2 - 1$, $m = 0..N_z - 1$, then $\lambda^{(n)}(f, k_z)$ and $\varphi_\alpha^{(n)}(y_i; f, k_z)$ are known at discrete points too. The number of eigenmodes that can be resolved is limited by the need to avoid spatial aliasing as described by Glauser and George [58]. In this experiment it is found that m probes generally allow $m/2$ modes to be resolved although this also depends on the particular velocity component considered. Spatial and temporal aliasing issues are addressed in the next section.

6.2 Aliasing issues

The acquired data is discrete in both time and space and therefore careful consideration must be given to avoid temporal and spatial aliasing. Avoidance of aliasing in the homogeneous directions is straightforward and is considered first.

6.2.1 Aliasing in z-direction

When measuring correlations in the z-direction, questions arise regarding how many points to choose and what spatial separation to take. The more points we use, the better resolution we

have. On the other hand, each measurement point requires both a considerable amount of time to measure and storage space to save the data. So, the number of points in z-direction should be rationally minimized without a considerable loss of accuracy and resolution in measurements through aliasing. In the two-rake experiment, the traverse system allows one to control the spanwise position of the second rake with respect to the first. At each streamwise location investigated, one rake is placed in the $x - y$ centerplane midway between the flow field confining plates, which corresponds to $z = 0$. The second rake is sequentially positioned below the first rake at $N_z = 15$ different equally spaced z-locations. In order to establish the appropriate z increment for these measurements (which we denote as h), consideration was given to the character of the spanwise correlation coefficient function,

$$\rho_{11}\left(\Delta z\right) \equiv \frac{\overline{u(y,z)u(y,z+\Delta z)}}{\overline{u^2}(y,z)} \tag{6.19}$$

at $y/b = 0$ for $x/D = 70$.

Figure 6.2a presents a sample correlation coefficient function as obtained at $x/D = 70$ for 40 equally spaced z-locations with a step size of 4.5 mm. This step provides a maximum resolved wavenumber $k_z^{(\max)} = 111$ m^{-1}. The probe separation Δz is made non-dimensional with the local mean velocity half-width. A spatial Fourier transform of the correlation coefficient function yields a cross-spectral density function of spanwise wavenumber k_z.

$$F_{11}(k_z) = \int \rho_{11}(\Delta z) \exp(-2\pi i k_z z) dz \tag{6.20}$$

Figure 6.2b presents $F_{11}(k_z)$ corresponding the $\rho_{11}\left(\Delta z\right)$ of Figure 6.2a. From this figure one observes that there is little spanwise correlation for $k_z b > 2$. Defining $k_z^{max} \equiv 2/b$ we then require that h satisfy the Nyquist constraint,

$$k_z^{max} \leq \frac{1}{2h}. \tag{6.21}$$

This gives the requirement that $h \leq 0.21b$. The selected value of the stepsize in the z-direction was chosen to be $h = 1.91$ cm for all streamwise stations. This stepsize in z satisfies the Nyquist constraint over the range $50 \leq x/D \leq 90$. For example, at $x/D = 70$, $h \approx 0.19b$.

6.2.2 Macroscales in z-direction

From correlation measurements, other flow characteristics like macroscales can be calculated. The integral macroscale value for u-component is defined as $\Lambda_z^{(u)} = \int_0^\infty \rho_{11}(\Delta z) d(\Delta z)$ and is found to be approximately $\Lambda_z^{(u)}/b = 0.22$. This has been observed by other investigators (e.g. Everitt and Robins [46], Antonia et al [7] and Thomas and Brehob [138]). The other macroscales at $y/b = 0$ are calculated, $\Lambda_z^{(v)}/b = 0.6$, $\Lambda_z^{(w)}/b = 0.32$. Similar macroscales values are reported in [46], [7].

6.2.3 Temporal aliasing

For the conditions under which the jet was operated, conventional power spectra reveal that the frequency bandwidth for the fluctuating velocity extends to approximately 5 kHz. In order to avoid temporal aliasing and to satisfactorily characterize the turbulence, this would
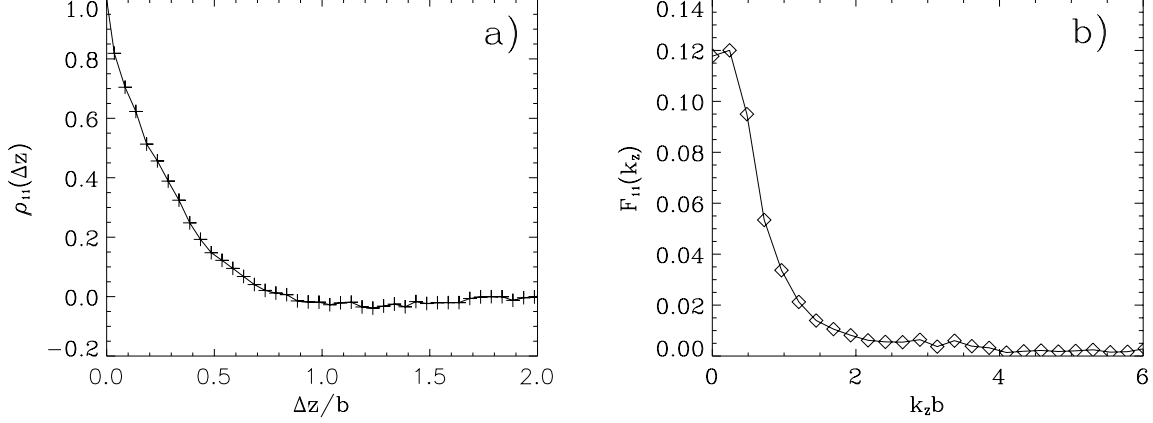
Figure 6.2: **a)** Normalized correlation of u-component in z-direction $\rho_{11}(\Delta z)$ and **b)** it's Fourier transform $F_{11}(k_z)$ at $y = 0$ for $x/D = 70$.

dictate a sampling frequency for conventional turbulence measurements of approximately 10 kHz.However, since the focus of this experiment is on *the large-scale structure* in the flow
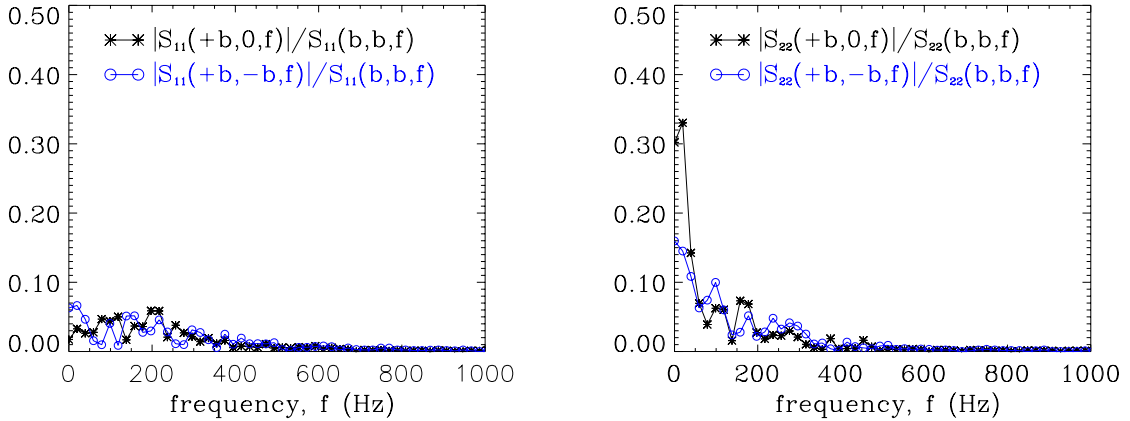
Figure 6.3: Normalized spectral cross-correlations $|S_{11}(+b, y', f)|/S_{11}(b, b, f)$ and $|S_{22}(+b, y', f)|/S_{22}(b, b, f)$ between two probes for $y' = 0, -b$ at $x/D = 70$.

which is investigated via cross-spectral methods, it will be shown that a much lower sampling frequency combined with the use of analog anti-alias filters offers the best approach. Converged cross-spectral density functions $S_{\alpha\alpha}(y, y'; f)$ obtained with a sampling frequency of $f_s = 10$ kHz at a variety of locations in the jet similarity region show that significant correlation is restricted to much lower frequencies, even for the smallest cross-stream probe spacing. As an example Figure 6 presents both $|S_{11}(+b, y'; f)|/S_{11}(b, b; f)$ and $|S_{22}(+b, y'; f)|/S_{22}(b, b; f)$ as obtained for $y' = 0, -b$ at $x/D = 70$. Note that there is virtually no spectral coherence for frequencies $f > 400$ Hz. From this figure (and others that are not presented here) it can be seen that the spatially coherent structures lie at comparatively low frequencies, so the use of relatively low sampling rates is justified for two point correlation measurements. In general,

it is found that the cross-spectral functions exhibit little correlation for local nondimensional frequencies $fb/U_{max} > 1$. Consequently, the local non-dimensional sampling frequency for the experiments was set at

$$St = f_s b/U_{max} = 8.0. \tag{6.22}$$

From (6.22) and using (5.1) and (5.2), the streamwise dependence of the sampling frequency is $f_s(x/D) = 170 \, U_0/D \, (x/D)^{-3/2} = 4.7 \cdot 10^5 (x/D)^{-3/2}$ (Hz). The numerical values at experimental streamwise locations are presented in Table 6.1.

Table 6.1: Sampling frequencies at the measurement streamwise locations.

x/D	50	60	70	80	90
f_s (Hz)	1300	1000	800	650	550

For the range of x/D investigated in this experiment the sampling frequency varied from 1.3 kHz at $x/D = 50$ to 0.55 kHz at $x/D = 90$. In each case the cutoff frequency of the anti-alias analog filters was set to $f_s/2$ in order to prevent *temporal* aliasing.

6.2.4 Spatial aliasing in inhomogeneous direction

The two rake experiment uses 8 x-wire probes (per rake), equally spaced in the inhomogeneous y direction with $\Delta y = 5$ cm. In order to assess and minimize the degree of spatial aliasing in the y direction, use was made of a single rake experiment with 16 equally spaced x-wires across the jet. Thus the spacing between probes was half that for the two-rake case, $\Delta y_1 = \Delta y/2 = 2.5$ cm. In order for the two-rake experiment to correctly resolve the cross-spectral matrix in the y-direction, the spatial Nyquist wavenumber $k_y^{(N)} = 1/(2\Delta y)$ must be greater than the maximum wavenumber exhibiting non-zero lateral spatial correlation. At each x/D location the cross-spectral density $S_{\alpha\alpha}(y, y', St)$ (where $St = fb/U_{max}$) was computed between all probe pairs. For the 16 probe rake this represents a total of 120 cross-spectral measurements at each streamwise location for each combination of velocity components S_{11}, S_{22} and S_{33}. A spatial Fourier transform of the resulting cross-spectra for each y-position is calculated as $|X_\alpha|^2(k_y, y, St) = |X_\alpha(k_y, y, St)X_\alpha^*(k_y, y, St)|$, where

$$X_\alpha(k_y, y, St) = \int S_{\alpha\alpha}(y, y', St) \exp(-2\pi i k_y y') dy' \tag{6.23}$$

is a spatial Fourier transform of the S-matrix obtained from the one-rake measurements and the asterisk denotes a complex conjugate. The magnitude $|X_1|^2(k_y, y, St)$ is plotted as a function of $k_y b$ for selected representative values of the parameter St in Figure 6.4. The spatial wavenumber is normalized by b. All significant lateral correlation of streamwise fluctuations occurs for $k_y b < 0.7$. Similar results were examined for $|X_2|^2(k_y, y, St)$ and $|X_3|^2(k_y, y, St)$ and the results are presented in Figure 6.5 and in Figure 6.6, respectively. For u- and v- correlations significant spectral content is limited to $k_y b \leq 0.5$ and 1.2, respectively. In order to avoid spatial aliasing in the measurement of $S_{11}(y, y', St)$ it is required that the lateral probe spacing $\Delta y/b \leq 1/(2k_y b)_{max} = 0.7$. This corresponds to a requirement on lateral probe spacing of between 4.45 cm at $x/D = 50$ to 8.0 cm at $x/D = 90$. The requirements for measurement of $S_{22}(y, y', St)$ are less stringent. In this case the minimum required lateral probe separation
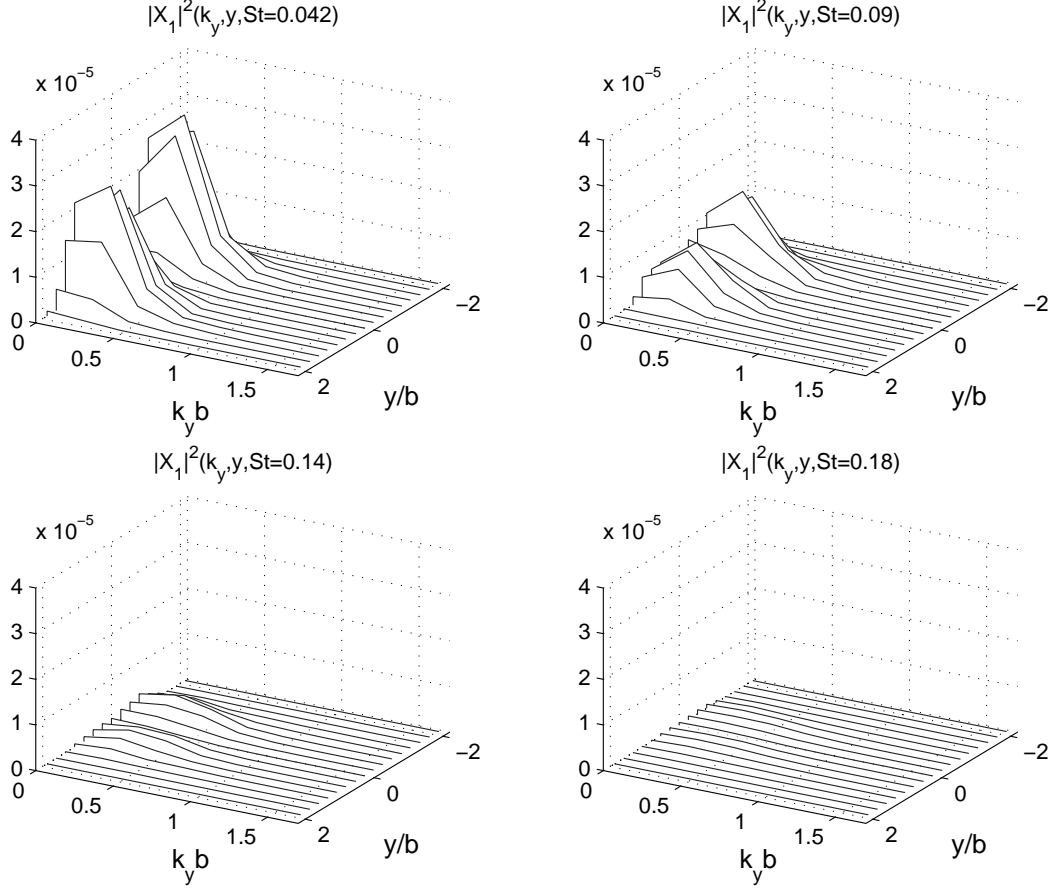
Figure 6.4: $|X_1|^2(k_y, y, St)$ for four frequencies $St = 0.042, 0.9, 0.14, 0.18$ at $x/D = 70$.

varies from 6.35 cm to 11.4 cm over the same streamwise range. The most stringent requirement for the avoidance of aliasing is associated with measurement of $S_{33}(y, y', St)$ which requires a probe separation of from 2.7 cm to 4.8 cm over the range $50 \le x/D \le 90$.

A summary of the all restrictions on Δy for different S-matrix measurements at all streamwise stations is presented in Table 6.2.

Summarizing, it was concluded that based upon the single rake measurements spatial aliasing would not be expected to significantly influence the u- or v-modes except perhaps at $x/D = 50$ where higher order u modes could be affected. The constraint on the w component means that only the lowest order w modes can be faithfully captured. Fortunately, it will be shown that the higher order w modes are of very low energy so this was not deemed a critical factor in the experiment.

Table 6.2: Maximum separation between the probes Δy_{max} (cm) for the two-rake experiments to avoid spatial aliasing for different S-matrix measurements.

x/D	50	60	70	80	90
S_{11}	4.45	5.3	6.2	7.1	8.0
S_{22}	6.35	7.6	8.9	10.1	11.4
S_{33}	2.7	3.2	3.7	4.2	4.8
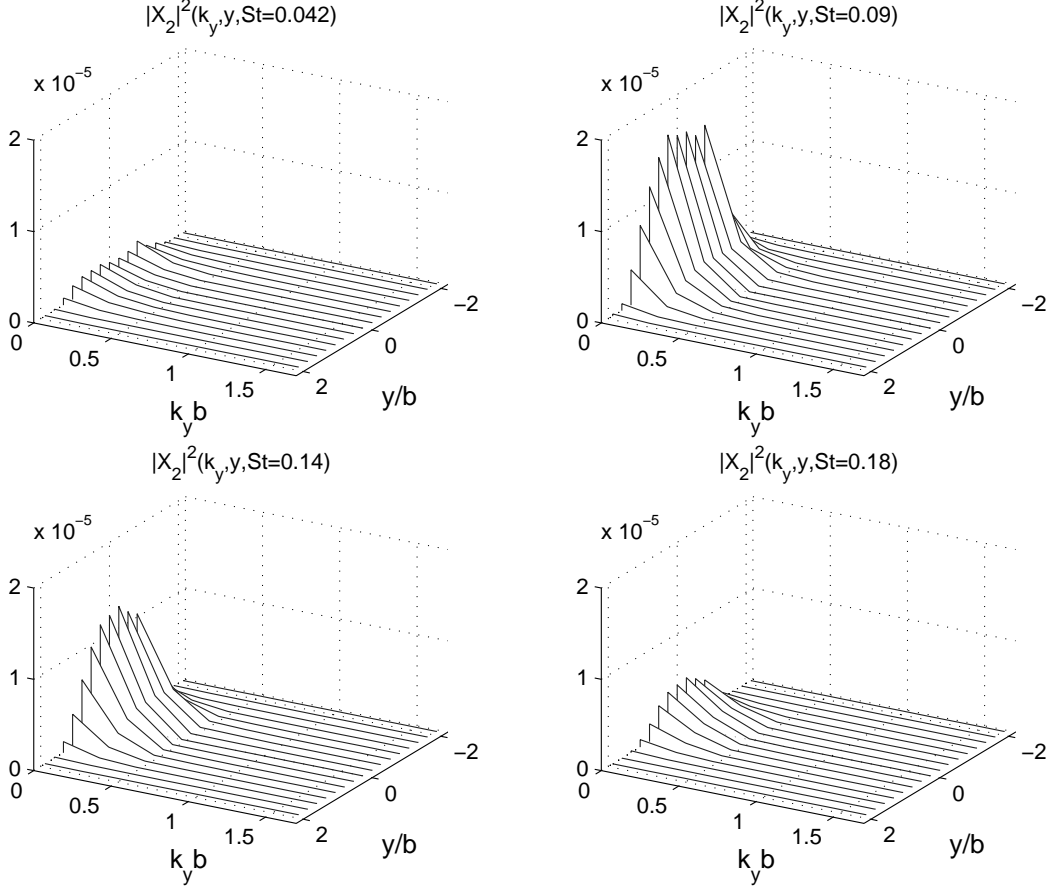
Figure 6.5: $|X_2|^2(k_y, y, St)$ for four frequencies $St = 0.042, 0.9, 0.14, 0.18$ at $x/D = 70$.

6.2.5   Averaging times for correlation measurements

In order to insure stationary statistics, convergence tests were performed. For the sampling rates quoted above (6.22), these showed that by sampling the fluctuating velocity in blocks of $N_p = 1024$ points for a total of $N_b = 500$ blocks the required cross-spectral statistics were fully converged. This corresponds to a total sample time of between 6.5 to 15.5 minutes as x/D varies from 50 to 90, respectively.

6.3   One-rake experiments

The cross-spectral matrix $S_{\alpha\beta}(y, y', f, \Delta z = 0)$ obtained with the single rake of 16 x-wire probes can be used to compute a set of single rake POD eigenmodes $\psi_\alpha^{(n)}(y; f)$ with corresponding eigenvalues $\mu^{(n)}(f)$ from the relation,

$$\int S_{\alpha\beta}(y, y'; f, \Delta z = 0) \; \psi_\beta^{(n)}(y'; f) \; dy' = \mu^{(n)}(f) \; \psi_\alpha^{(n)}(y; f). \qquad (6.24)$$

The approach taken in the numerical solution of the above integral equation is similar to that described for (6.5) in section 6.1.5. In this case, however, the resulting eigenfunctions are not functions of spanwise wavenumber k_z but depend only on Strouhal number, St, and the

33
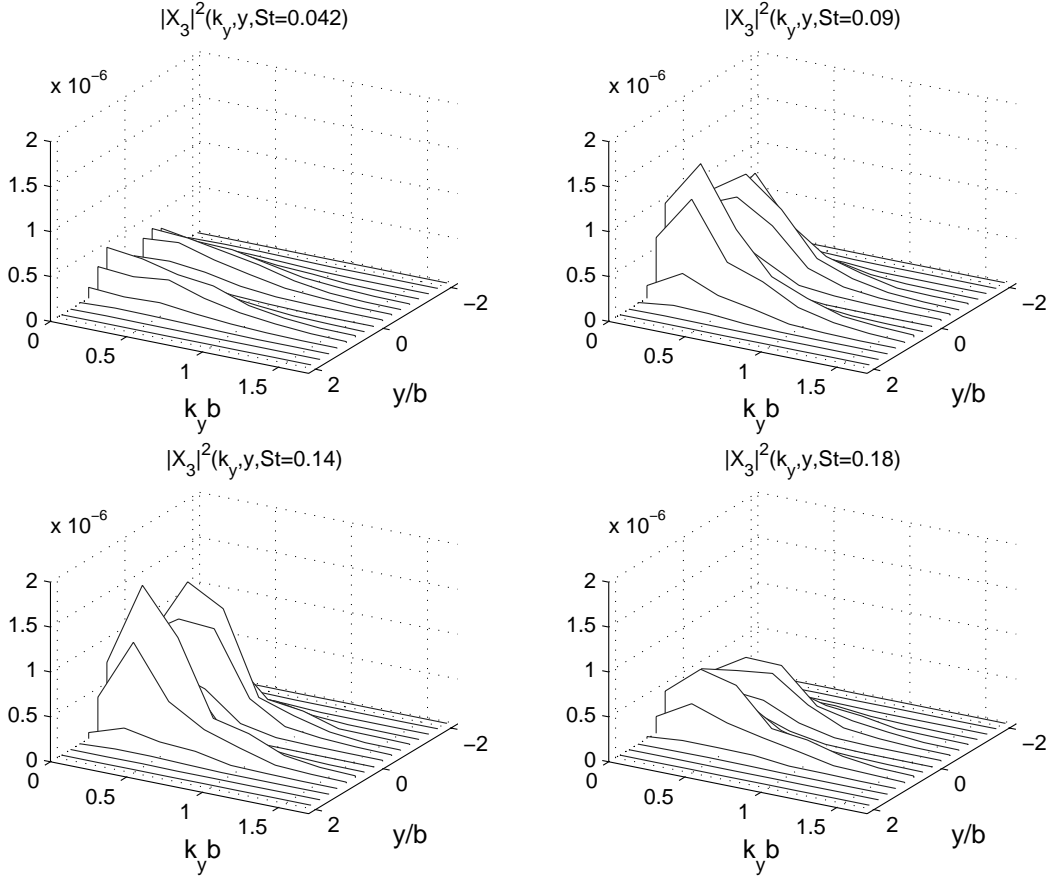
Figure 6.6: $|X_3|^2(k_y, y, St)$ for four frequencies $St = 0.042, 0.9, 0.14, 0.18$ at $x/D = 70$.

inhomogeneous spatial coordinate y. Since the probe spacing in y is one-half that for the two rake experiment, the spatial resolution of the eigenmodes is improved. However, since the one-rake experiment does not resolve the spanwise direction, the resulting POD modes will represent a weighted sum of the two-rake spanwise wavenumber dependent POD modes. Hence, comparison of the results obtained in the one and two rake experiments allows one to gauge the effects of rake resolution (because of the larger number of probes in the inhomogeneous coordinate) and the effects of aliasing multiple spanwise wavenumber k_z modes in measurements confined to a single $x - y$ plane.

The one-rake data were taken in blocks of $N_p = 1024$ points for a total of $N_b = 2000$ blocks at the same sampling frequencies, as for two rake experiments, Table 6.1.

6.4 Blockage effect

In order to check whether the rakes block the flow, a conventional measurements of the velocities were performed at $x/D = 70$ and compared with a single x-probe measurements. The results are shown in Figure 6.7. One can see that the blockage effect on the rake support system is negligible. So, the rakes don't disturb the jet and consequently the velocity components can be measured accurately.
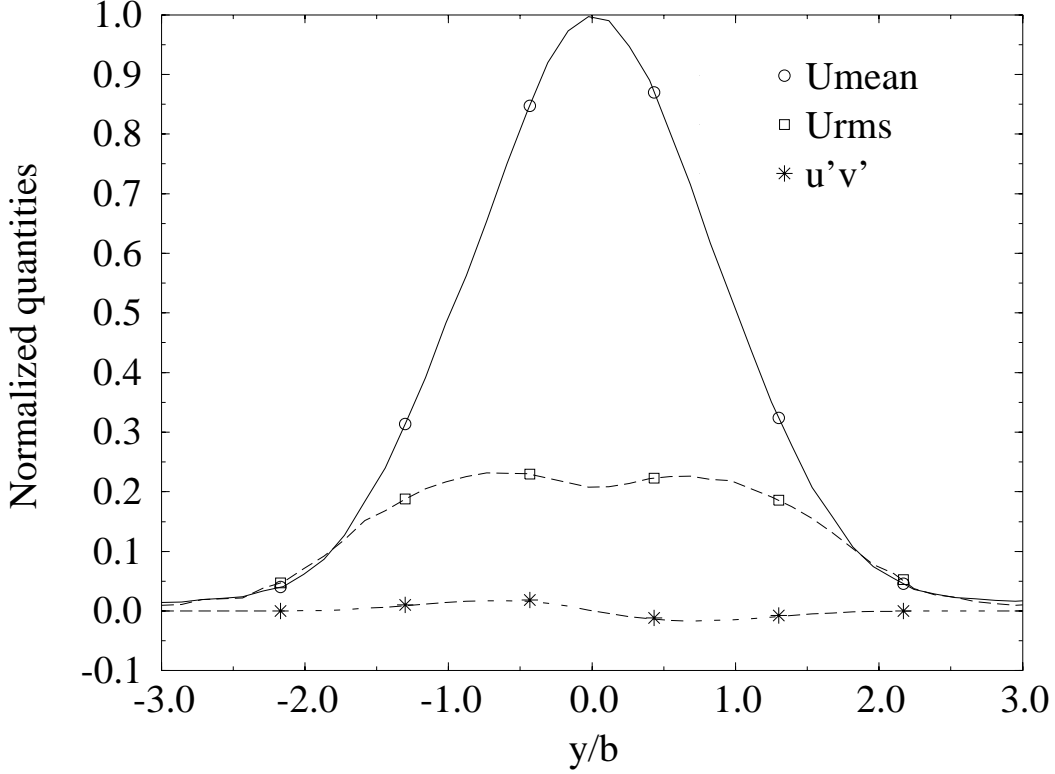
Figure 6.7: Comparison between single X-probe (solid lines) and the rake of X-probes (symbols) measurements of the selected velocity quantities.

6.5   Computer memory requirements

The required space to store the digital data for the two-rake experiments for one streamwise location is $2\ bytes \times 2\ rakes \times M \times 2\ velocity\_components \times N_p \times N_b \times N_z \approx 0.5$ GBytes. For 5 streamwise locations and two types of velocity measurements (u, v) and (u, w) the total amount of memory required is $2 \times 5 \times 0.5$ GBytes = 5 GBytes.

For one-rake measurements $N_z = 1$ and $N_b = 2000$ and the total memory requirement is 1.3 Gbytes.

6.6   Three-rake experiments

The set of three-rake measurements is conducted to investigate the shape of POD modes in physical space. Unlike one- and two-rake experiments, where the cross-spectral measurements are taken, the three rakes are used to acquire an instantaneous velocity record across the jet. The set-up is similar to the two-rake experiment, with three rakes of 8 x-wire probes each (for a total of 24 probes) with a constant z-separation H between them, see Figure 6.8.The value of $H = 8.9$ cm is chosen for the reasons to be discussed in Section 6.8.1. The separation between probes at each rake is the same as in two-rake experiment, $\Delta y = 5$ cm. The instantaneous velocity field at $x/D = 70$ was recorded with sampling frequency $f_s = 800$ Hz for $N_b = 100$ blocks of $N_p = 1024$ points each. Thus, the total sampling time is $T = N_p N_b/f_s = 128$ seconds. Both (u, v) and (u, w) velocity components are measured. These records are used to apply
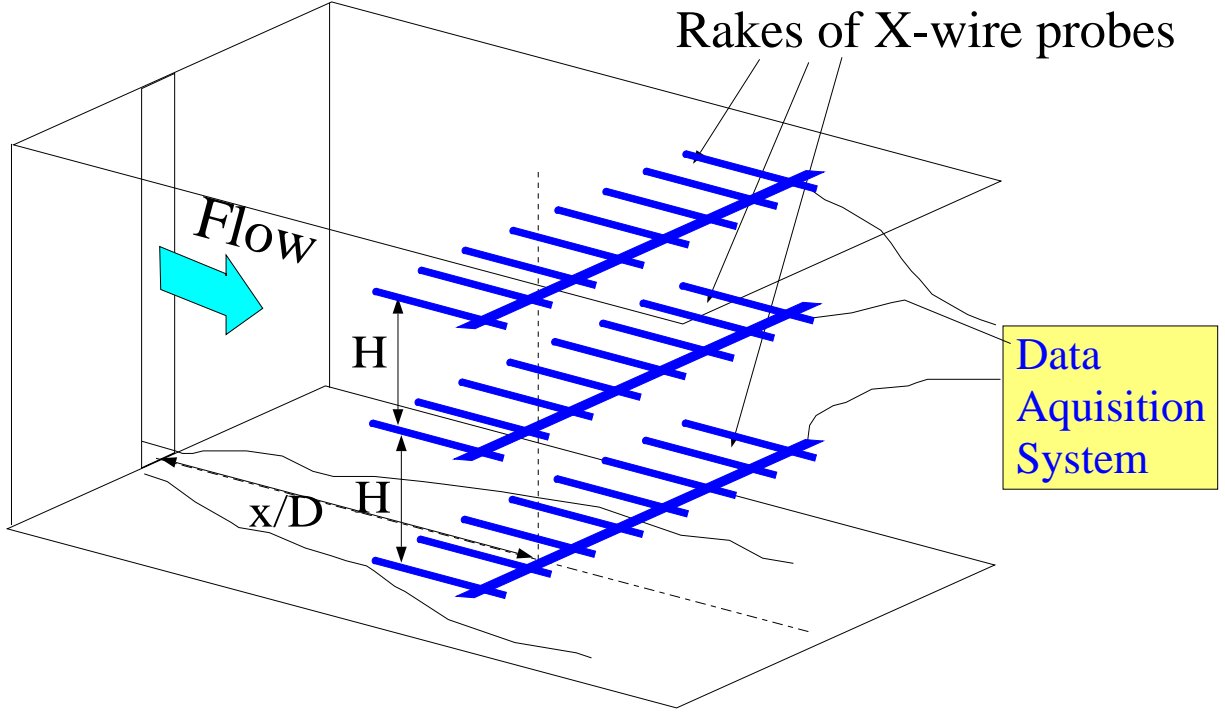
Figure 6.8: Orientation of the rakes in three-rake experiment.

the wavelet reconstruction procedure to reconstruct POD modes in the physical space. The reconstruction procedure is described in the following section.

6.7 Wavelet reconstruction of POD modes

In order to reconstruct the shape of the POD modes $\phi^{(n)}(y; f, k_z)$ in the physical space, an inverse transform in frequency and wavenumber domains must be performed. But the POD modes are known only up to an arbitrary phase $\exp(i\sigma(f, k_z))$. (Property 5, Section 3.2). Phase information can be restored by projection of the POD modes onto instantaneous realizations $u_\alpha(y, z, t)$ of the flow, using the continuous wavelet transformation. The algorithm consists of six steps, which are listed below,

1. The Fourier transform in the z-direction is performed to compute $\hat{u}_\alpha(y, k_z, t) = FT\{u_\alpha(y, z, t)\}$,

2. The wavelet transformation in time (4.1) is calculated, $\tilde{u}_\alpha(y, k_z; a(f), \tau) = WT(a, \tau)\{\hat{u}_\alpha(y, k_z, t)\}$.

3. Using the orthogonality of POD modes, the phase related wavelet coefficients $c^{(n)}(k_z; a(f), \tau)$ can be computed by projecting POD modes onto an instantaneous realization,

$$c^{(n)}(k_z; a(f), \tau) = \int \tilde{u}_\alpha(y, k_z; a(f), \tau)\varphi_\alpha^{(n)}(y; f, k_z)dy$$

4. The wavelet transform of each POD mode can be restored

$$\tilde{u}_\alpha^{(n)}(y, k_z; a(f), \tau) = c^{(n)}(k_z; a(f), \tau)\varphi_\alpha^{(n)}y; f, k_z)$$

36

5. The inverse wavelet transform (4.5) provides the POD mode in physical space,

$$\hat{u}_\alpha^{(n)}(y, k_z, t) = WT^{-1}(a, \tau)\left\{\tilde{u}_\alpha^{(n)}(y, k_z; a(f), \tau)\right\}$$

6. Finally, the inverse Fourier transform restores the POD modes in physical domain, $u_\alpha^{(n)}(y, z, t) = FT^{-1}\{\hat{u}_\alpha^{(n)}(y, k_z, t)\}$

The flow field is a sum of all POD modes,

$$u_\alpha(y, z, t) = \sum_{n=1}^{\infty} u_\alpha^{(n)}(y, z, t)$$

6.7.1 Morlet mother function

Particular choice of the mother function for the wavelet transform (4.1) usually depends on what kind of information we are interested in extracting from the signal and is determined by its shape. This investigation uses a complex Morlet wavelet mother function as the basis for the wavelet transform. An analytical expression for the Morlet wavelet is as follows,

$$g(x) = e^{irx}e^{-x^2/2} - e^{-r^2/2}e^{-x^2/2}, \tag{6.25}$$

where r is a user specified constant. Note that since the Morlet wavelet is complex, it can provide local information concerning both amplitude and phase at a given scale. For example, if the Morlet wavelet transformation is applied for the simple case of $f(t) = Ae^{i(2\pi ft+\phi)}$ the straightforward calculation gives

$$\tilde{f}(a, \tau) = \sqrt{2\pi a}e^{-(2\pi fa-r)^2/2}(1 - e^{-r2\pi fa})Ae^{i(2\pi f\tau+\phi)} \tag{6.26}$$

The resulting wavelet transform is a function of a and τ. Note, that the wavelet transformation gives only finite frequency resolution. The modulus of (6.26) is maximum at

$$a(f) \approx r/2\pi f \tag{6.27}$$

for $r > 3$ and allows one to relate scale a and frequency f. For the research described in this thesis the constant r was chosen to be $r = 6$.

6.8 Numerical implementation of wavelet reconstruction

From the three-rake experiment, (u, v) or (u, w) components of the velocity field are given at discrete spatial and temporal points, $u_\alpha(m\Delta y, z(k), t_i)$, where $z(k)$ are the z-locations of the rakes, $t_i = i/f_s$. Therefore, all the continuous integrations in the wavelet reconstruction algorithm, described in Section 6.7 should be replaced by an appropriate finite summation.

6.8.1 Discrete Windowed Fourier Transform

The Fourier transform is replaced with its discrete analog. Since only three points in the z-direction are available, the Discrete Windowed Fourier Transform was chosen to process the data,

$$X(k) = \frac{1}{2}\sum_{n=0}^{2} x(n)w(n)\exp\left(-\frac{2\pi ikn}{2}\right), \quad k = 0, .., 2, \tag{6.28}$$

where $x(n) = u_\alpha(m\Delta y, z(n), t_i)$, $n = 0, 1, 2$ are velocities from the corresponding rakes, positioned at $z(n)$-locations. The trapezoidal weighting vector is $w = [0.5, 1, 0.5]$ and the transformation (6.28) looks as follows,

$$
\begin{aligned}
X(0) &= 0.5[0.5x(0) + x(1) + 0.5x(2)] \\
X(1) &= 0.5[0.5x(0) - x(1) + 0.5x(2)] \\
X(2) &= 0.5[0.5x(0) + x(1) + 0.5x(2)] = X(0)
\end{aligned}
$$

The zeroth coefficient $X(0)$ represents the $(k_z = 0)$-mode or *planar* mode. The first coefficient $X(1)$ provides information about the $(k_z = 1/(2H))$-mode. The discrete Fourier transform works as a band-pass filter in the z-direction with the Nyquist wavenumber $k_z^{(N)} = 1/H$. In order to avoid aliasing from non-zero k_z-modes into the planar mode, the separation H must be chosen in such way that there is no significant correlation in the z-direction above the Nyquist wavenumber. This constraint can be rewritten in terms of the cross-spectral matrix Φ as

$$
\Phi_{\alpha\beta}(y_i, y_j; f, k_z > k_z^{(N)} = 1/H) \approx 0. \tag{6.29}
$$

This criterion provides the restriction for the separation H between the rakes. Based on the results to be presented in section 7.5.1, the value of $H = 8.9$ cm was chosen.

The inverse Discrete Fourier Transform is taken in the following form,

$$
x(n) = \sum_{k=0}^{2} X(k)w(k)\exp\left(\frac{2\pi ikn}{2}\right) = X(0) + X(1)(-1)^n, \; n = 0, 1, 2
$$

6.8.2   Numerical implementation of wavelet transform

To compute the forward wavelet transform, equation (4.1) is replaced by a finite integral approximation for the case of a zero-order interpolation between data points,

$$
\tilde{u}_\alpha(m\Delta y, k\Delta k_z; a_n, \tau_j) = \frac{1}{\sqrt{a_n}}\sum_{i=1}^{N_p} \hat{u}_\alpha(m\Delta y, k\Delta k_z, t_i)g^*\left(\frac{t_i - \tau_j}{a_n}\right)\Delta t,
$$

The complex Morlet mother function $g(x) = exp(irx - x^2/2)$, $r = 6$ is used. Since POD modes are known only at finite points $\varphi_\alpha(m\Delta y, n\Delta f, k\Delta k_z)$, the wavelet transform is calculated at discrete time points $\tau_j = t_j$ for $N_p/2$ scales, chosen according to (6.27), $a(n\Delta f) = r/(2\pi n\Delta f)$, $n = 1..N_p/2$, $\Delta f = 1/T = f_s/N_p$.

The inverse wavelet transform is computed by replacing the integral to a finite summation,

$$
\hat{u}_\alpha^{(n)}(m\Delta y, k\Delta k_z, t_i) = \frac{\Delta t}{C(g)}\sum_{n=1}^{N_p/2-1}\sum_{j=1}^{N_p}\frac{\tilde{u}_\alpha^{(n)}(m\Delta y, k\Delta k_z; a_n, \tau_j)}{\sqrt{a_n}}g\left(\frac{t_i - \tau_j}{a_n}\right)\frac{(a_{n+1} - a_n)}{a_n^2},
$$

where $C(g) = 0.471$, according to (4.2).

6.8.3   Numerical projection of POD modes into the flow

The numerical calculation of the projection of POD modes into the instantaneous flow field looks as follows,

$$
c^{(n)}(k\Delta k; a_n, \tau_j) = \sum_{m=1}^{M}\tilde{u}_\alpha(m\Delta y, k\Delta k_z; a_n, \tau_j)\varphi_\alpha^{(n)}(m\Delta y, n\Delta f, k\Delta k_z)w(m)\Delta y
$$

with $w(m) = (0.5, \overbrace{1, 1, .., 1}^{M-2}, 0.5)^T$ as a trapezoidal weighting function.

Chapter 7

RESULTS

All information about the POD modes is contained in the cross-spectral matrix $\Phi_{\alpha\beta}$ (6.4). In order to understand the essential features of the cross-spectral matrix, recall that it is obtained by applying a spatial Fourier transform to the experimentally measured matrix $S_{\alpha\beta}$ (6.3). So, before going into details about the shape of the POD modes, let us first examine essential features of both the Φ-matrix and S-matrix.

7.1 One-rake measurements of $S_{\alpha\beta}(y, y', St, \Delta z = 0)$-matrix

During one rake experiments, 16 probes were placed at one rake and the S-matrix was measured. For this case, the separation between rakes can be treated as zero, $\Delta z = 0$. Otherwise noticed, everywhere below the S-matrix is a function of (y, y', St). Let us examine some important features of the S-matrix.

The measurements of S_{11}, S_{12}, S_{22}, S_{13}, and S_{33} (6.3) with 16 probes placed on one rake were performed at five streamwise stations, $x/D = 50, 60, 70, 80$ and 90. In this section the results are presented only for $x/D = 70$ and the results may be considered representative. Everywhere below the crosstream coordinate y is scaled by the local half-width b and the frequency f is scaled by $U_{\max}/b$ to obtain the Strouhal number, $St = fb/U_{\max}$. Analysis of $S_{\alpha\alpha}$ reveals that S_{11}, S_{22} and S_{33} reach maximum value at $St = 0.05, 0.1$ and 0.14 correspondingly. For these reason, the frequencies (along with with an additional $St = 0.19$) are chosen to characterize the S-matrix behavior in the (y, y') planes. The real and imaginary parts of $S_{11}(y, y', St)$ for four frequencies $St = 0.05, 0.1, 0.14, 0.19$ are shown in Figure 7.1 as contour plots. Central symmetry about the origin $y = y' = 0$ (6.12) and symmetry about the line $y = y'$ (6.11) can be clearly observed in both the real and imaginary parts. Note, that from these symmetries it follows that $Im\{S_{\alpha\alpha}(y, y, f)\} = Im\{S_{\alpha\alpha}(y, -y, f)\} = 0, \alpha = 1..3$. This property of imaginary part also can be observed in Figure 7.1. The maximum positive correlation occurs for probes at one side of the jet at $y/b = y'/b = \pm 0.9$ for $St = 0.05$ and quickly decays as St increases with the peak's locations gradually shifting to $y/b = y'/b = \pm 0.7$. In the center of the jet the correlations are much smaller. The reason is that the S-matrix reflects only large-scale correlations, on the order of the spacing between the probes $\Delta y_1 = 1$". Small correlation in the center of the jet means that mostly small scale turbulent fluctuations are responsible for the essentially non-zero values of $u_{rms}(y = 0)$ (see Figure 5.4). Positive correlations are confined to a regions on either side of the jet, with no positive correlation across the jet. Note that,

negative correlation of u-component of velocity across the centerline of the jet is indicated in the Figure 7.1. The maximum negative correlation occurs at $(y/b, y'/b) = \pm(0.7, -0.7)$ for $St = 0.05$ and dies out rapidly with St increasing. We'll discuss the importance of negative correlations as an indicator of large-scale structure in section 7.4. Finally note the generally smaller magnitude of the imaginary part of S_{11} relative to the real part.

The v-component $S_{22}(y, y', St = 0.05, 0.1, 0.14, 0.19)$ is presented in Figure 7.2. It reveals only positive v-correlation across the jet, with maximum values at $St = 0.1$. This value is in good agreement with the value obtained in [36] and [7]. Figure 7.2 shows that the correlation magnitude decreases for large St.For each St, maximum auto-correlations form a plateau of fairly constant values in the center of the jet. The plateau width shrinks with increasing frequency. The imaginary part is significantly smaller than the real part. Both symmetries (6.11) and (6.12) are clearly observed.

The values of the real and imaginary parts of $S_{33}(y, y', St = 0.05, 0.1, 0.14, 0.19)$ represent w-component correlation and are plotted in Figure 7.3.Small squares visible on the diagonal line $y = y'$ are artifacts of the plotting software. Non-zero correlation values are confined to the region near the diagonal $y = y'$ and quickly decay for $|(y - y')/b| > 0.7$. Two peaks of the correlation are located at $y/b = \pm 0.7$ with maximum values at $St = 0.14$. Small negative correlations are noticeable at $(y/b, y'/b) = \pm(0.7, -0.7)$ around $St = 0.14$. Note, that the maximum values of the S_{33}-matrix are roughly four times smaller than the maximum values of the S_{11}-matrix. The rate of decay of S_{33} is slower as $St \to \infty$ than in the case for S_{11} and S_{22}.

The real and imaginary parts of the cross-correlation between u- and v-components $S_{12}(y, y', St = 0.05, 0.1, 0.14, 0.19)$ is plotted in Figure 7.4.The U-component is measured at the y-location and and v-velocity is taken along y'-axis. Positive correlations occur for $y > 0$ and negative correlations exist for $y < 0$. Maximum value of the correlation is located at $(y/b, y'/b) = \pm(0.7, 0.7)$ over the range of $St = [0.05..0.1]$. No correlation between u-and v-components exists along the line $y = 0$, $\overline{u'(y = 0)v'(y')} = 0$. Recall that the v-component is positively correlated across the jet while the u-component is antisymmetric with respect to the jet centerline. That Figure 7.4 shows that $Re\{S_{12}\} = 0$ when $y = 0$ but is nonzero for $y' = 0$ indicates that streamwise fluctuations on the centerline must be associated primarily with small scales and are uncorrelated with the larger-scale lateral fluctuations. The iso-contours of $Im\{S_{12}\}$ shown in Figure 7.4 indicate that the imaginary part of the tensor is considerably smaller than the real part. The correlation magnitude gets weaker for large St. Figure 7.5 presents the real and imaginary parts of $S_{13}(y, y', St)$. The magnitude of both the real and imaginary parts of S_{13} are at a given Strouhal number are generally much smaller than for S_{12}. Significant values of S_{13} are restricted to smaller probe separations than for S_{12}. Finally, the iso-contours exhibit much more complex patterns than for other components of the cross-spectral tensor.

7.2 Behavior of $S_{11}-$matrix for $\Delta z \neq 0$

Let's first briefly examine the symmetries and behavior of $S_{\alpha\beta}(y, y'; St, \Delta z)$ for a non-zero separation between the two rakes. To illustrate the Δz-variation of the $S_{\alpha\beta}$-matrix, contour plots of the real part of the $S_{11}(y, y'; St = 0.05, \Delta z)$ for six different Δz separations are presented in Figure 7.6. The separation Δz is normalized by $b(x)$. Symmetries (6.11) and (6.12) are observed in this figure. Comparison of the $\Delta z/b = 0$ case shown in Figure 7.6 with the corresponding part of the Figure 7.1 reveals an almost identical behavior in the (y, y') domain.

The small difference is likely associated to the lower lateral spatial resolution for the two-rake case.

Figure 7.6 shows that increasing Δz weakens the correlation between the probes on different rakes. Note that the correlation between two probes located near $y/b = y'/b = \pm 1$ even changes sign, being positive for $\Delta z/b < 1.5$ and becoming negative for $\Delta z/b > 1.5$. For all z-separations the S_{11}-matrix is symmetrical about the center $y = y' = 0$. As it was discussed before, this is a consequence of the lateral symmetry of the jet about the centerline (6.11).
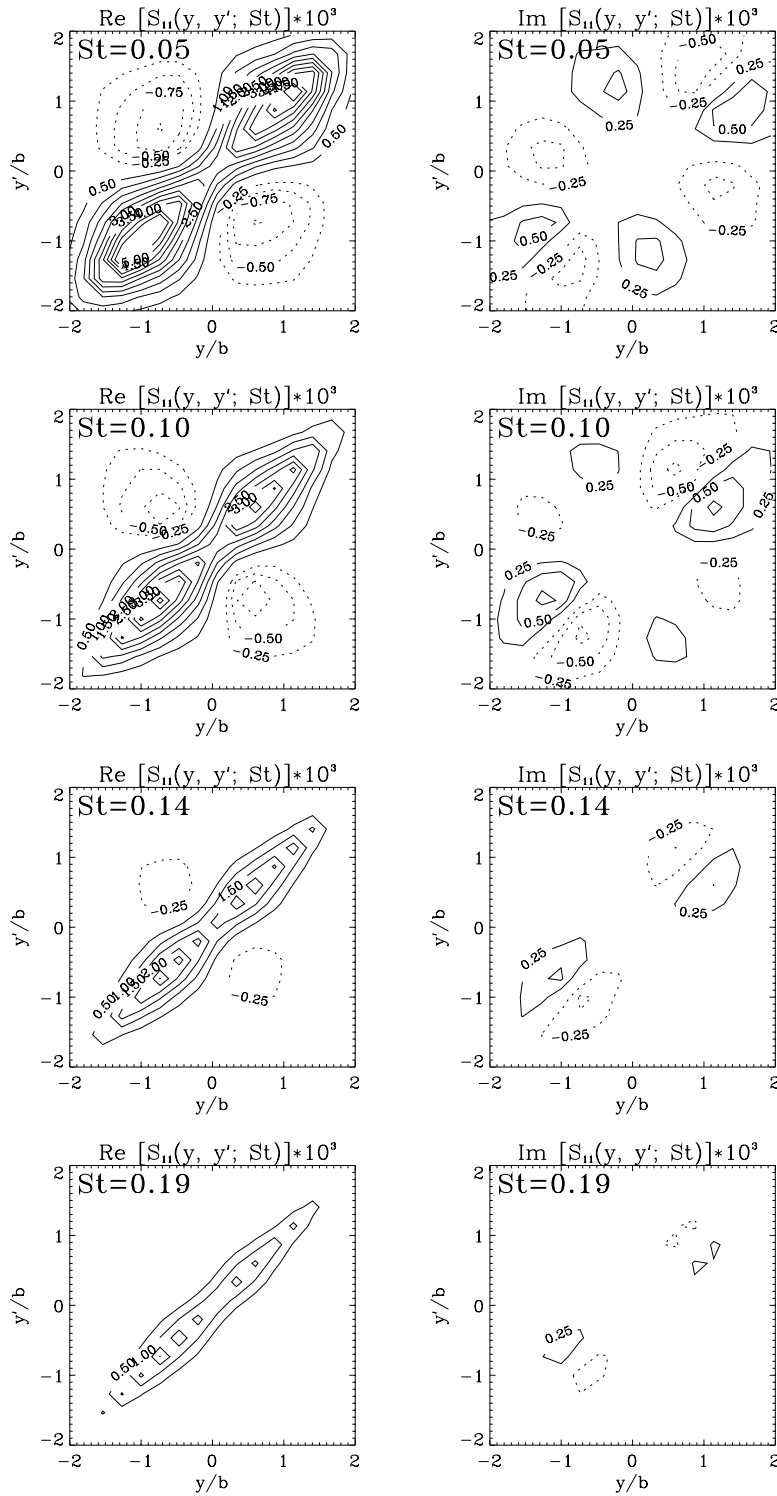
Figure 7.1: The spectral correlation matrix $S_{11}(y, y', St) \times 10^3$ for $St = 0.05, 0.1, 0.14, 0.19$ at $x/D = 70$
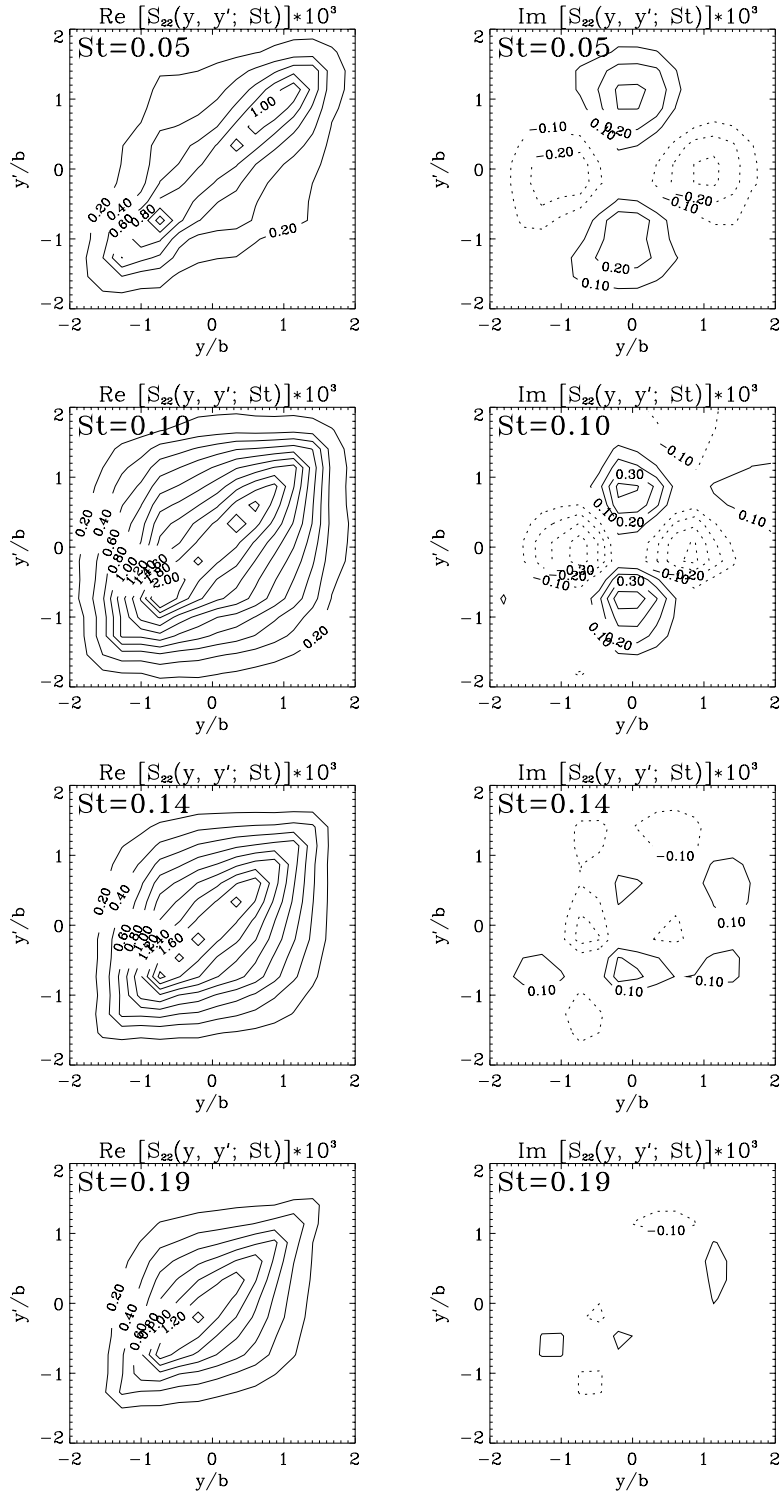
Figure 7.2: The spectral correlation matrix $S_{22}(y, y', St) \times 10^3$ for $St = 0.05, 0.1, 0.14, 0.19$ at $x/D = 70$
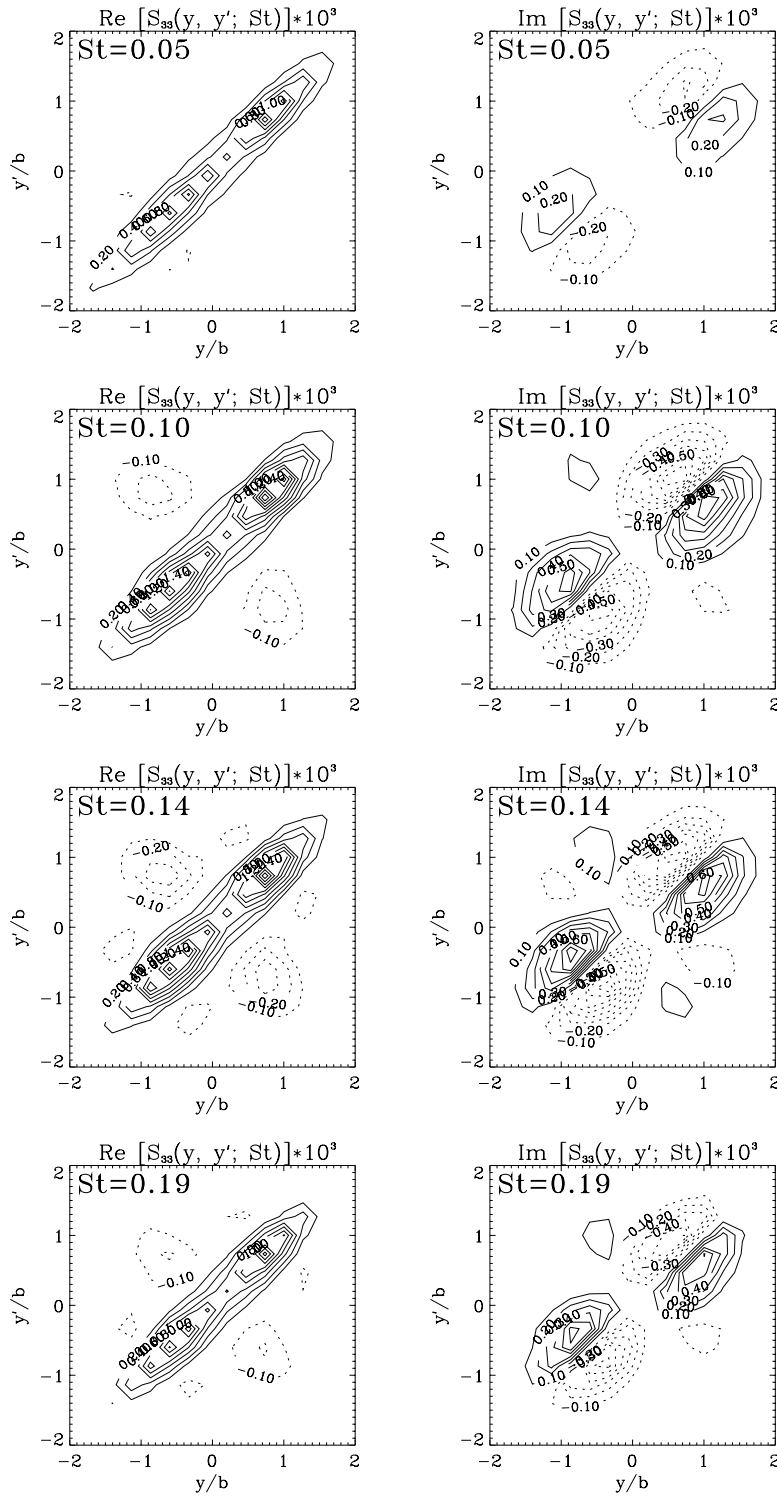
Figure 7.3: The spectral correlation matrix $S_{33}(y, y', St) \times 10^3$ for $St = 0.05, 0.1, 0.14, 0.19$ at $x/D = 70$
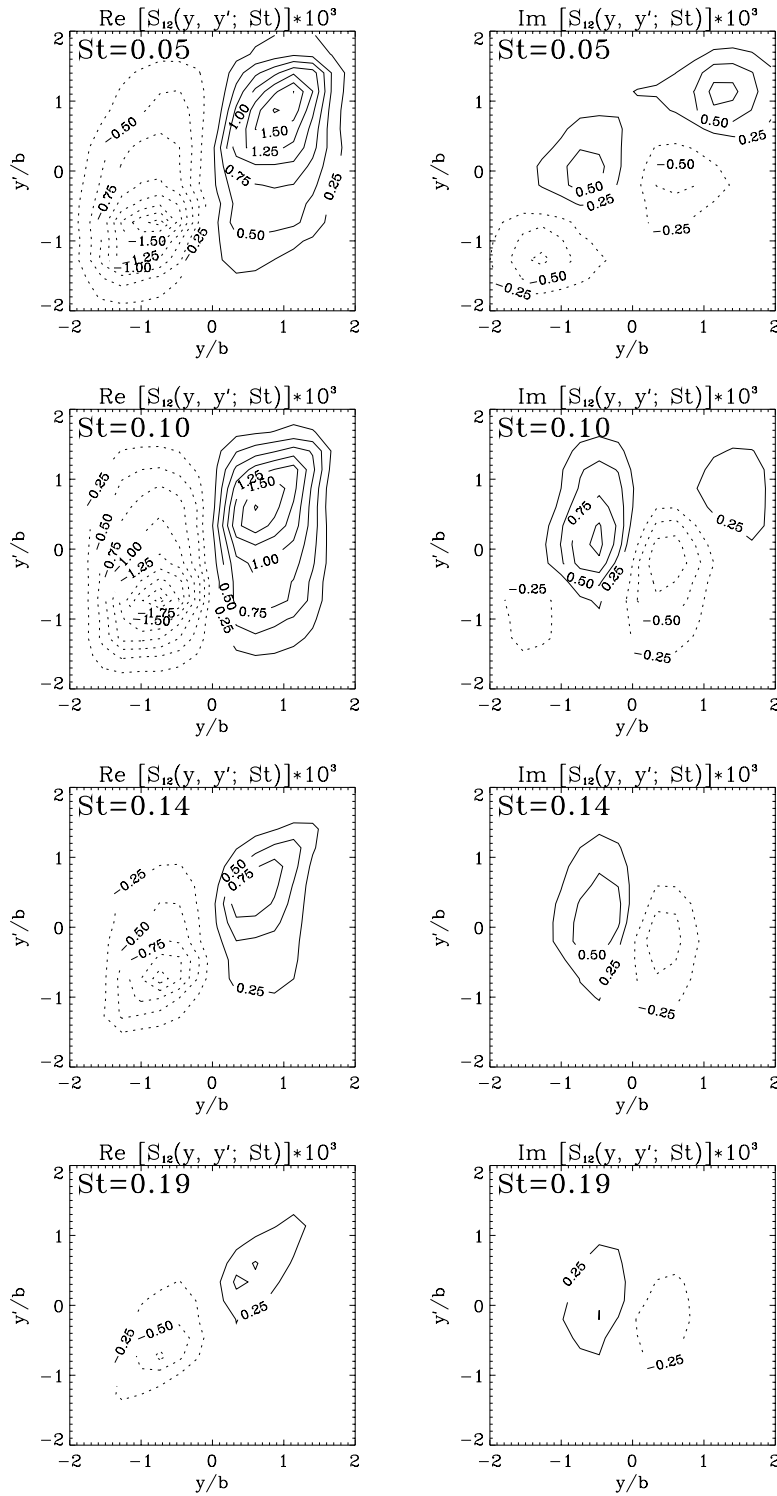
Figure 7.4: The spectral correlation matrix $S_{12}(y, y', St) \times 10^3$ for $St = 0.05, 0.1, 0.14, 0.19$ at $x/D = 70$
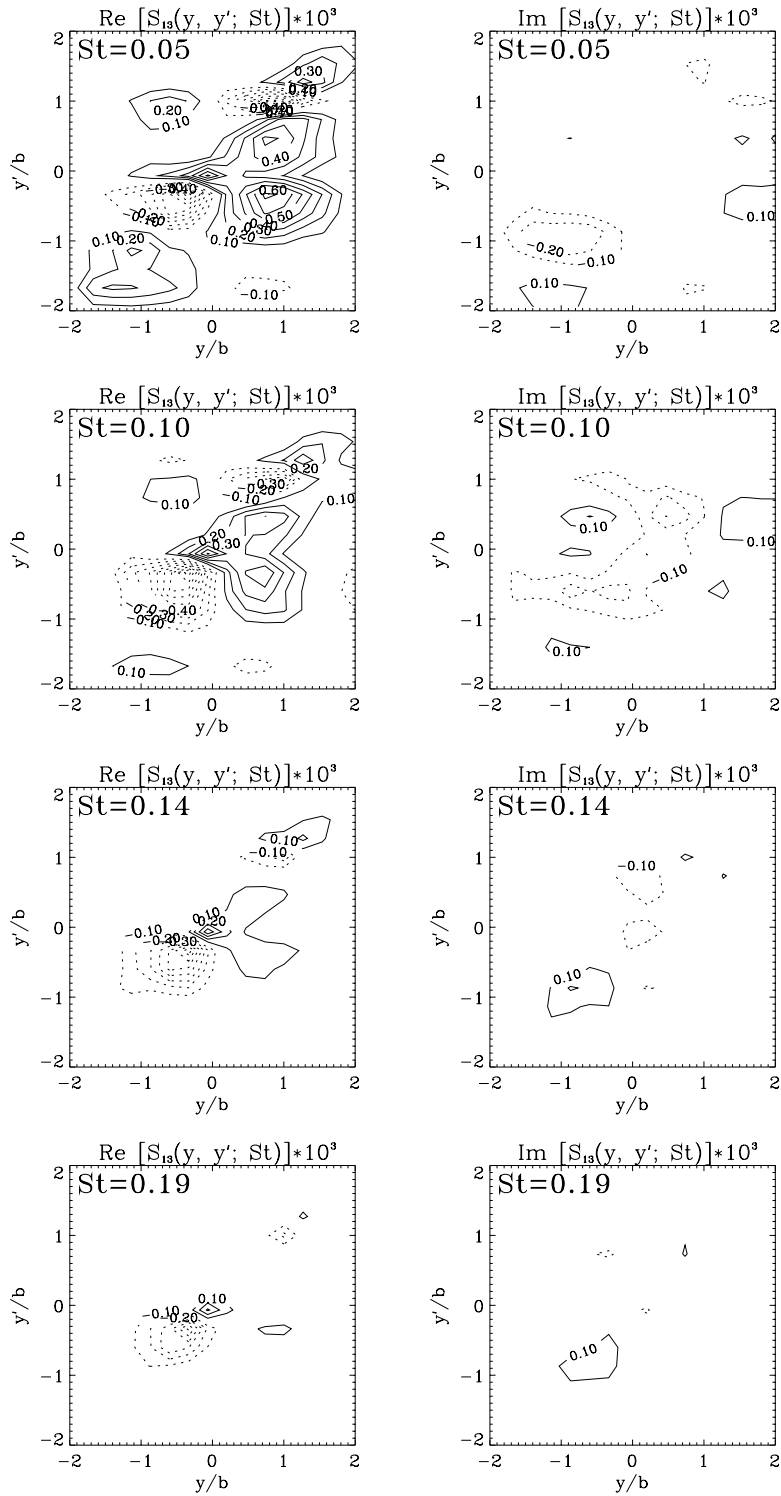
Figure 7.5: The spectral correlation matrix $S_{13}(y, y', St) \times 10^3$ for $St = 0.05, 0.1, 0.14, 0.19$ at $x/D = 70$
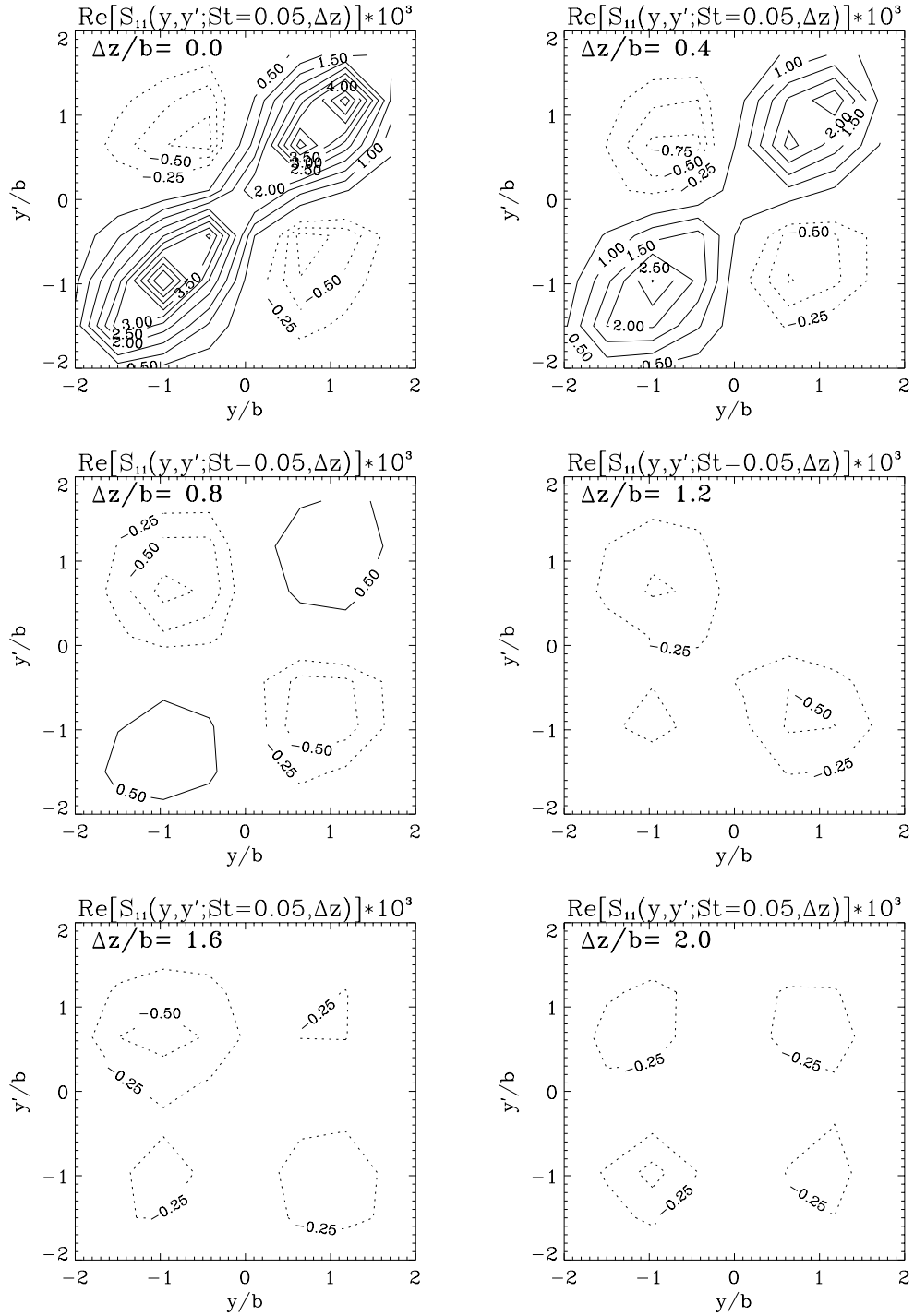
Figure 7.6: Spanwise variation of the real part of spectral correlation matrix $Re\{S_{11}(y, y', St = 0.05, \Delta z)\}$ for $\Delta z/b = 0.0, 0.4, 0.8, 1.2, 1.6, 2.0$ at $x/D = 70$

7.3 Two-rake measurements of the Φ-matrix

In this section the experimental measurements of the spectral cross-correlation matrix $\Phi(y, y', f, k_z)$ (6.4) are presented. Essentially, the Φ-matrix unfolds the S-matrix in the z-direction. It is based on the measurements of S-matrix for different spanwise separations between rakes. Computing the Φ-matrix involves taking the Fourier transform in z-direction only, so a similar variation in the y-direction and in frequency space as the S-matrix exhibits is expected. Measurements of Φ_{11}, Φ_{22}, Φ_{12}, Φ_{23} and Φ_{33} using two rakes are performed at several streamwise locations $x/D = 50, 60, 70, 80$ and 90. Because of the self-similar behavior of the Φ-matrix in the streamwise direction for the reported stations, the results for $x/D = 70$ will be presented only.

In general, Φ-matrix is a complex matrix and is a function of four variables, (y, y', f, k_z). Everywhere below the spanwise wavenumber k_z is scaled by $1/b$. From symmetry (6.12) it follows $Im\{S_{\alpha\alpha}(y, y, f, \Delta z)\} \equiv 0$ and, using (6.3),
$Im\{\Phi_{\alpha\alpha}(y, y, f, k_z)\} \equiv 0$, $\alpha = 1..3$.
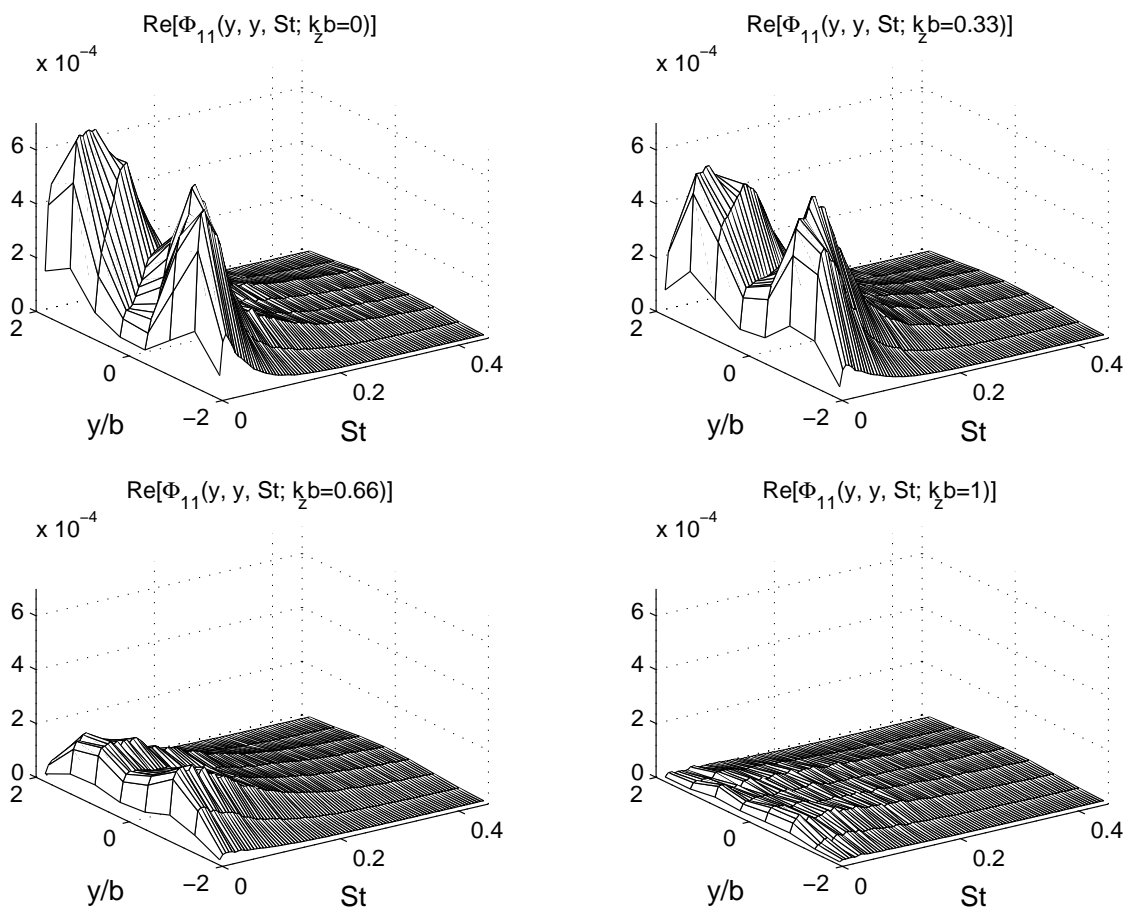
Figure 7.7: The real part of the spectral correlation matrix $Re[\Phi_{11}(y, y, St, k_z b)]$ for $k_z b = 0, 0.33, 0.66, 1$

A plot of the real part of $u - u$-correlations $\Phi_{11}(y, y, St, k_z b)$ for four wavenumbers $k_z b = 0, 0.33, 0.66, 1$ is shown in Figure 7.7. The correlation matrix has two well-defined positive peaks at $(y/b = \pm 1, St = 0.05)$. It quickly decays for large St, so the spectral correlation in frequencies higher than $St > 0.4$ is negligible. Nevertheless, small tales in correlation for large

49

St suggest some degree of intermittency in time of the underlying structure. As a function of k_z, the maximum correlation occurs at $k_z = 0$ and gets weaker for large k_z, so virtually no significant correlation is present above $k_z b > 1$. At the centerline of the jet correlation values are fairly small. The frequency $St = 0.05$ corresponds to a peaks in the frequency domain. The spectral correlation across the centerline of jet for $\Phi_{11}(y, y', St = 0.05, k_z)$ for the same selected wavenumbers $k_z b = 0, 0.33, 0.66, 1$ is plotted in Figure 7.8. The negative correlation between the velocities at the opposite sides of the jet is clearly seen for $k_z = 0$ (negative correlations are indicated with dashed lines). This figure is quite similar to $S_{11}(y, y', St)$ at Figure 7.1. It follows from (6.4)

$$S_{11}(y, y', \Delta z = 0, St) = \int \Phi_{11}(y, y'; St, k_z) dk_z. \qquad (7.1)$$

that the similarity between $S_{11}(y, y', St)$ and $\Phi_{11}(y, y'; St, k_z = 0)$ indicates that higher k_z modes contribute little to S_{11}. This means that the dominant structure responsible for u-u correlations is a planar structure in the spanwise direction. Nevertheless, correlations at non-zero wavenumbers indicates a presence of three-dimensional structures as well.

The real part of $\Phi_{22}(y, y, St, k_z b)$ (v-v correlations) for $k_z b = 0, 0.17, 0.33, 0.5$ is given in Figure 7.9. The correlation reaches maximum at $(y = 0, St = 0.1, k_z = 0)$ and quickly decays for large St and k_z. The contours of $\Phi_{22}(y, y', St = 0.10, k_z b = 0, 0.33)$ are plotted in Figure 7.10 and indicate only positive correlations for v-component of the velocity across the jet. In this case only two spanwise wavenumbers are shown since the decay of Φ_{22} with k_z is even more rapid than was the case for the streamwise fluctuations. The implication is that the structure in the flow responsible for the large-scale v-component correlation is quite two-dimensional in nature. Also the correlations are quite similar to $S_{22}(y, y', St)$ at Figure 7.2. Therefore, a similar conclusion about the dominant planar structure in the jet can be made.

The real part of the $w - w$ correlation, $\Phi_{33}(y, y, St, k_z b = 0, 0.33, 0.66, 1)$ is presented in Figure 7.11. The two-positive correlation peaks are located at $(y/b = \pm 0.7, St = 0.11, k_z = 0)$ and no visible correlations exist for $St > 0.4$ and $k_z b > 0.5$. Comparison with results for Φ_{11} and Φ_{22} shown in Figures 7.7 and 7.9, respectively, reveal that the correlation levels associated with the w-component are considerably smaller than those for the u and v-component fluctuations. The variation of the real and imaginary parts of $\Phi_{33}(y, y', St = 0.14, k_z b = 0, 0.33, 0.66)$ with spanwise wavenumber are presented in Figure 7.12. This figure indicates a small negative correlation of w-component across the jet for $k_z = 0$. The rate of decay with increased wavenumber is generally smaller in this case suggesting that a non-planar structure is responsible. This is also evident in comparing Figure 7.12 with S_{33} shown in Figure 7.3. There is considerable difference, especially in the imaginary parts. This suggests that higher spanwise wavenumber modes are considerably more significant for the w-component fluctuations than was the case for v or u.

The real and imaginary parts of the mixed correlation between u-and v-velocity components $\Phi_{12}(y, y, St, k_z b = 0, 0.33, 0.66, 1)$ are plotted in Figures 7.13 and 7.14. This figure reveals a strong anti-symmetrical correlation between the u- and v-components of the velocity at $St = 0.07$ for small $k_z b < 0.5$. The maximum values of the correlations are located at $y/b = \pm 1$. Much smaller values of the imaginary part of Φ_{12} suggests near zero phase correlation. These figures reveal a fairly rapid decay of Φ_{12} with k_z which suggests that motions responsible for large-scale $u - v$ correlation are largely two-dimensional. This is also apparent from comparison of $\Phi_{12}(y, y', St = 0.1, k_z b = 0, 0.33)$ in Figure 7.15 with S_{12} as measured in the single rake experiment (Figure 7.4). The pattern exhibited by $Re(\Phi_{12})$ is consistent with the existence of

Figure 7.8: The spectral correlation matrix $\Phi_{11}(y, y', St = 0.05, k_z b) \times 10^3$ for $k_z b = 0, 0.33, 0.66$.

a structure that gives rise to antisymmetric large-scale u-fluctuations and v-fluctuations which exhibit positive correlation across the jet.

The variation with spanwise wavenumber of the real and imaginary parts of $\Phi_{13}(y, y', St = 0.1, k_z)$ are shown in Figure 7.16. These show significant correlation between u and w-component fluctuations. The real part of the $u - w$ correlation $\Phi_{13}(y, y, St, k_z b = 0, 0.33, 0.66, 1)$ is presented in Figure 7.17 and the imaginary part of the Φ_{13} is shown in Figure 7.18. From (6.10) it follows that $\Phi_{13}(y, y', St, k_z = 0) = 0$. Hence, there is no contribution to the Φ_{13}-tensor by the planar structure $(k_z = 0)$. It has already been noted that the motions responsible for the w fluctuations must be three-dimensional in nature. Figure 7.17 suggests that a component of the streamwise fluctuations is attributable to this structure as well. The decay of Φ_{13} with spanwise wavenumber is slower than for Φ_{12}. In addition, there is little resemblance between the contour plots shown in Figure 7.17 with S_{13} as measured in the single rake experiment (Figure 7.5).

Figure 7.9: The real part of the spectral correlation matrix $Re[\Phi_{22}(y, y, St, k_z b)]$ for $k_z b = 0, 0.17, 0.33, 0.5$

Summarizing, the most energetic spectral correlations $\Phi_{\alpha\beta}(y, y', St, k_z b)$ are confined in the region $(St < 0.4; k_z b < 1)$ and have a well-defined peaks in frequency domain. This implies pseudo-periodic structures in time with large spanwise size $L \sim 1/k_z \geq b$. U- and w-components reveal negative correlations across the jet with positive correlation for v-component at $k_z \approx 0$. W-correlation values are several times smaller than u- and v-correlations.

7.4   Correlation measurements and underlying structures

The negative time-average correlation of u-component fluctuations on opposite sides of planar jet based on the analysis of conventional correlation matrix $R(y, y', x, x', z - z', t - t')$ were noted by Goldschmidt and Bradshaw [59], Everitt and Robbins [46], Cervantes and Goldschmidt [36] ,Mumford [114], Antonia at al [7]. In addition, positive correlation of v-components across the centerline of the jet were noted [7]. Initially these correlations were thought to be an indicator of flapping lateral motion of the jet, similar to a flapping of a flag. But apparent uncorrelated motion of the boundaries of the jet on opposite sides of the jet, revealed in [148] and [112], along with measurements of bulk displacement of the velocity mean profile, conducted in [59], [36], [7] were not supportive of this scenario. Oler and Goldschmidt [115], Mumford [114], Antonia
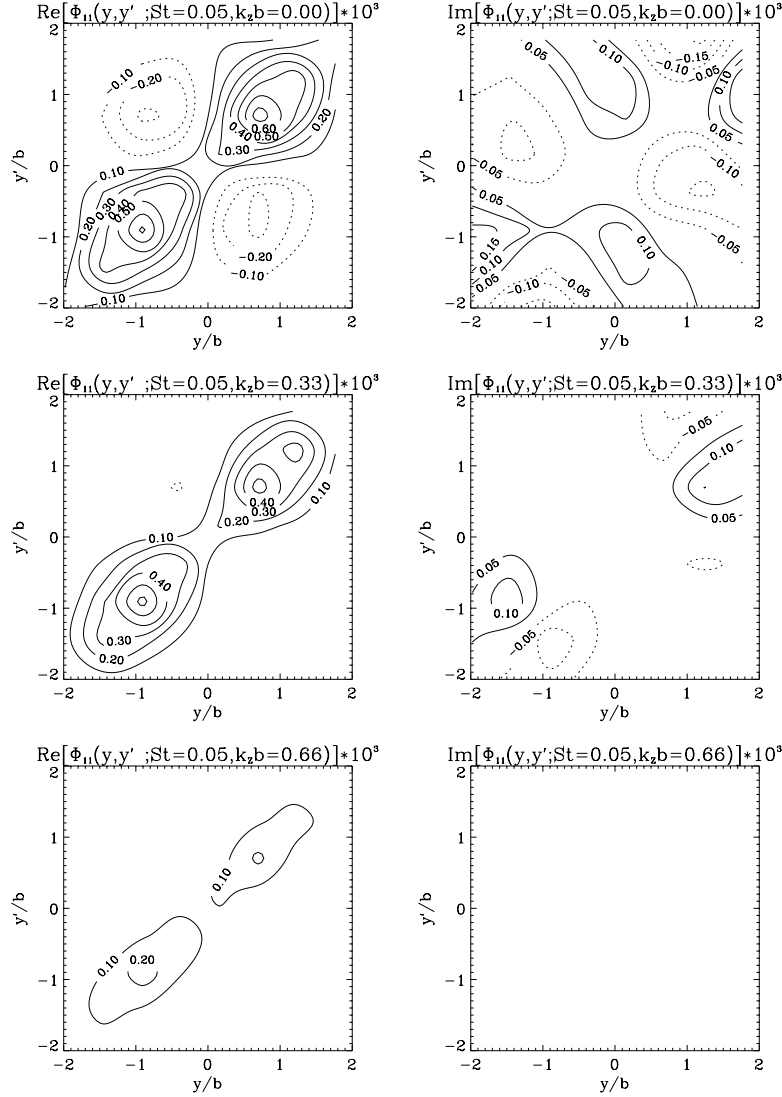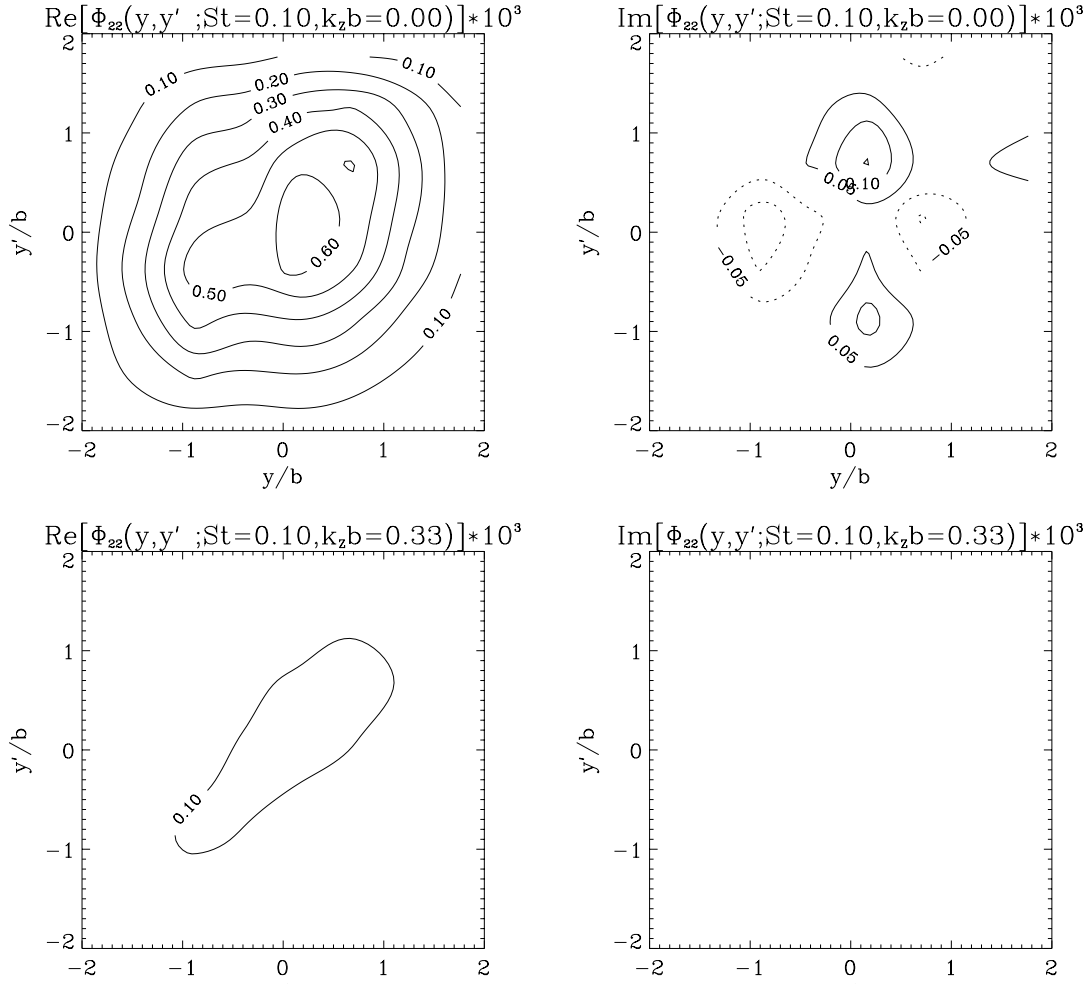
Figure 7.10: The spectral correlation matrix $\Phi_{22}(y, y', St = 0.1, k_z b) \times 10^3$ for $k_z b = 0, 0.33$.

et al [7], [8] had proposed a different scenario consisting of an array of the spanwise roller-like large-scale counter-rotating vortices existing in the jet, similar to a Karman vortex street. The review of early research on large-scale structures in the self-similar region of the jet can be found in [137].

By analyzing space-time correlation functions with probe positioned on opposite sides of the jet, an average time-delay between minima or maxima of passing structures T_{cor} was calculated in [36], [139], [138]. This value was found to evolve in a self-similar fashion downstream such that,

$$St = \frac{b}{T_{cor} U_{\max}} = 0.1 \tag{7.2}$$

These observations provide a strong indication that underlying structures exhibit self-similar behavior in the self-similar region of the jet. This Strouhal number is of the same order as St corresponding to maxima of the spectral correlation, $S_{\alpha\beta}(y, y', St)$, discussed in Section 7.1. Ewing in [48] has theoretically predicted that the evolution of cross-correlations in the self-similar region of the jet admit self-similar solutions. This is a necessary, but not sufficient condition for the dynamics of the jet to be a self-similar one. The sufficient condition is the self-similarity of coherent structures or, in our definition, POD modes.
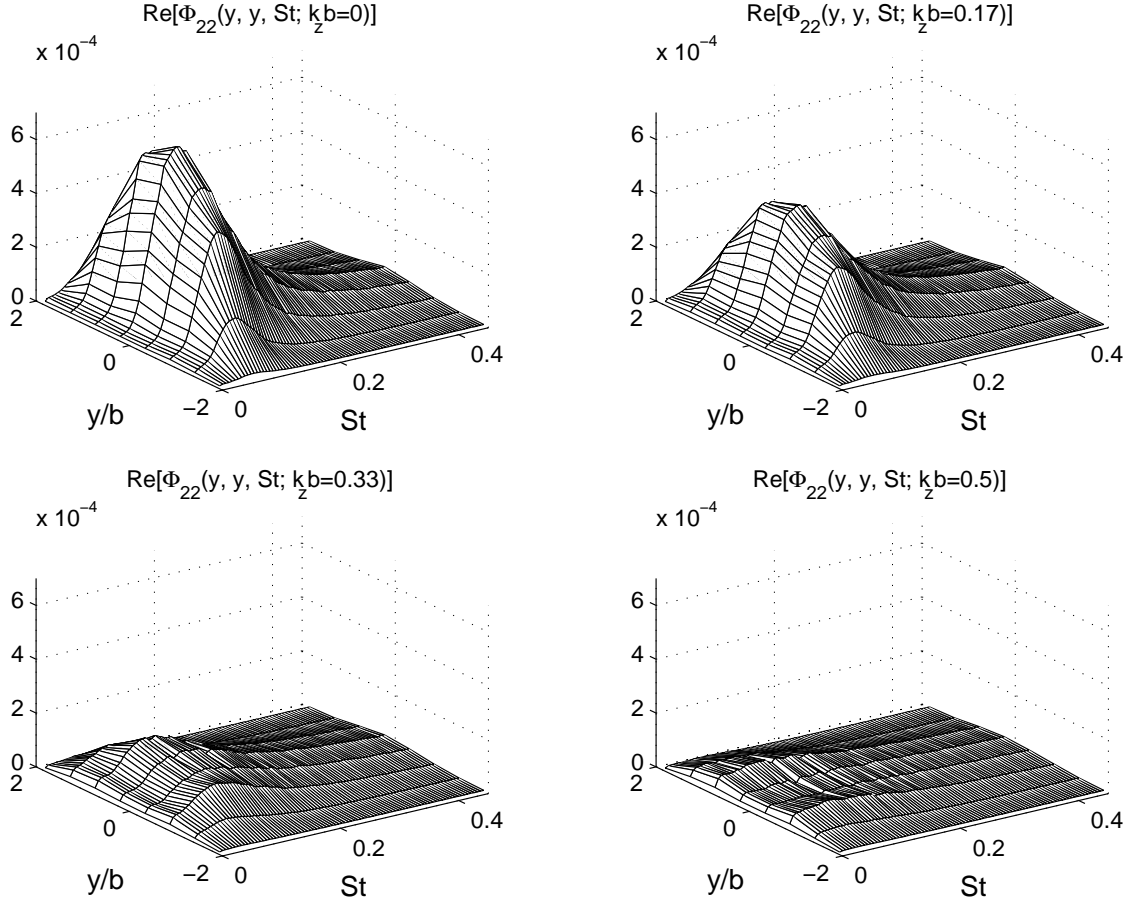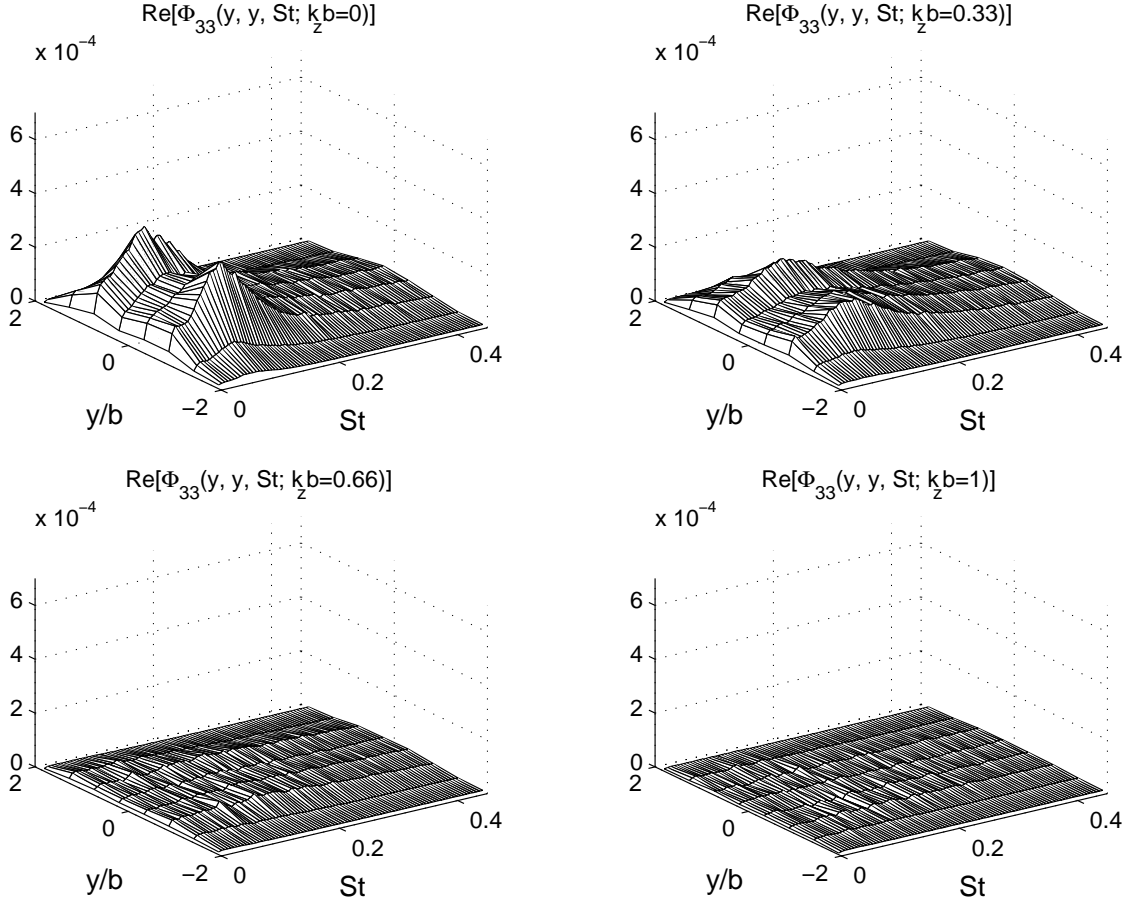
Figure 7.11: The real part of the spectral correlation matrix $Re[\Phi_{33}(y, y, St, k_z b)]$ for $k_z b = 0, 0.33, 0.66, 1$

7.5 POD modes

7.5.1 Two-rake POD modes measurements

In this section the POD eigenfunctions and associated eigenvalues obtained from the solution of equation (6.17) using the experimentally obtained cross-spectral matrix $\Phi_{\alpha\beta}$ are presented. The cross-correlation matrix Φ gives a large-scale correlation, averaged in time among many blocks. It means that POD modes, extracted from Φ-matrix (6.7), will represent *an average shape* of large-scale structures. Furthermore, time and spatial z-direction are transformed into frequency and wavenumber spaces by two Fourier transforms, (6.2), (6.4). Therefore POD modes give an averaged shape of the structure in a mixed physical-Fourier space (y, St, k_z). The reconstruction procedure, which transforms POD modes to a physical domain is described in section 6.7. The reconstruction allows to restore an instantaneous shape of the structures and the results are presented in section 7.7.

To find the POD modes, the equation (6.5) must be solved. This requires determination of all nine components of the cross-spectral matrix, $\Phi_{\alpha\beta}$. Unfortunately, only the five components Φ_{11}, Φ_{12}, Φ_{22}, Φ_{13} and Φ_{33} can be directly measured via the x-wire rakes; the term Φ_{23} is not directly available. However, as will be described in some detail in section 7.7.1, this term can

Figure 7.12: The spectral correlation matrix $\Phi_{33}(y, y', St = 0.14, k_z b) \times 10^3$ for $k_z b = 0, 0.33, 0.66$

be calculated from a knowledge of the other components by means of the continuity equation and by invoking a Taylor's frozen field approximation. The remaining terms Φ_{21}, Φ_{31} and Φ_{23} follow by using the property that the Φ-matrix is Hermitian.

The focus of this section is on the character of the eigenmodes extracted from two-rake experiments and exploration the self-similarity of the underlying large-scale structure in the jet. In order to do this we avoid invoking assumptions required for the solution of (6.5) (e.g. a Taylor's frozen field approximation) and present POD modes calculated using only *the diagonal terms* $\Phi_{\alpha\alpha}$,

$$\int \Phi_{\alpha\alpha}(y, y'; f, k_z) \varphi_\alpha^{(n)}(y'; f, k_z) dy' = \lambda_\alpha^{(n)}(f, k_z) \varphi_\alpha^{(n)}(y; f, k_z). \tag{7.3}$$

It is important to note that the above relation excludes any information contained in the off-diagonal terms, Φ_{12}, Φ_{32}, and so on. Strictly speaking then, the POD modes derived from solving (7.3) and those obtained from solving (6.5) will be different. In fact, they will be the
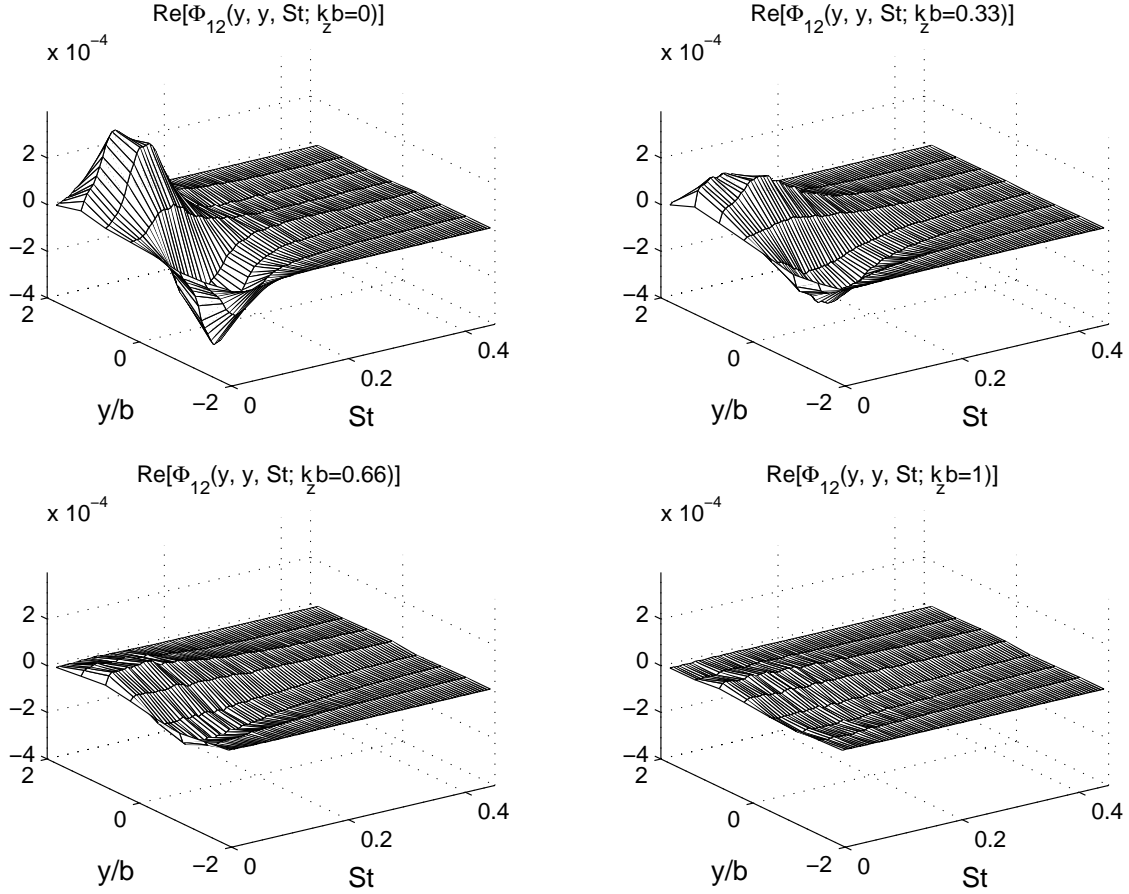
Figure 7.13: The real part of the spectral correlation matrix $Re[\Phi_{12}(y, y, St, k_z b)]$ for $k_z b = 0, 0.33, 0.66, 1$

same only if the off-diagonal terms are zero. Since, as shown in the previous section, Φ_{11} and Φ_{22} dominate the off-diagonal term Φ_{12} we can expect the u- and v-component POD modes obtained by solution of (7.3) to be quite similar to the POD modes obtained by (6.5). In fact, this turns out to be the case as will be shown in section 7.7. In the case of the w-mode the results from the previous section show that Φ_{33} and Φ_{13} are of the same order of magnitude. Hence we can expect a more substantial disparity between the w-component POD modes derived from (7.3) and (6.5). Nevertheless, it is also worth mentioning that the set of w-component POD modes obtained via (7.3) is still complete and can be treated as another completely valid way to investigate the Φ_{33}-term. Thus, while the u and v-component POD modes obtained from (7.3) can shed light onto the shape of the structure, more caution must be exercised in forming conclusions regarding the w-component structure based on the presented w-modes. As it will be discussed in section 7.7, only the w-component POD modes from (6.5), combined with instantaneous phase information obtained from the projection onto the flow field will provide the physical flow structure responsible for the w-component fluctuation.

In summary, the information contained in the off-diagonal terms of the cross-spectral matrix is crucial for modeling the jet dynamics and for reconstructing the large-scale structure in physical space. The focus of this section is on (1) the documentation of the cross-spectral matrix, (2) examination of the basic character of the POD modes in the y, St, k_z domain and

Figure 7.14: The imaginary part of the spectral correlation matrix $Re[\Phi_{12}(y, y, St, k_z b)]$ for $k_z b = 0, 0.33, 0.66, 1$

(3) the exploration of the self-similarity of the POD modes and eigenvalues. To do this we exploit the dominance of the diagonal terms in the cross-spectral matrix and thereby avoid use of a Taylor's frozen field approximation by working with (7.3) instead of (6.5).

Modes φ_α with the corresponding eigenvalues $\lambda_\alpha^{(n)}(St, k_z b; x/D)$ were calculated from (7.3) using (6.17) for each individual $\Phi_{\alpha\alpha}$, $\alpha = 1..3$. Later we will refer to the modes φ_1, φ_2 and φ_3 as u-, v- and w-modes, respectively. As was the case in the presentation of the correlation matrices $S_{\alpha\beta}$ and $\Phi_{\alpha\beta}$, we choose to highlight results obtained at $x/D = 70$ and these may be considered representative. Results obtained at the other streamwise locations will be presented when we examine similarity scaling of the eigenfunctions and eigenvalues.

The eigenvalues for the first and the most energetic u-mode at $x/D = 70$ is presented at Figure 7.19.**a)**. The eigenvalue plots represent the modal energy distribution in Strouhal number-wavenumber domain. The peak u-eigenvalue is located at $(St = 0.05, k_z = 0)$. Essentially all the energy of the first u-mode is concentrated in a low wavenumber range $k_z b \leq 1$, which again suggests an extended(i.e. of order of b) structure in the spanwise direction. The pick in frequency reflects a pseudo-periodic behavior in time.

Because eigenmodes are orthonormal, from (6.7) it is convenient to multiply them by the amplitude corresponding factor $\sqrt{\lambda_\alpha^{(n)}(f, k_z)}$. All modes have been properly scaled using the local maximum velocity U_{max} and the local-half-width b. The details will be given in section
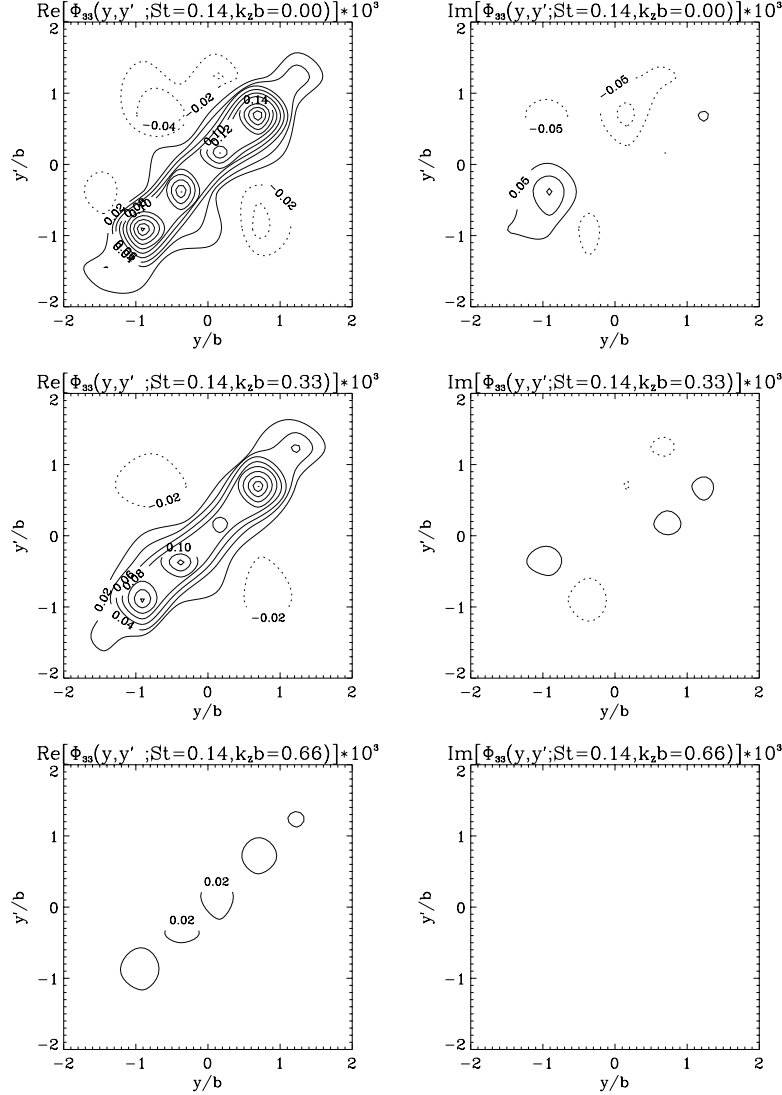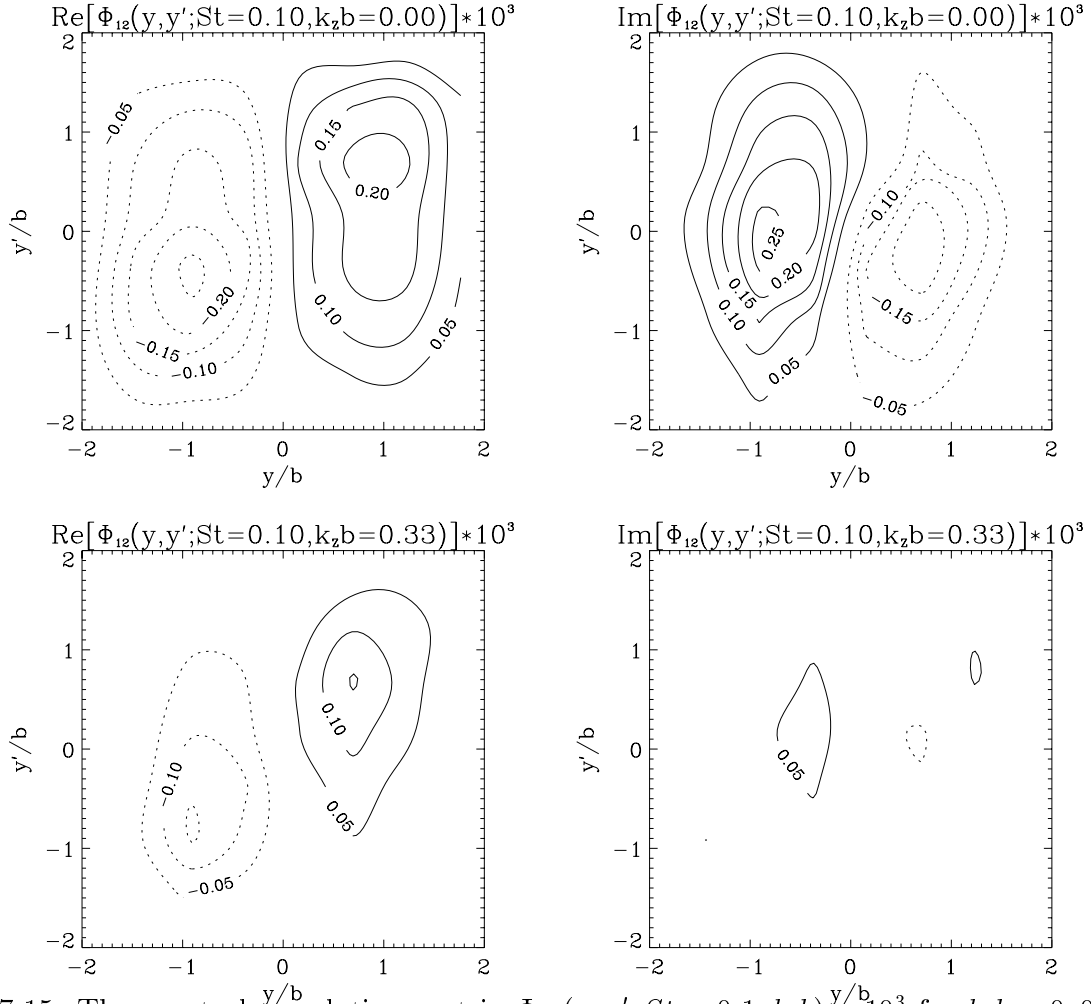
Figure 7.15: The spectral correlation matrix $\Phi_{12}(y, y', St = 0.1, k_z b) \times 10^3$ for $k_z b = 0, 0.33$.

7.6. The square of the modulus of the first u-mode for several wave-numbers $k_z b = 0$, 0.33, 0.66 is shown in Figure 7.19.b), c), and d) The square modulus of the u-mode at $k_z = 0$ is symmetric in the y-direction, which appears as two positive symmetrical 'humps' at $y/b = \pm 1$. For $k_z b = 0.33$ though, the mode reveals an asymmetrical cross-stream pattern, where the mode amplitude on one side of the jet (negative values of y) dominates the opposite side of the jet. A similar trend is seen for $k_z b = 0.66$ wavenumber; however the mode amplitude is smaller here.

The second u-mode is presented in Figure 7.20. The eigenvalue still has a peak at ($St = 0.03$, $k_z = 0$) but the peak has a small flat plateau in the wavenumber direction k_z. Again, however, there is little energy content for $k_z b > 1$. As was the case for u-mode 1, the St band of significant energy content is also rather narrow. The mode at $k_z = 0$ is symmetrical in the y-direction and appears to be slightly asymmetric for $k_z b = 0.33$, with the positive side of the jet dominating another side this time. Figure 7.20.b) presents the scaled modulus-squared of $\varphi_1^{(2)}$ for $k_z = 0$. It is symmetrical in the y-direction. Higher wavenumber modes presented in Figures 7.20.c) and d) reflect a similar cross-stream asymmetry as occurred for first u-mode. For $k_z b = 0.33$ the modal amplitude on the $+y$ side of the jet dominates the $-y$ side. Comparison of this figure with Figure 7.19.c) reveals that the shape of the second mode at $k_z b = 0.33$ is almost a mirror image of the first mode at the same wavenumber. The same can be said of a comparison

58
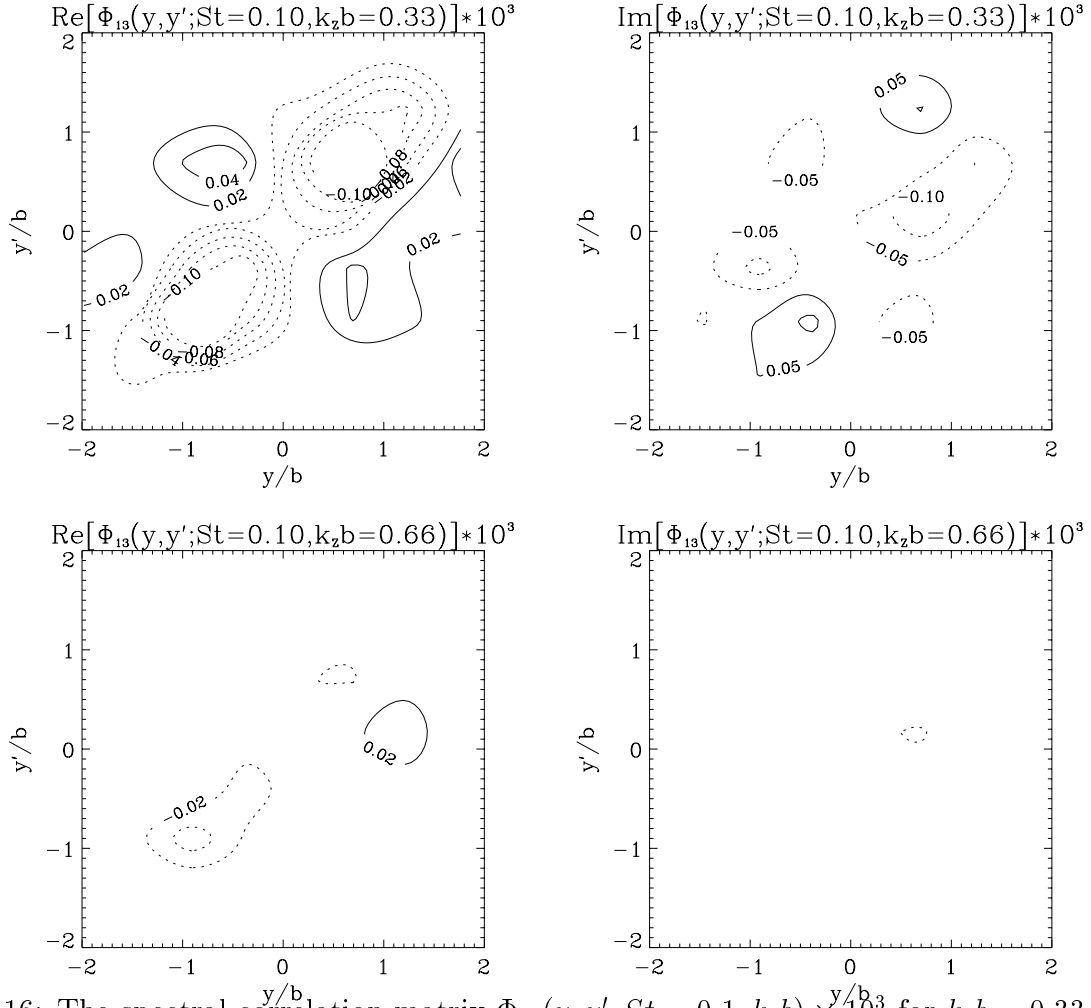
Figure 7.16: The spectral correlation matrix $\Phi_{13}(y, y', St = 0.1, k_z b) \times 10^3$ for $k_z b = 0.33, 0.66$.

between u-mode 1 and 2 shapes at $k_z b = 0.66$ (Figures 7.19.d and 7.20.d). These results suggest the existence of two different physical structures in the jet, namely a planar structures aligned in spanwise direction (for $k_z = 0$) and essentially three-dimensional structures with asymmetrical shape in y-direction and pseudo-periodically distributed in spanwise direction with wavenumbers $k_z b = 0.33..0.66$. An approximate scale of the latter structures in spanwise direction is $L_z \sim 1/k_z \sim 5..10$ inches at $x/D = 70$. These observations are similar to those of Mumford [114], who found evidence of two kinds of vortical structures, planar ones and the vortices aligned in the direction of local strain rate.

The first v-mode is shown in Figure 7.21. The maximum v-eigenvalue occurs at $(St = 0.09, k_z = 0)$. In this case the decrease in energy with increased k_z is much more rapid than for the u-modes previously presented. The v-mode shows a symmetrical behavior in the crosstream direction for $k_z = 0$ and approximately symmetrical shape for non-zero wavenumbers. Figure 7.21 suggests that the first v-mode is essentially planar. The second v-mode in Figure 7.22 clearly exhibits minimum amplitude on the jet centerline and exhibits two peaks near $y/b = \pm 1$. The mode shape is similar for both zero and non-zero spanwise wavenumbers. The associated eigenvalue distribution is shown in Figure 7.22.a). Again the peak occurs at $k_z = 0$ and
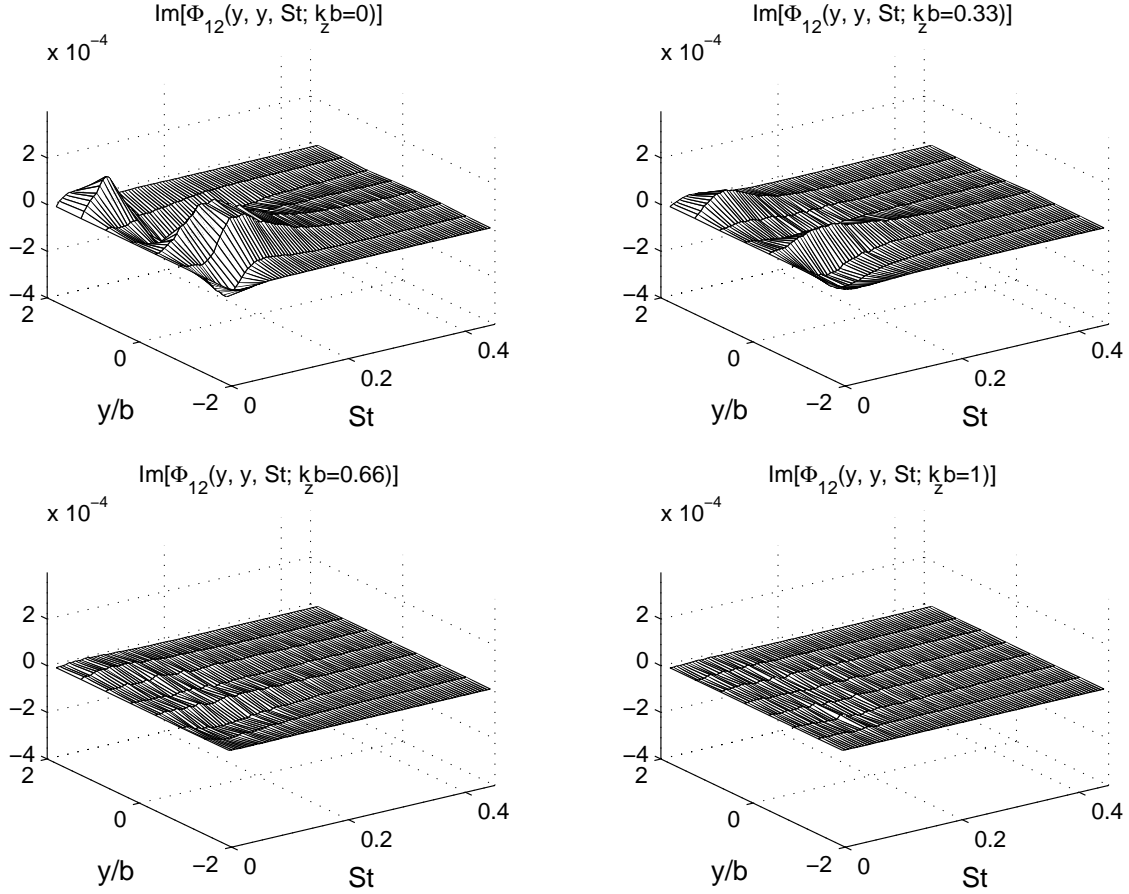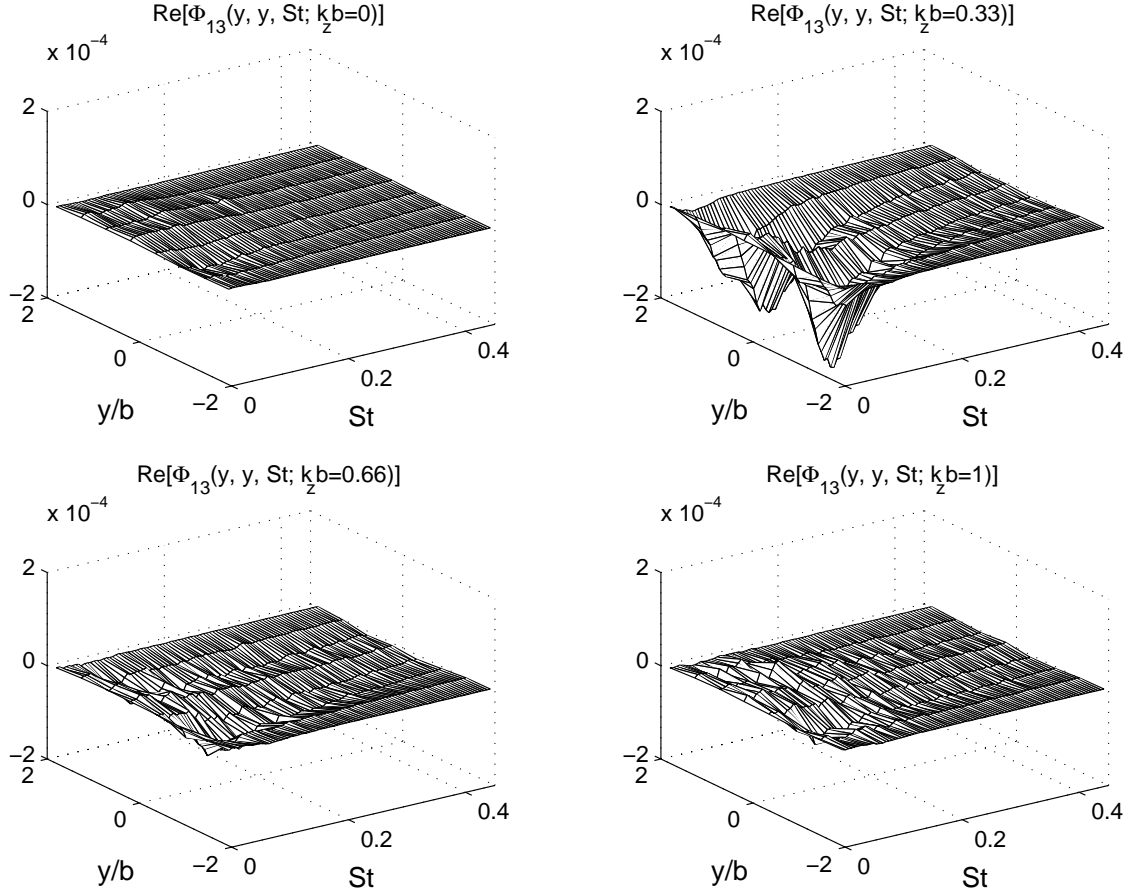
Figure 7.17: The real part of the spectral correlation matrix $Re[\Phi_{13}(y, y, St, k_z b)]$ for $k_z b = 0, 0.33, 0.66, 1$

$St = 0.10$ but the peak eigenvalue is only about one-sixth the value for v-mode 1. The rapid reduction in $\left|\phi_2^{(2)}\right|^2$ with k_z is also indicative of a planar mode.

Finally, the first w-mode is presented in Figure 7.23. The maximum eigenvalue is one-sixth the maximum u-eigenvalue. The eigenvalue peak (Figure 7.23.a) is located at $(St = 0.12, k_z = 0)$. Figures 7.23.b)-d) show that near $St = 0.12$ the w-mode appears symmetrical in the crosstream direction for both zero and non-zero wavenumbers. Its shape exhibits minimum value near the jet centerline and peak values occur near $y/b = \pm 1$. The mode shape at lower St are asymmetric in y. The second w-mode is shown in Figure 7.24 and comparison with Figure 7.23 reveals that its cross-stream shape is basically a mirror image of the first w mode.

7.5.2   Convergence of the POD eigenvalues

We can give consideration to the energy content of the POD modes as expressed through their respective eigenvalues. For a given fluctuating component α, one can investigate the relative amount of energy contained in mode number n expressed as a ratio of the total energy contained within that fluctuating component. That is, the relative energy of the α-component
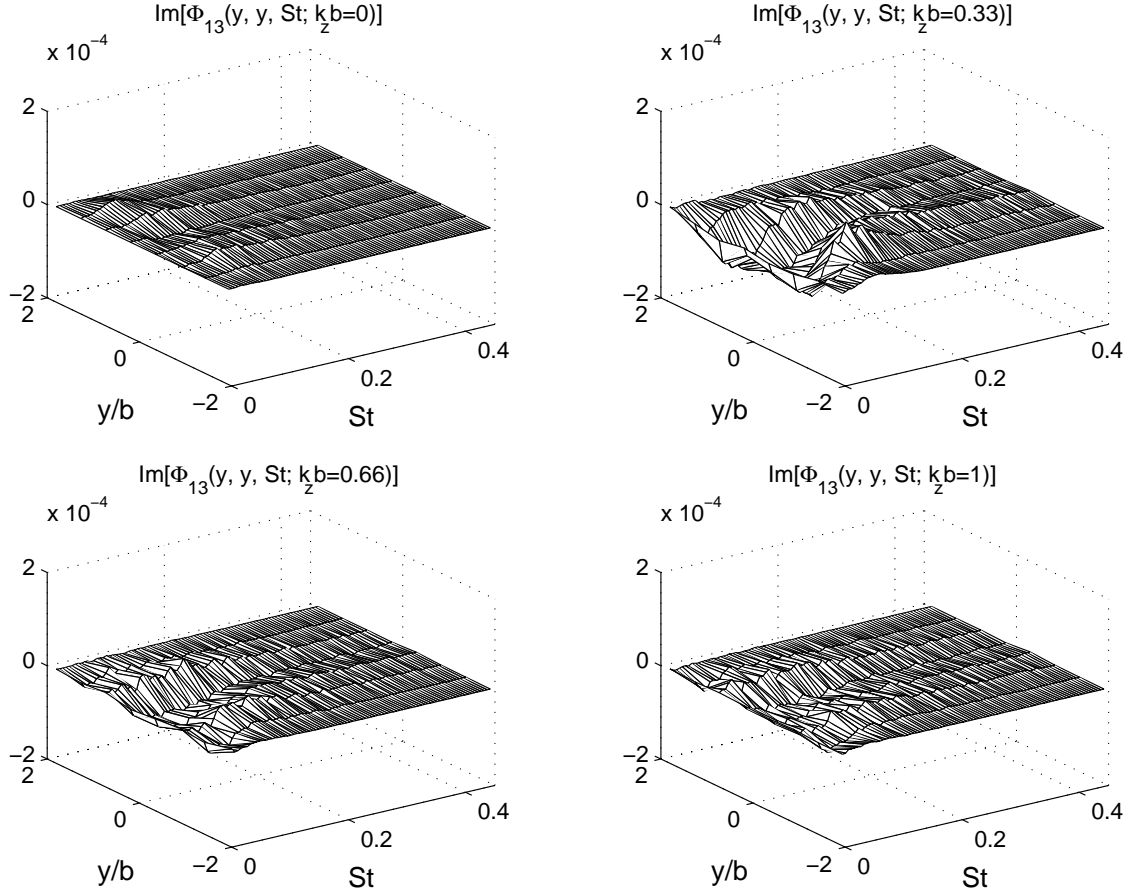
Figure 7.18: The imaginary part of the spectral correlation matrix $Im[\Phi_{13}(y, y, St, k_z b)]$ for $k_z b = 0, 0.33, 0.66, 1$

mode number n is given by,

$$E_R(n; \alpha - mode) = \frac{\sum_{f,k_z} \lambda_\alpha^{(n)}(f, k_z)}{\sum_n \sum_{f,k_z} \lambda_\alpha^{(n)}(f, k_z)} \tag{7.4}$$

Alternately, for a given fluctuating component we can consider the cumulative effect of all modes up to the n-th mode again expressed as a ratio of the total energy in that fluctuating component,

$$E_C(n; \alpha - mode) = \frac{\sum_{k=1}^{n} \sum_{f,k_z} \lambda_\alpha^{(k)}(f, k_z)}{\sum_n \sum_{f,k_z} \lambda_\alpha^{(n)}(f, k_z)} \tag{7.5}$$

Figure 7.25 presents both $E_R(n; \alpha - mode)$ and $E_C(n; \alpha - mode)$ for the u-, v- and w-components. Note that the first u-mode contains approximately 36% of the total energy of the u-component, $\overline{u'^2}$, and the first four modes account for approximately 85% of the total u-component energy. The convergence is even more rapid for the v-component. The first v-mode is responsible for 61% of the v-component energy with the first three modes capturing nearly 90% of $\overline{v'^2}$. The w-component eigenvalues show a slower convergence, with 33% of $\overline{w'^2}$ being contained in the first mode. The first four modes account for over 80% of the total w-component energy in the flow. With regard to the possibility of building a low-dimensional model of the

61
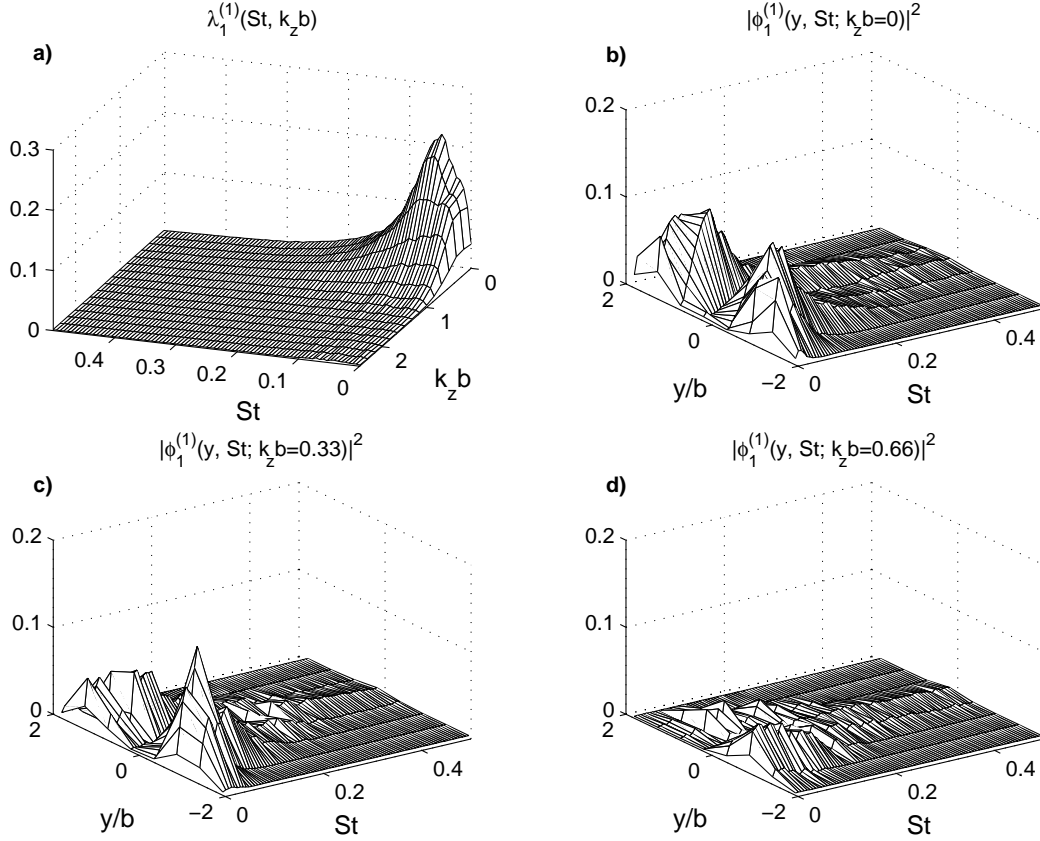
Figure 7.19: The first u-mode: **a)** Eigenvalues $\lambda_1^{(1)}(St, k_z; x/D = 70)$ and the eigenmodes $|\phi_1^{(1)}(y, St, k_z; x/D = 70)|^2$ for for **b)** $k_z b = 0$, **c)** $k_z b = 0.33$ and **d)** $k_z b = 0.66$.

self-similar region of the turbulent planar jet, Figure 7.25 is very encouraging. Considering that this is a fully turbulent shear flow, it is of interest to note that such a large fraction of the fluctuation energy is accounted for by the first 3-4 POD modes and this suggests that Galerkin projection of these modes onto the Navier-Stokes equations could provide the basis for a model that can capture the essential large-scale dynamics of the flow [15], [142], [37].
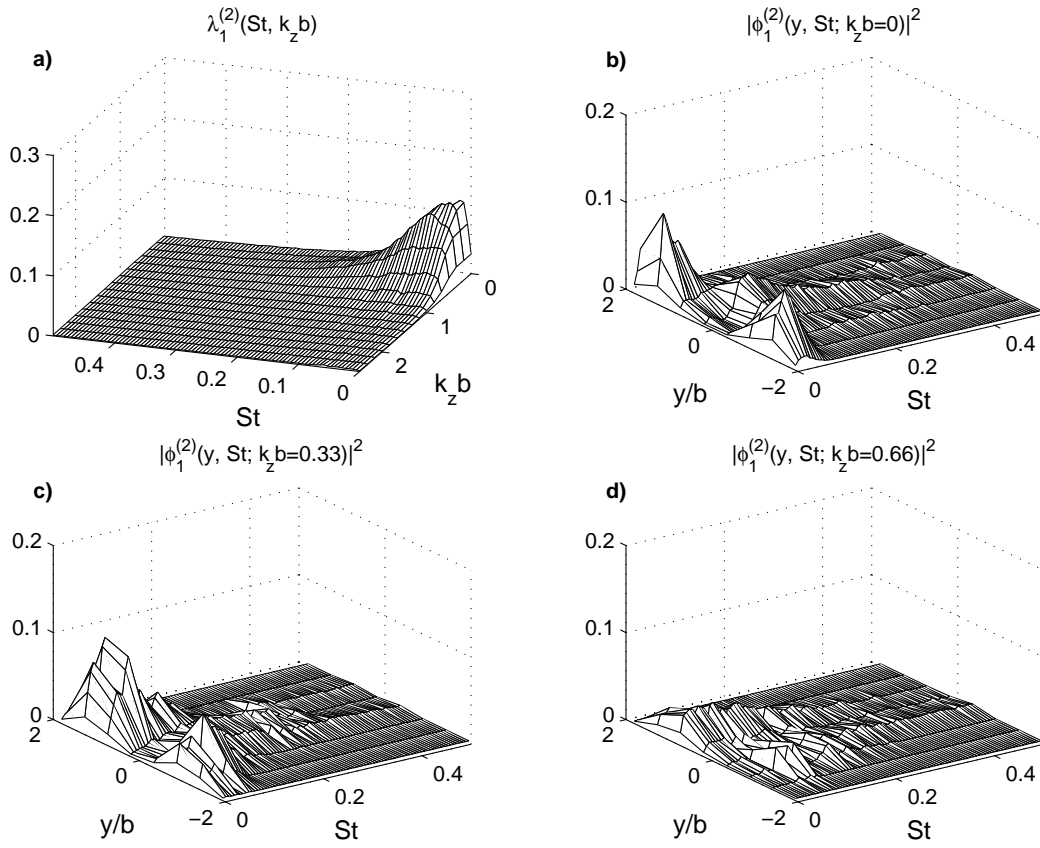
Figure 7.20: The second u-mode: **a)** Eigenvalues $\lambda_1^{(2)}(St, k_z; x/D = 70)$ and the eigenmodes $|\phi_1^{(2)}(y, St, k_z; x/D = 70)|^2$ for for **b)** $k_z b = 0$, **c)** $k_z b = 0.33$ and **d)** $k_z b = 0.66$.
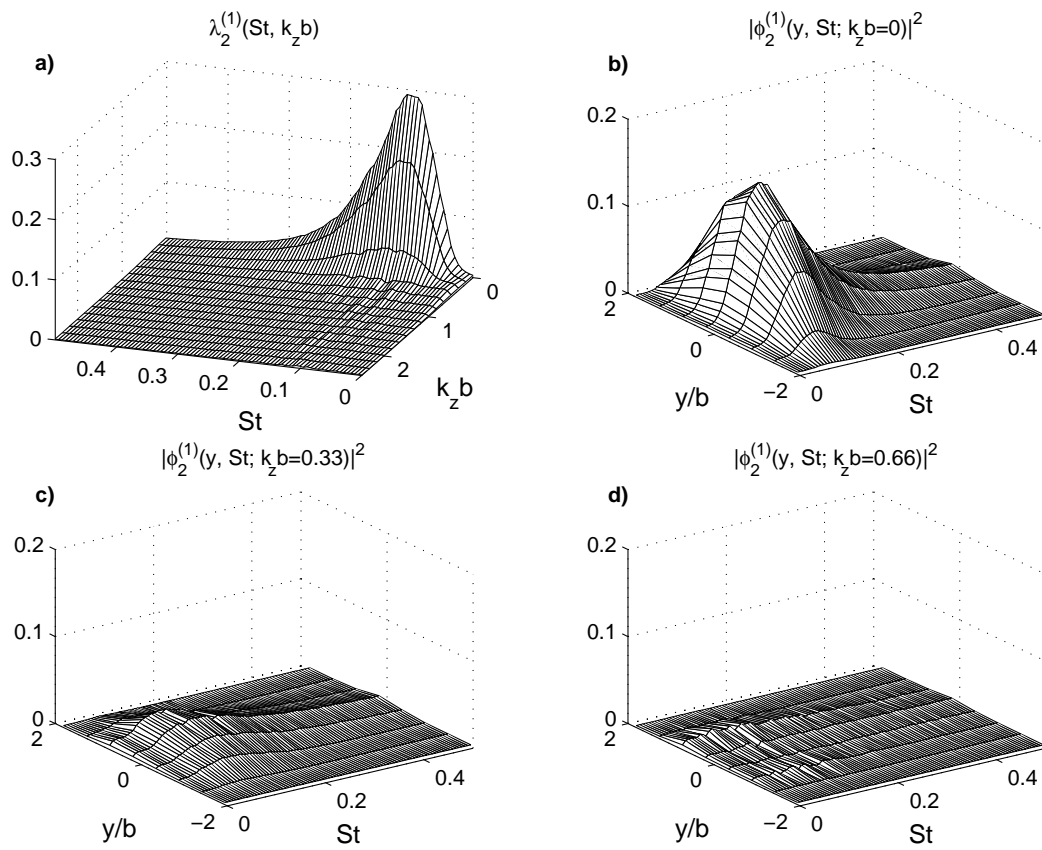
Figure 7.21: The first v-mode: **a)** Eigenvalues $\lambda_2^{(1)}(St, k_z; x/D = 70)$ and the eigenmodes $|\phi_2^{(1)}(y, St, k_z; x/D = 70)|^2$ for for **b)** $k_z b = 0$, **c)** $k_z b = 0.33$ and **d)** $k_z b = 0.66$.
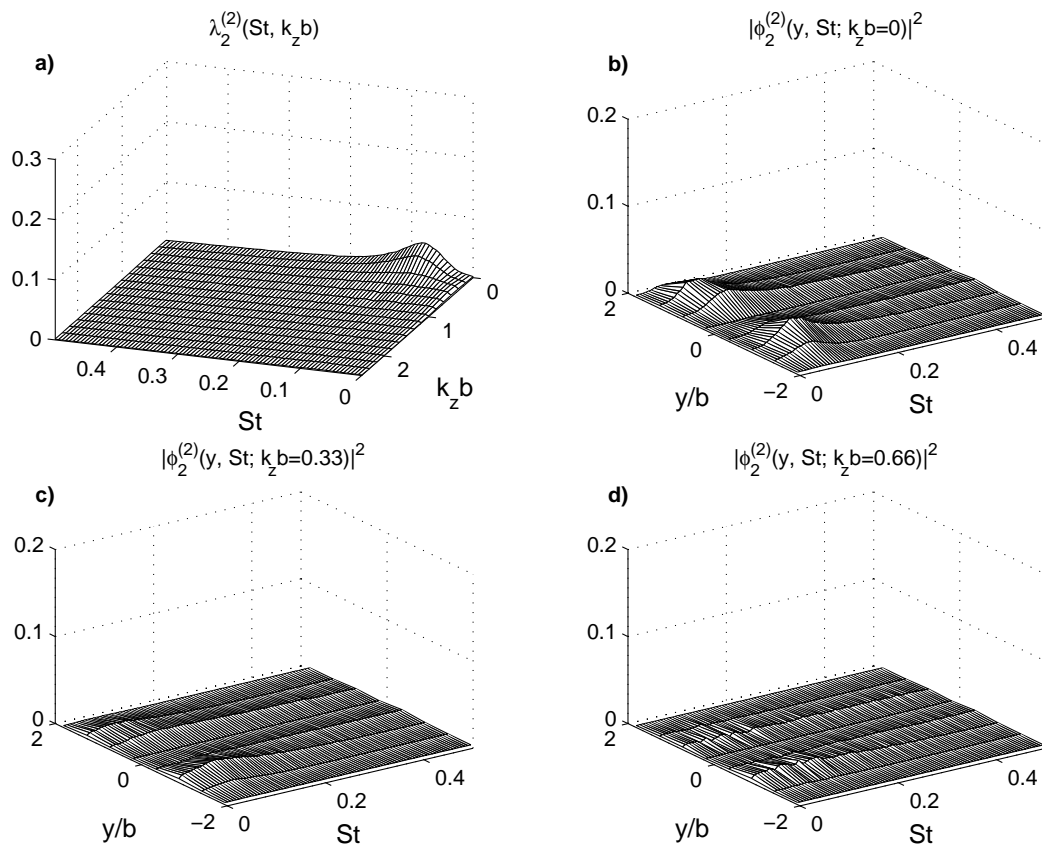
Figure 7.22: The second v-mode: **a)** Eigenvalues $\lambda_2^{(2)}(St, k_z; x/D = 70)$ and the eigenmodes $|\phi_2^{(2)}(y, St, k_z; x/D = 70)|^2$ for for **b)** $k_z b = 0$, **c)** $k_z b = 0.33$ and **d)** $k_z b = 0.66$.
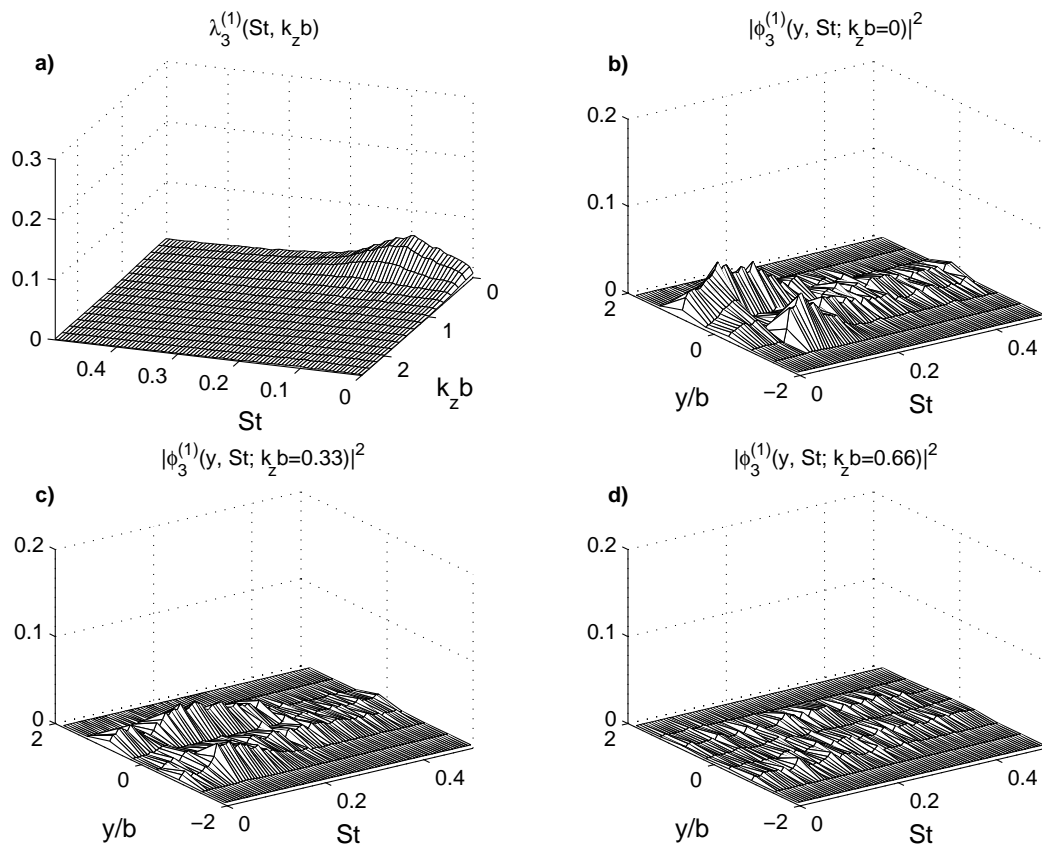
Figure 7.23: The first w-mode: **a)** Eigenvalues $\lambda_3^{(1)}(St, k_z; x/D = 70)$ and the eigenmodes $|\phi_3^{(1)}(y, St, k_z; x/D = 70)|^2$ for for **b)** $k_z b = 0$, **c)** $k_z b = 0.33$ and **d)** $k_z b = 0.66$.
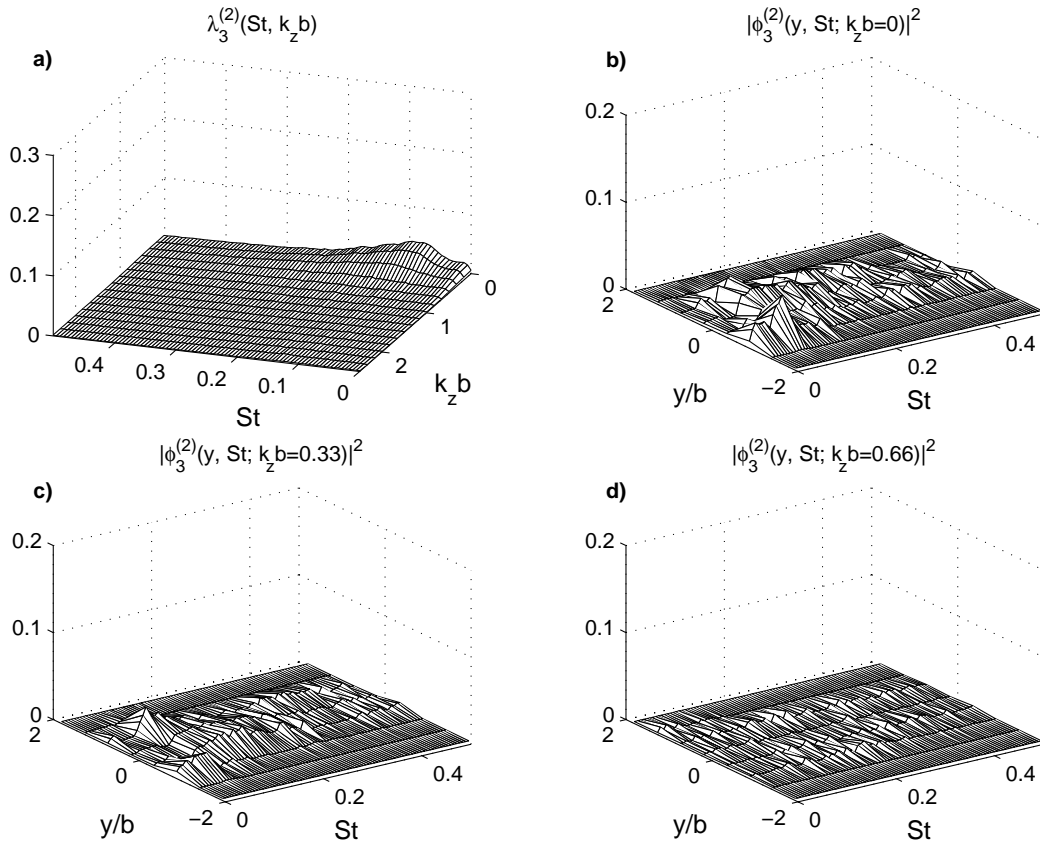
Figure 7.24: The second w-mode: **a)** Eigenvalues $\lambda_3^{(2)}(St, k_z; x/D = 70)$ and the eigenmodes $|\phi_3^{(2)}(y, St, k_z; x/D = 70)|^2$ for for **b)** $k_z b = 0$, **c)** $k_z b = 0.33$ and **d)** $k_z b = 0.66$.
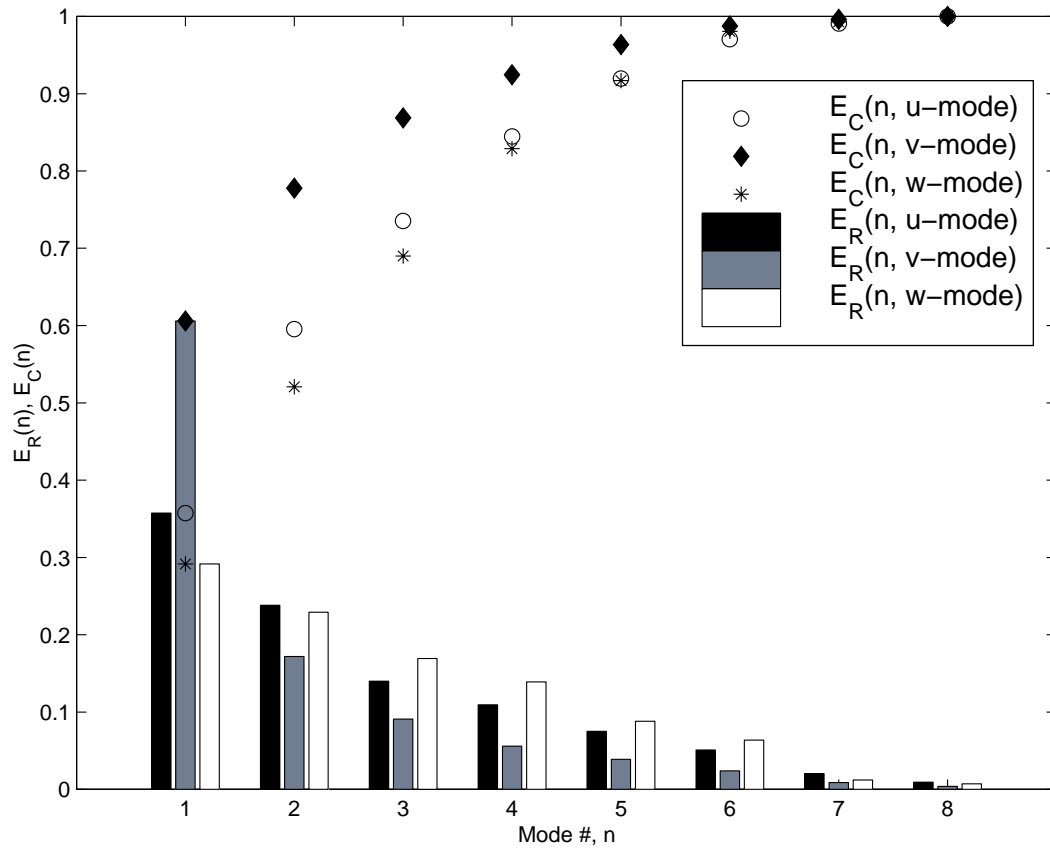
Figure 7.25: Relative $E_R(n, \alpha - mode)$ and Cumulative $E_C(n, \alpha - mode)$ Energies for u-, $v-$ and w-modes.

7.5.3   One-rake POD modes

We consider the two rake implementation of the POD the primary experiment and the most proper way of exploring the structure of the planar jet. This method provides eigenmodes and eigenvalues that exhibit an explicit dependence on spanwise wavenumber, k_z. However, a single rake implementation of the POD was also performed in support of the primary experiment as described in section 7.5.1. This was motivated by the fact that many previous investigations in the planar jet have utilized probes confined to a single $x - y$ plane. In addition, the single rake implementation allows a larger number of probes to be placed in the inhomogeneous direction and thereby enables eigenmode resolution issues to be addressed.

In this section the single rake POD modes $\psi_\alpha^{(n)}(y/b; St)$ with corresponding eigenvalues $\mu_\alpha^{(n)}(St)$ as computed from (6.24) for the diagonal terms $S_{\alpha\alpha}$ are presented and compared to results from the two rake experiment. Note that in the single rake experiment the resulting eigenfunctions are not explicit functions of spanwise wavenumber k_z but depend only on Strouhal number, St, and the inhomogeneous spatial coordinate y. Since the one-rake experiment does not resolve the spanwise direction, the resulting POD modes will represent a weighted sum of the two-rake POD modes previously presented.
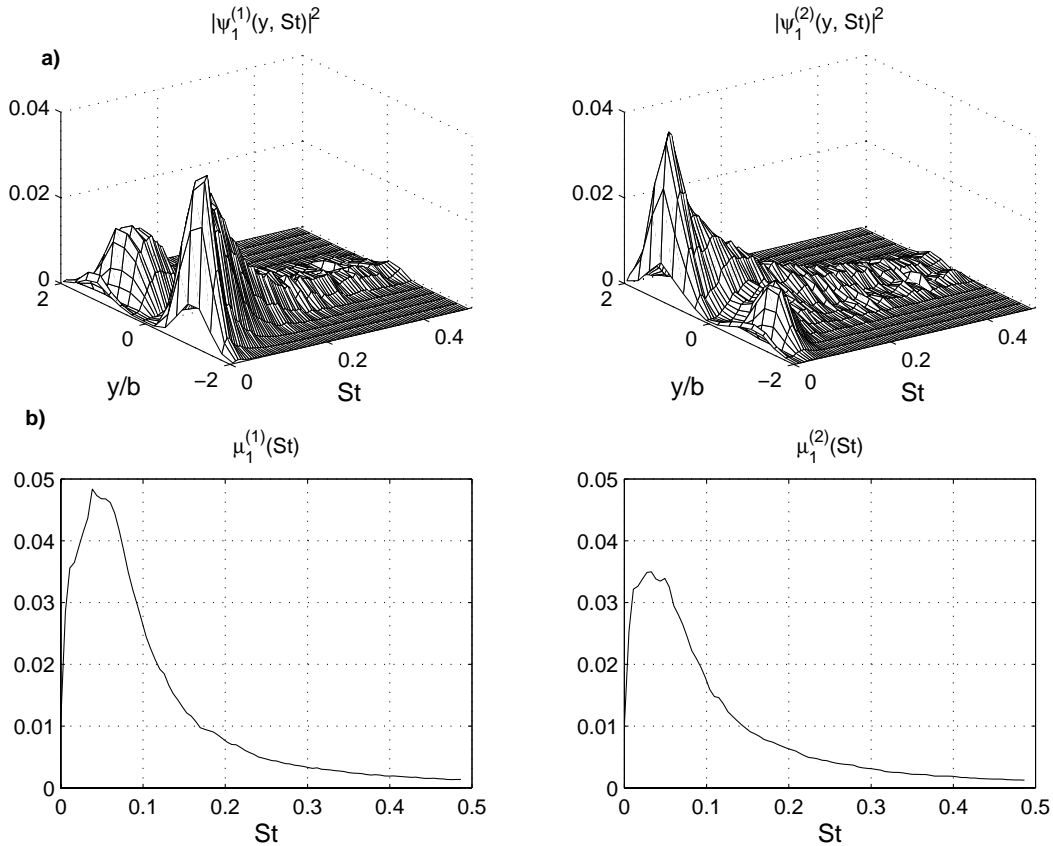
Figure 7.26: The first two one-rake u-modes $\psi_1^{(n)}(y, St; x/D)$ with the corresponding eigenvalues $\mu_1^{(n)}(St; x/D)$, $n = 1, 2$ at $x/D = 70$

Figure 7.26a presents $\left|\psi_1^{(1)}(y; St)\right|^2$ and $\left|\psi_1^{(2)}(y; f)\right|^2$ as obtained at $x/D = 70$. The associated eigenvalues $\mu_1^{(1)}(St)$ and $\mu_1^{(2)}(St)$ are presented in Figure 7.26b. A cross-stream asymmetry

in both eigenmodes is apparent from Figure 7.26a. Note, in particular, that values of $\left|\psi_u^{(1)}\right|^2$ are greater for $-y$ than for $+y$. The opposite is true for $\left|\psi_u^{(2)}\right|^2$. Recall from the two-rake POD results that the first two u-component eigenmodes also exhibited an identical cross-stream asymmetry *for nonzero spanwise wavenumbers*. This may be seen by comparing Figure 7.26a with Figures 7.19c,d and 7.20c,d. Since the one rake results presented here represent a weighted sum over all spanwise wavenumbers, the cross-stream asymmetry is an expected consequence of the contribution of the nonzero k_z modes. Similarly comparison of Figure 7.26a with Figures '7.19b and 7.20b clearly demonstrate that *single rake measurements do not properly capture planar modes*. Figure 7.26b shows that the peak eigenvalues $\mu_1^{(1)}$ and $\mu_1^{(2)}$ occur at $St = 0.04$ and $St = 0.03$, respectively. These values are quite similar to those obtained in the two rake experiment.
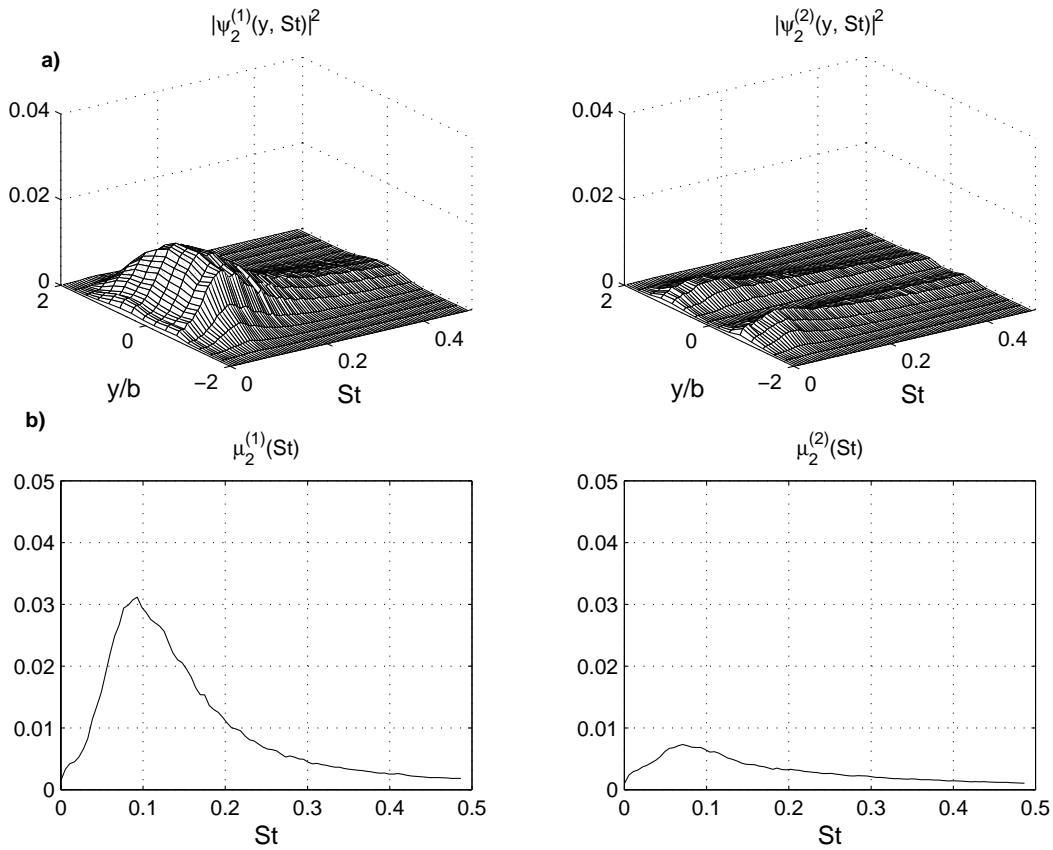
Figure 7.27: The first two one-rake v-modes $\psi_2^{(n)}(y, St; x/D)$ with the corresponding eigenvalues $\mu_2^{(n)}(St; x/D)$, $n = 1, 2$ at $x/D = 70$

The v-component eigenmodes $\left|\psi_2^{(1)}(y, St)\right|^2$ and $\left|\psi_2^{(2)}(y, St)\right|^2$ are presented in Figure 7.27a and both are observed to be symmetric in y. This is expected since the first and second POD modes from the two-rake experiment as shown in Figures 7.21 and 7.22 are also both symmetric in y. Note, however, that their are differences in the mode shapes between the two experiments. For example Figure 7.27a shows the $\left|\psi_2^{(1)}(y, St)\right|^2$ mode shape to exhibit a broader peak near the jet centerline than is shown in Figure 7.21b. This difference is most likely due

70

to the contribution of nonzero spanwise wavenumber modes. Figure 7.27b shows that peak eigenvalues $\mu_2^{(1)}$ and $\mu_2^{(2)}$ occur at $St = 0.09$ and $St = 0.07$, respectively.
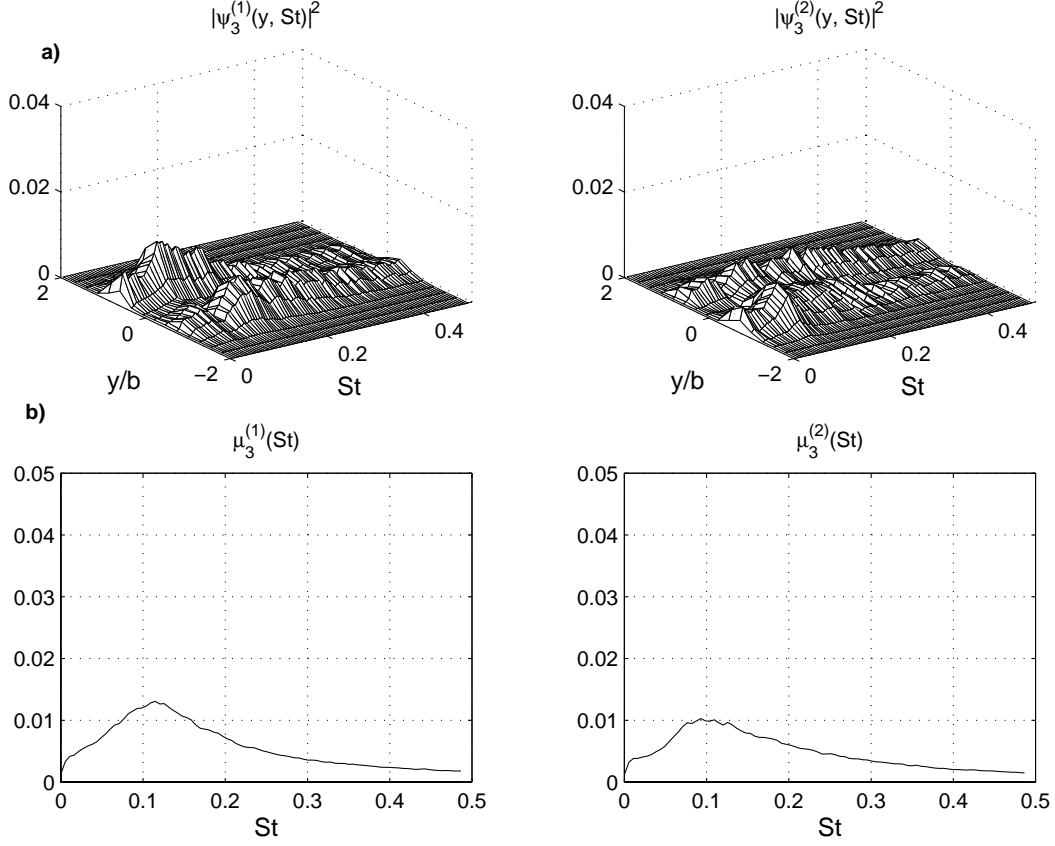
Figure 7.28: The first two one-rake w-modes $\psi_3^{(n)}(y, St; x/D)$ with the corresponding eigenvalues $\mu_3^{(n)}(St; x/D)$, $n = 1, 2$ at $x/D = 70$

Figure 7.28a presents $\left|\psi_3^{(1)}(y, St)\right|^2$ and $\left|\psi_3^{(2)}(y, St)\right|^2$. Their respective shapes are observed to be quite similar to those shown previously in Figures 7.23 and 7.24 for $\left|\phi_3^{(1)}(y, St; k_z = 0)\right|^2$ and $\left|\phi_3^{(2)}(y, St; k_z = 0)\right|^2$. The peak eigenvalues $\mu_3^{(1)}$ and $\mu_3^{(2)}$ occur at $St = 0.12$ and $St = 0.1$, respectively.

7.6 Self-similarity of POD modes

In this section we investigate the self-similarity of the POD eigenvalues and eigenmodes by application of suitable scaling. To answer the question about the self-similarity of the two-rake POD modes, all quantities should be properly scaled. The dimension of $R_{\alpha\beta}$ (6.4) is $[m^2/\sec^2]$, and since $\Phi_{\alpha\beta}$ is a Fourier transform of $R_{\alpha\beta}$ in time t and space z, the appropriate dimensions of $\Phi_{\alpha\beta}$ is $[m^2/\sec^2 \cdot m \cdot \sec] = [m^3/\sec]$. From (6.5) it follows that the dimension of λ is $[m^4/\sec]$. Thus, the appropriate scaling for λ is $b^3 U_{max}$ and eigenvalues can be written in the following non-dimensional form,
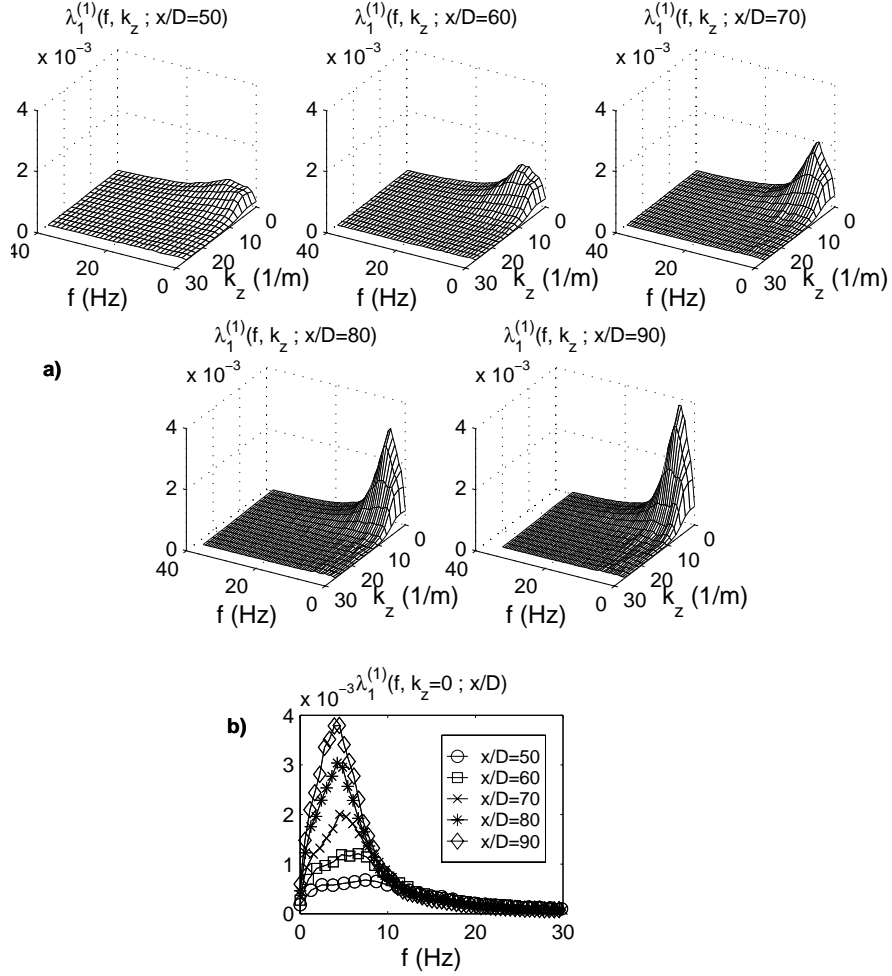
Figure 7.29: Unscaled eigenvalues $\lambda^{(1)}(f, k_z; x/D)$ for the first u-mode for several x/D-stations.

$$\lambda^{(n)}(f, k_z; x/D) = b^3 U_{max} \tilde{\lambda}^{(n)}(St, k_z b; x/D) \tag{7.6}$$

The appropriate non-dimensionalization for the POD modes will be

$$\sqrt{\lambda_\alpha^{(n)}(f, k_z; x/D)}\varphi_\alpha^{(n)}(y; f, k_z, x/D) = \sqrt{b^3 U_{max}\tilde{\lambda}_\alpha^{(n)}(St, k_z b; x/D)}\varphi_\alpha^{(n)}(y/b; St, k_z b, x/D). \tag{7.7}$$

An example of the measured eigenvalue variation over the streamwise distance covered in this experiment is presented in Figure 7.29. In particular, Figure 7.29a shows the streamwise variation of $\lambda_1^{(1)}(f, k_z; x/D)$, the *unscaled* u-component mode 1 eigenvalues over the streamwise range $50 \leq x/D \leq 90$. This figure shows that the maximum unscaled eigenvalue increases in magnitude and shifts to smaller frequencies with increased streamwise distance. This is also apparent readily from Figure 7.29b which highlights the streamwise development of the $k_z = 0$ (i.e. a planar mode) u-component mode 1 eigenvalues.

If the POD eigenmodes and eigenvalues exhibit self-similarity then after a suitable rescaling (7.6) and (7.7), we must have congruence of both the non-dimensional eigenvalues $\tilde{\lambda}_\alpha^{(n)}(St, k_z b; x/D)$ in $St - k_z b$ space and the eigenfunction in $y/b, St, k_z b$ space.

<center>72</center>

Since the eigenvalues form surfaces in $St-k_z$ space this poses a bit of a challenge in providing a meaningful comparison at different x/D stations. One way of performing such a comparison is to 'slice' each of the eigenvalue surfaces at selected values of St and compare their variation with spanwise wavenumber k_z at each streamwise position. Alternately, we may slice the surfaces at selected k_z and compare their variation with Strouhal number at each streamwise location. Both approaches are taken in the results presented next.
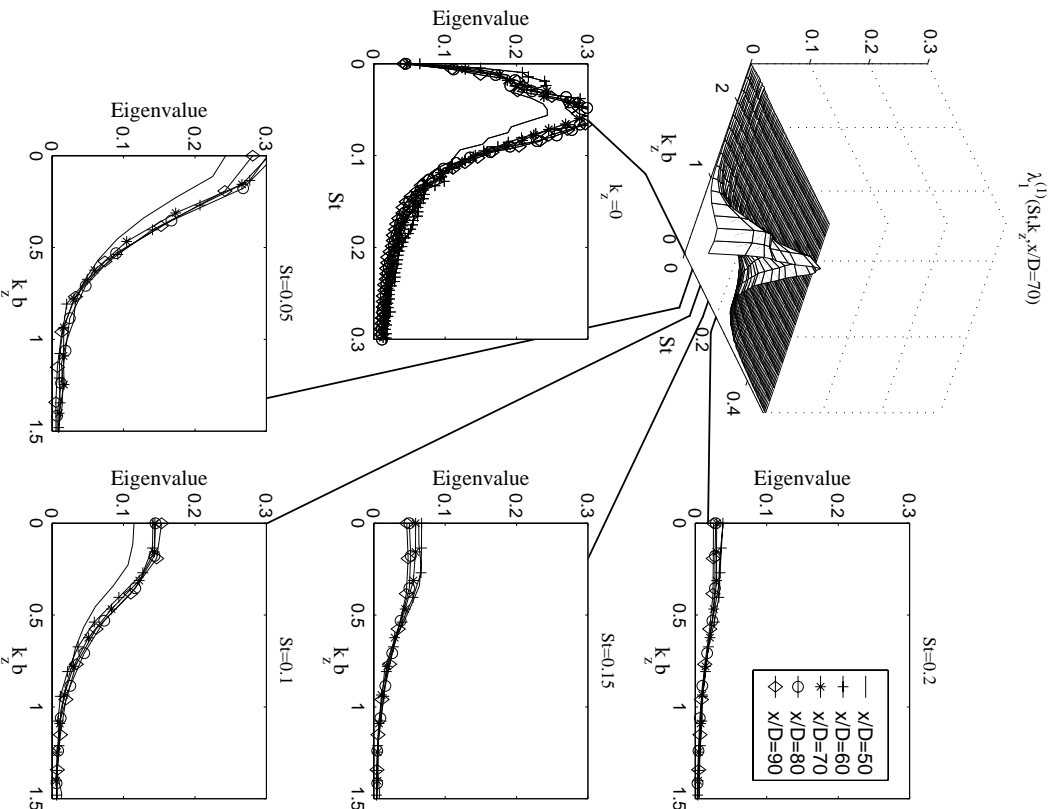
Figure 7.30: Scaled eigenvalues $\tilde{\lambda}_1^{(1)}(St, k_z b; x/D)$ for the first u-mode.

Figure 7.30 presents the scaled mode 1, u-component eigenvalues. For reference, the scaled eigenvalue distribution in $St, k_z b$ space at $x/D = 70$ is shown in order to indicate the location of the "slices" taken for the associated plots. The figure shows the variation of the planar mode ($k_z = 0$) eigenvalues, $\tilde{\lambda}_1^{(1)}$, with St for $50 \leq x/D \leq 90$. In addition, the variation of $\tilde{\lambda}_1^{(1)}$ with $k_z b$ is shown for four representative values of St over the same streamwise locations. This figure shows quite convincingly that the scaled u-component eigenvalue distribution becomes self-similar for $x/D > 50$ as evidenced by the congruence of the scaled profiles at the different x/D stations. The reader is invited to compare the scaled planar mode eigenvalue $\tilde{\lambda}_1^{(1)}$ variation with St shown in Figure 7.30 with the unscaled version shown previously in Figure 7.29b. The
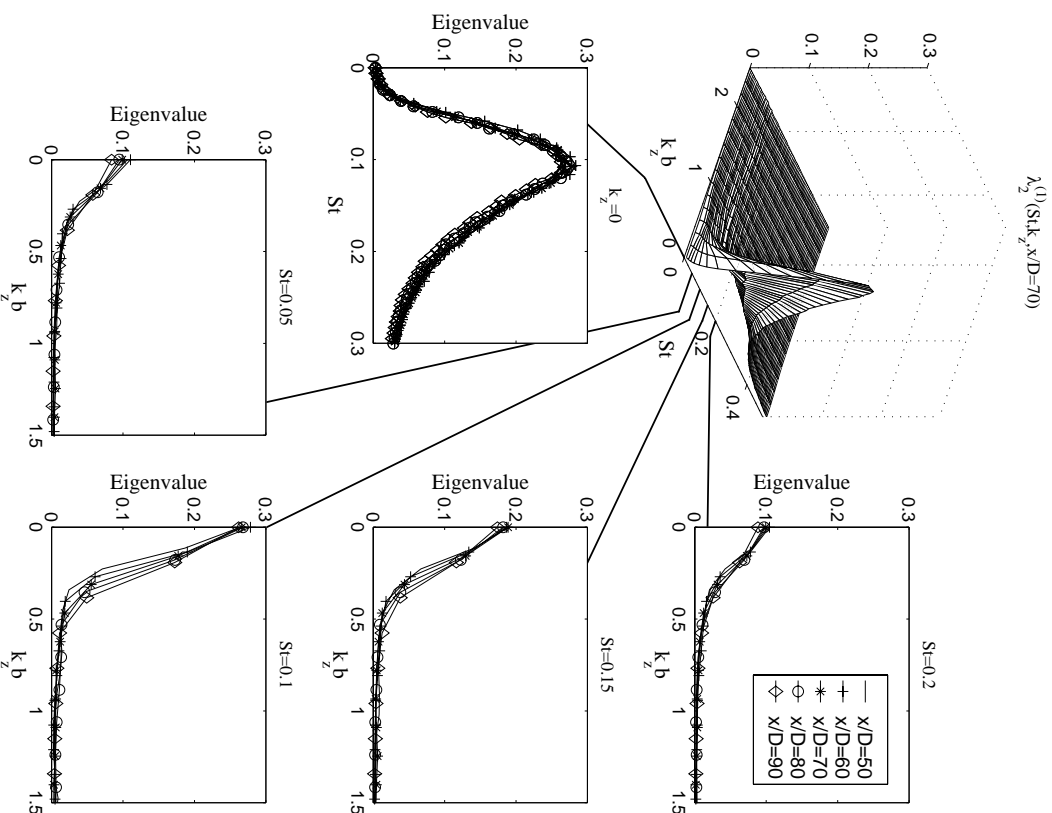
Figure 7.31: Scaled eigenvalues $\tilde{\lambda}_2^{(1)}(St, k_z; x/D)$ for the first v-mode.

effect of the similarity scaling in collapsing the eigenvalues at the various streamwise locations is obvious.

Figure 7.31 shows a similar representation of the scaled mode 1, v-component eigenvalues, $\tilde{\lambda}_2^{(1)}$. The variation of the planar mode ($k_z = 0$) eigenvalues with St for selected streamwise locations is shown to exhibit similarity. In addition, the variation with spanwise wavenumber $k_z b$ for selected St also exhibits collapse for the various x/D locations shown. Figure 7.31 shows that the v-component mode 1 eigenvalues exhibit similarity scaling for $x/D \geq 50$.

The scaled, u-component, mode 1 eigenvalues are shown in Figure 7.32. These figures also show evidence of self-similar behavior for $\tilde{\lambda}_3^{(1)}$. However, unlike the u and v-components, significant differences in the eigenvalue profiles remain apparent at $x/D = 50$ and 60. These data suggest that self-similar behavior for the u-component eigenvalues occurs only for $x/D > 60$.

The scaled eigenvalues associated with higher u, v, and w-component modes were also found to exhibit a collapse similar to that documented for mode 1. The reader is referred to Appendix E for a full presentation of the results for the second POD mode.

In order to assess the self-similarity of the scaled POD eigenmodes, cross-stream profiles at selected streamwise locations may be compared for given values of St and $k_z b$. Such comparisons were made for numerous combinations of St and k_z and a sample of representative results are presented here. Figure 7.33 presents $|\phi_1^{(1)}(y/b; St, k_z = 0, x/D)|^2$ and $|\phi_1^{(2)}(y/b; St, k_z = 0, x/D)|^2$ for $St = 0.05, 0.1$ and $50 \leq x/D \leq 90$. These results illustrate the self-similarity in cross-stream u-component scaled eigenmode shape that was found to characterize the other combinations as well.

Figure 7.34 presents similar results for the first two v-component eigenmode profiles. Again the comparison is shown for the planar mode, $k_z = 0$, with $St = 0.05, 0.1$. The self-similarity in v eigenmode profile shape is again readily apparent.

The first scaled u-component eigenmode cross-stream profile is shown in Figure 7.35. This mode exhibits evidence of similarity scaling (except at $x/D = 50, 60$ as noted previously). Only the first mode is shown since the second mode is of such low amplitude in comparison as well as the fact that the eight probe rake is probably incapable or properly resolving the

Figure 7.32: Scaled eigenvalues $\tilde{\lambda}_3^{(1)}(St, k_z; x/D)$ for the first u-mode.

75
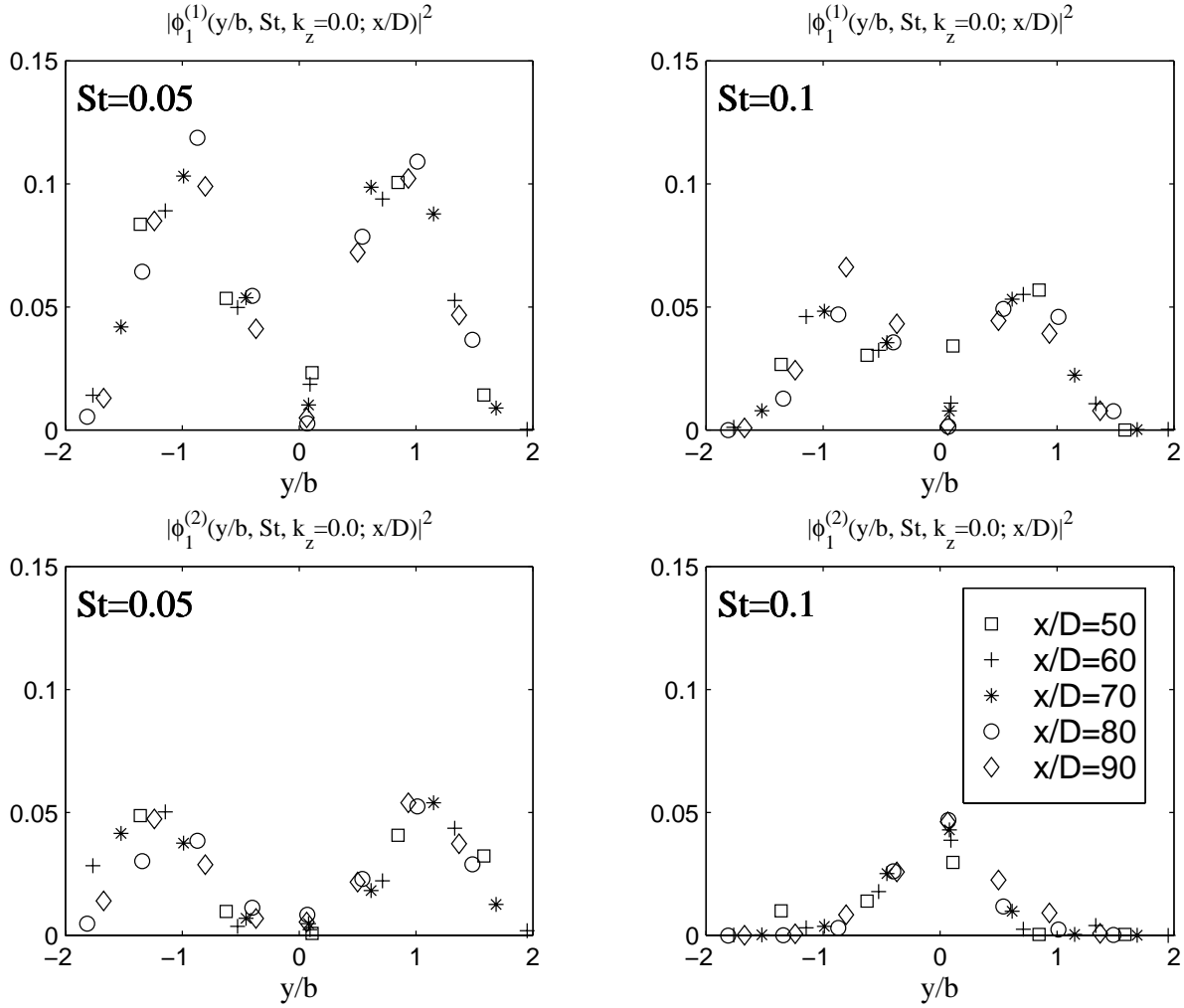
Figure 7.33: Scaled u-eigenmode $|\phi_1^{(n)}(y/b, St, k_z = 0; x/D)|^2$, n=1,2.

cross-stream shape of the higher w-modes as noted in section 6.2. By proving the self-similarity of the POD modes, the self-similarity of S- and Φ-matrices follow from (6.7) and (6.4). It experimentally verifies the theoretical prediction of the self-similarity of the cross-correlation matrix by Ewing [48]. Furthermore, as the dynamics of the jet can be expanded in terms of POD-modes (Chapter 8), we can conclude that the dynamics of the jet and an average shape of large-scale structures in self-similar region are self-similar after $x/D \geq 50$.
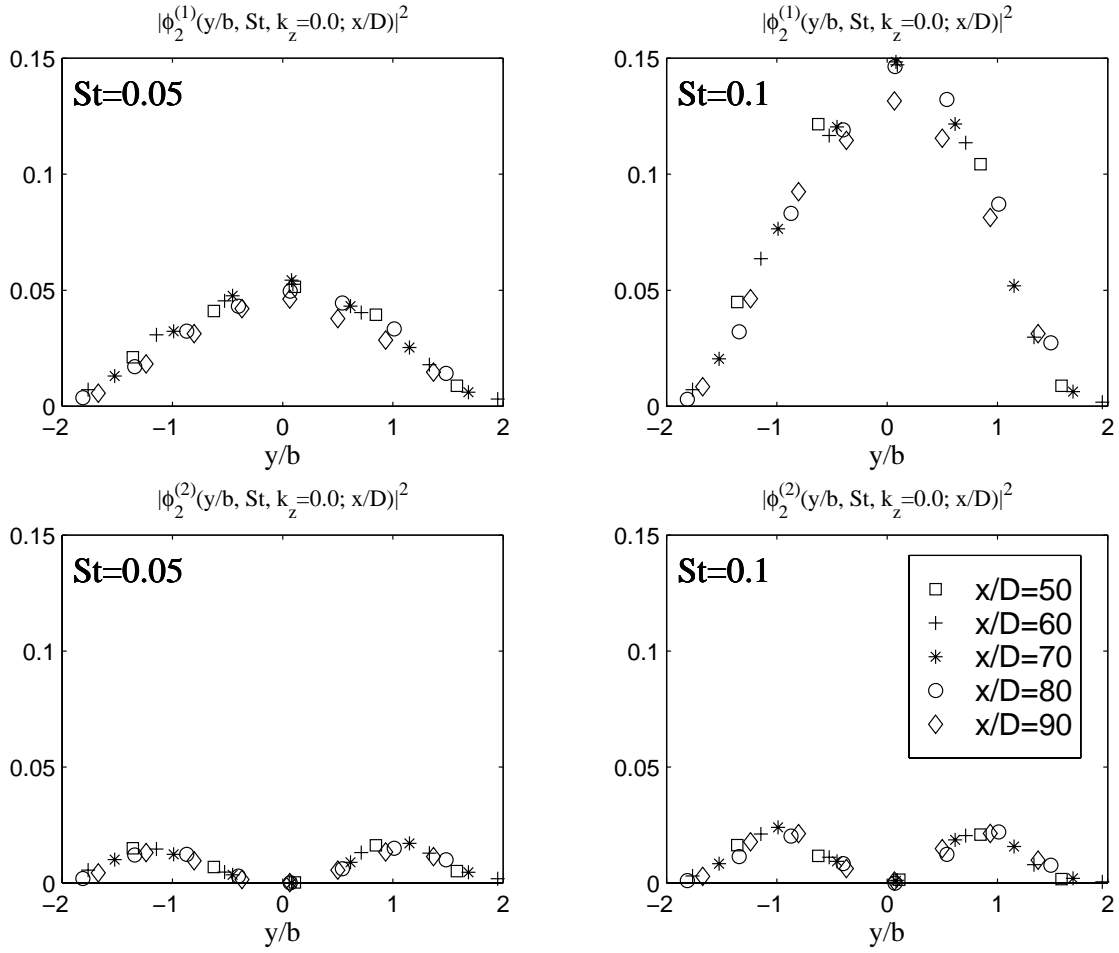
Figure 7.34: Scaled v-eigenmode $|\phi_2^{(n)}(y/b, St, k_z = 0; x/D)|^2$, n=1,2.
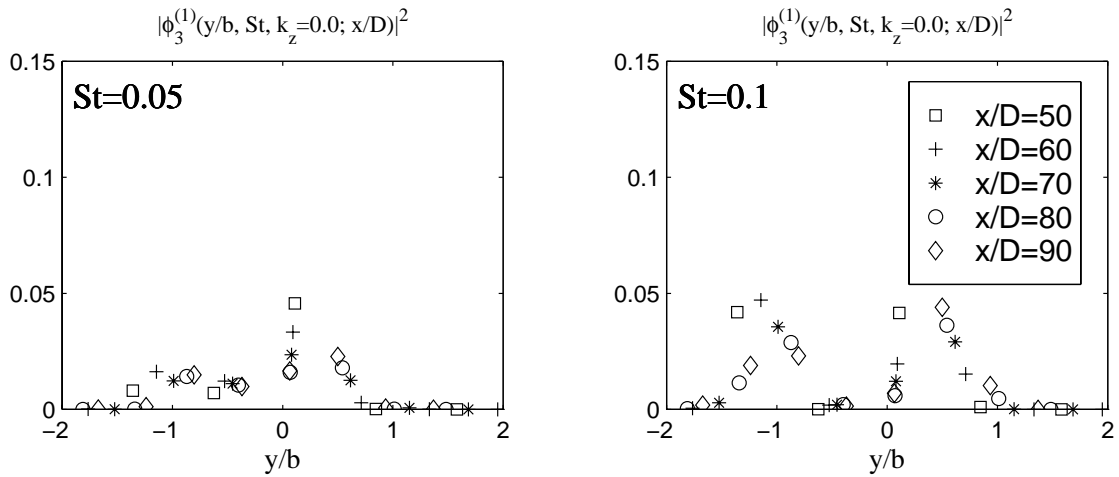
Figure 7.35: Scaled w-eigenmode $|\phi_3^{(1)}(y/b, St, k_z = 0; x/D)|^2$.

7.7 Three-rake results

7.7.1 Full set of POD modes

As noted earlier, the implementation of the POD presented in section 7.5.1 is based on the diagonal elements of the cross-spectral matrix $\Phi_{\alpha\alpha}$ and neglects information contained in the off-diagonal terms. This was done in order to examine the self-similarity of the POD modes without implementing a Taylor's frozen field approximation to find the Φ_{23} term required for the solution of (6.5). In order to reconstruct the POD modes in physical space, all components of the $\Phi_{\alpha\beta}$-matrix must be known. The term Φ_{32} can be obtained by a procedure described in Ukeiley and Glauser [142]. A Fourier transform of the continuity equation gives,

$$\frac{\partial \hat{u}_\alpha(y,z,f)}{\partial x_\alpha} = \frac{\partial \hat{u}_1(y,z,f)}{\partial x} + \frac{\partial \hat{u}_2(y,z,f)}{\partial y} + \frac{\partial \hat{u}_3(y,z,f)}{\partial z} = 0 \tag{7.8}$$

Since the spreading rate $db/dx \approx 0.1$ is small, the streamwise direction is weakly inhomogeneous and, as a first approximation, will be considered as homogeneous. We'll return to this assumption in chapter 8. According to Antonia et al[7], Thomas and Brehob [138], the structures in the self-similar region of the turbulent plane jet convect at approximately 60% of the local jet centerline velocity ($U_c \approx 0.6 U_{\max}$). First we form the complex conjugate of equation (7.8), multiply by $\hat{u}_2(y',z',f)$ and average over multiple ensembles. After performing a spatial Fourier transform in the z-direction and applying a constant group speed hypothesis in the x-direction,

$$\frac{\partial}{\partial x} = -\frac{1}{U_c}\frac{\partial}{\partial t} = -2\pi i f \frac{1}{U_c} = 2\pi i k_x, \tag{7.9}$$

the equation (7.8) can be rewritten in terms of $\Phi_{\alpha 2}$ (6.4) as in [142],

$$2\pi i k_x \Phi_{12} + \frac{\partial \Phi_{22}}{\partial y} + 2\pi i k_z \Phi_{32} = 0 \tag{7.10}$$

From the above relation, Φ_{32} can be easily calculated. The remaining terms Φ_{21}, Φ_{31} and Φ_{23} can be found using the property that the Φ-matrix is Hermitian,

$$\Phi_{\alpha\beta}(y,y',k_x,k_z) = \Phi^*_{\beta\alpha}(y',y,k_x,k_z) \tag{7.11}$$

This spectral correlation tensor $\Phi_{\alpha\beta}$ is a kernel in the integral equation (6.5) to find the POD modes for different streamwise and spanwise wavenumbers, k_x and k_z, respectively.

By exploiting certain symmetries of the $\Phi_{\alpha\beta}$ matrix which are discussed at length in section 6.1.3 and by application of a finite quadrature form of (6.18), the POD eigenfunctions $\varphi_\alpha^{(n)}(y_i;f,k_z)$ and associated eigenvalues $\lambda^{(n)}(f,k_z)$ were determined.

The resulting first POD eigenvalues $\lambda^{(1)}(St,k_z)$ are presented in Figure 7.36. In this implementation of the POD the eigenvalues are the same for all three velocity components. The eigenvalue distribution has a peak at $St = 0.09$, $k_z = 0$. Recall that the eigenvalues $\lambda_u^{(1)}$ and $\lambda_v^{(1)}$ obtained using (7.3) peak at $St = 0.05$ (Figure 7.19) and $St = 0.1$ (Figure 7.21), respectively. It is interesting to note that the peak Strouhal number for the planar mode compares quite well with the Strouhal number corresponding to the jet "flapping frequency" (7.2) reported in earlier studies of the planar jet. The planar component ($k_z = 0$) of the first POD mode is presented in Figure 7.37.**a)**. Note that since this is a planar mode, the w-component POD mode
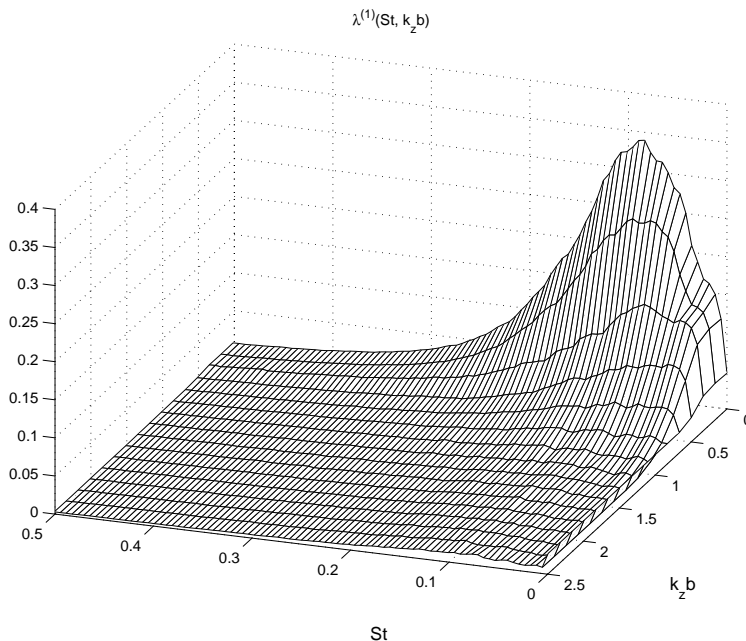
Figure 7.36: Combined eigenvalue distribution for the first POD mode $\lambda^{(1)}(St, k_z)$ at $x/D = 70$.

is nearly zero. Recall that the diagonal elements Φ_{11} and Φ_{22} are dominant with respect to Φ_{12}. Therefore, the POD modes obtained from the solution of (6.5) shown in figure 7.37.**a)** compare quite favorably with those shown in Figures 7.19 and 7.21 which result from the diagonal terms only (7.3).

Three non-planar parts of the first POD mode for $k_z b = 0.33, 0.5, 0.66$ are shown in Figure 7.37.**b)**, **c)** and **d)**, respectively. While the shape of the u-component for the non-planar mode is relatively similar to the u-component of the planar part, the v-component changes quite dramatically with increased k_z. Inspection of the first POD mode at different wavenumbers k_z, Figure 7.37, reveals that while the ($k_z b = 0.33$)-mode is still somewhat close in shape to the planar ($k_z = 0$) mode, the ($k_z b = 0.5$)-mode exhibits a qualitatively different behavior. The v-component shows two peaks in the y-direction and the amplitudes of v- and w-components are of the same order. The ($k_z b = 0.66$)-mode is quite similar to the ($k_z b = 0.5$)-mode, the only difference being a smaller amplitude. The v-mode amplitude decreases with k_z while the w-mode increases. For high wavenumbers, the amplitude of the w-component is comparable with the amplitude of the v-component.

Based upon the implementation of the POD as outlined above, it was found that the turbulent planar jet supports a planar structure aligned in the spanwise direction ($k_z = 0$) as well as an essentially three-dimensional structure with asymmetrical shape in the y-direction. Because of this "dual aspect" of the time averaged structure, both were chosen to restore the shapes of planar and non-planar coherent structure in physical space.

7.7.2 Choice of separation between rakes

As was already discussed in section 6.8.1, the three-rake experiment allows one to extract information about the planar ($k_z = 0$) and one non-planar ($k_z = 1/(2H)$) structure. By adjusting H, different non-planar structures can be extracted from the flow. So, the question

arises as to what particular wavenumber to choose. An eigenvalue spectrum for the first POD mode, Figure 7.36 shows a monotonous decay of energy in the k_z-direction, with peak value at $k_z = 0$. The eigenvalue distribution for the first POD mode is essentially zero for $k_z b > 1$. In order to avoid the spatial aliasing in the z-direction *to resolve the planar mode*, the restriction (6.29) gives a lower limit for the separation between rakes,

$$2k_z^{(N)}b = 2b/(2H) \geq 1, \quad \text{or} \quad H \geq b \tag{7.12}$$

If the condition (7.12) is satisfied, the planar mode will be resolved properly. But all non-planar modes with $0 < k_z < k_z^{(N)}$ will be contaminated by modes above the Nyquist wavenumber $k_z^{(N)} = 1(2H)$. So, the completely accurate measurement of any non-planar structure is impossible with the three-rake experiment. Still, some useful qualitative results can be extracted. It is noted first from Figure 7.37, that all the modes with $k_z b \geq 0.5$ appear to be from the same family. Second, the three-rake experiment works as a band-pass filter in the z-direction with fairly wide band (section 6.8.1) and all modes within this band around the chosen wavenumber will be present with some weights in the extracted mode. Consequently, not the exact shape, but only a qualitative topology of the non-planar structure can be reconstructed.

In addition to the planar mode, the non-planar $(k_z b = 0.5)$-mode was chosen to be reconstructed in the physical domain for the following reasons:

1. It satisfies the restriction (7.12).

2. It shows a distinctively different shape in $y - St$ space compared with the planar mode.

3. All components' amplitudes are essentially non-zero.

4. This mode is the most energetic among all modes, satisfying the restriction (7.12).

Based on the above criteria, the separation between rakes was chosen to be $H = b = 8.9$ cm. This arrangement provides the measurements of both the planar $(k_z = 0)$ mode and $(k_z b = 0.5)$-mode.

7.7.3 Planar mode $k_z = 0$

The three-rake experiment provides measurements of either (u, v) or (u, w) components of the velocity. Since the w-component of the planar part of the POD mode is nearly zero, as shown in Figure 7.37.**a)**, the instantaneous w-field is not necessary in order to restore the shape of the planar structure. Thus, only the (u, v)-instantaneous velocity field was used to restore first three planar (u, v)-POD modes in the physical space.

A plot of the instantaneous field and first two POD modes are plotted in Figure 7.38 as vector plots. Additional sequential time records are presented in Figures 7.39, 7.40 and 7.41. The temporal coordinate is converted to a pseudo-spatial coordinate and nondimensionalized by b, $x = U_c t/b$. Here U_c is a convective velocity of the structures, which was chosen to be $U_c = 0.6U_{\max}$. Also in the figure, the instantaneous velocity fluctuations u' and v' (black line) at $y/b = 0.4$ are compared to a reconstructed velocity based on sum of the first three POD modes (grey line). One can see, that the three modes do an admirable job in capturing large-scale

velocity variations. The deviation of the sum of the first three modes from the instantaneous velocity can be qualitatively characterized as,

$$\sigma_\alpha^2(y) = \langle [u_\alpha(y,t)_{instant} - \sum_{n=1}^{3} u_\alpha^{(n)}(y,t)]^2 \rangle \tag{7.13}$$

For instance, for $y/b = 0.4$ $\sigma_1 = 1.2$ m/sec. Again, it is consistent with the fact that first few POD modes cover most of the turbulent energy of the flow, as shown in Figure 7.25.

The first POD mode clearly reveals the existence of vortical structures. Clockwise rotating vortices are visible at $x = 1.5, 7, 10, 16, 18, 20.5$ and counterclockwise rotating vortices are present at $x = 5, 13, 17$. Vortices are centered along the line $y = 0$ and vary in size. It seems that the alignment along the jet centerline does not support the Karman vortex street hypothesis of earlier investigations. The intermittent appearance of vortices is also obvious. Analysis of longer time records has revealed that the vortices are more likely to exist in packets or trains of several alternately rotating vortices. One example of such train of structures is visible at $x = 13..19$.

The flow field corresponding to the second POD mode (Figure 7.38) is more complicated and less obvious for physical interpretation. Since this mode is energetically weaker that the first one, other non-planar modes might contaminate it, due to a coarse filter resolution in the z-direction.

7.7.4   Non-planar mode $(k_z b = 0.5)$

For a three-dimensional coherent structure, instantaneous measurements of all velocity components are necessary to reconstruct the non-planar POD mode in the physical space. Working only with either (u, v) or (u, w) components, an exact calculation of the phase-related coefficients $\mathbf{c}^{(n)}$'s (see section 6.7) cannot be performed. This lack of experimental measurements of simultaneous (u, v, w) introduces some ambiguity into the reconstruction procedure. One way to deal with this issue is to recognize what the u-component of the POD mode, shown in Figure 7.37.**c)** is dominant over v- and w-parts of the POD mode and will, consequently, provide the most information about the phase. Hence two reconstructions using the (u, v) or (u, w) instantaneous velocity field can be performed. This provides some information about either (u, v) or (u, w) parts of the coherent structure. Since both of them involve the u-component, one way to *qualitatively restore* the (u, v, w)-velocity field of the coherent structure is as follows. One can analyze the $u(y, x)$-field for both cases and look for similar patterns or *signatures* of structures. Matching the u-signatures gives the qualitative (u, v, w)-flow corresponding to the structure. In effect, the projections are used as the basis for conditional sampling of a characteristic u-signature.

The decomposition of the non-planar component of the instantaneous (u, v) velocity field for $k_z b = 0.5$ into a first non-planar POD modes is presented in Figure 7.42. Again, the first 3 POD modes represent reasonably well the large scale instantaneous u' and v' velocity fluctuations. Using (7.13), the deviation was found as $\sigma_1(y/b = 0.4) = 1.2$ m/sec. The first and second (u, v) POD modes are shown as well.

An example of results using the matching procedure described above is given in Figure 7.43. Figure 7.43.**b)** and Figure 7.43.**c)** show contours of the u-component for (u, v) and (u, w) parts of the structure. Since they look quite similar to some extent, the u-, v- and w-fields must

represent the same kind of structure. All three velocity components are essentially non-zero. The structure can be divided into three regions. They are displayed as square boxes in (u, v)- and w-plots in Figure 7.43.**a**). The 'head' of the structure is located at $x = 36..37$, $y/b < 0.5$ and is characterized by a local (u, v) velocity field (Figure 7.43.**a**) with essentially no w-component (Figure 7.43.**d**). The 'wings' of the structures lie in regions $|y/b| > 0.5$. Within the 'wings' exist extended regions of non-zero w-component. The signs of w-component are different at opposite 'wings'. The 'tail' of the structure ($x = 39..41$) consists of series of upward or downward motion, with the (u, v)-flow similar to 'head''s flow, but in opposite direction. Small vortical motions in the (u, v)-plane are visible at the centerline at $x = 38.7$ and $x = 40.5$. They seem to roughly coincide with the locations of non-zero w-flow. The sketch of the possible streamline topology is given in the Figure 7.44. The top view summarizes the flow field topology, described before. The prospective view gives a spanwise unfolding of the structure. The back view reveals the flow topology similar to streamwise vortices aligned in spanwise direction. The location of the vortex centers is approximately at $y/b = 0.5..1$. This seems to support Mumford's hypothesis [114] regarding the existence of streamwise vortices aligned along the maximum shear stress. The spanwise size of the structure is in the order of b, $L_z \sim 1/k_z = 10..20$. So, structures with different L_z, similar to sketched structure in Figure 7.44, exist in the jet. Based on the analysis of the long time records, no apparent correlation between locations of planar spanwise structure and locations of the non-planar spanwise-periodic structure was found. The possible modes of energy exchange between the structures are not known at this time. More rakes of the probes or/and conditional sampling techniques, based on the preliminary information about non-planar POD mode are required to investigate the flow topology of the non-planar structure in sufficient detail to give the answer to the above question.

The streamlines at the 'wings' of the structures are inclined relative to the centerline of the jet. If we define the structure as the event where the u-component exceeds a certain threshold $u_{\min}$, the mean slope of the structures can be defined from conditional sampling,

$$\theta = \left\langle \tan^{-1}(v/u) \mid u > u_{\min} \right\rangle \tag{7.14}$$

The calculation over large number of events gives the constant value of the slope as $\theta = 0.3..0.4$ rad $= 17..22$ degrees, independent from u_{min} for 1.5 m/sec $< u_{min} < 3$ m/sec. Thus, the angle between the streamlines and the centerline is approximately constant inside the tales. It is not clear at this point why the streamlines behave in such fashion. Refined measurements and/or numerical modeling are needed to address this issue.

The physical interpretation of the second mode is obscure, probably for the same contamination reasons, briefly discussed in the previous section.

7.7.5 Comparison of Fourier- and wavelet-based reconstructions

Instead of the wavelet transform, one can use a Fourier transform as a basis to reconstruct POD modes in the reconstruction algorithm described in Section 6.7. This implementation is straightforward and won't be discussed here. Such an approach was used to reconstruct dynamical behavior of vortical structures in the near field of a round jet in [37].

In this study, the Fourier-based reconstruction was applied to reconstruct planar modes and the results are plotted in Figure 7.45. The wavelet reconstruction of the same flow is given in Figure 7.38. Comparison of instantaneous u' and v' velocity traces at $y/b = 0.4$

resulting from a sum of the first three POD modes reveals that the Fourier reconstruction misses some important large-scale fluctuations. The vortical structures are still visible in the first POD modes, although they are less pronounced. The second mode velocity field also differs from the wavelet reconstructed second mode. Applying (7.13), the deviation was found to be $\sigma_1(y/b = 0.4) = 1.27$ m/sec, which is greater than the deviation $\sigma_1(y/b = 0.4) = 1.22$ m/sec for the wavelet reconstruction case.

The better job of the wavelet reconstruction stems from the fact that, due to the local nature of the wavelet basis functions, any errors in reconstruction remain *local* and do not affect the entire time domain. On the contrary, the Fourier transform operates with infinitely spanned basis functions and any local error will spread out throughout the temporal region. In the limit of increasing the sampling frequency and the number of points in time the Fourier and wavelet reconstruction will coincide, but for finite resolution and limited information in time, which is a common case in experimental measurements, the wavelet reconstruction is preferred against the Fourier reconstruction.
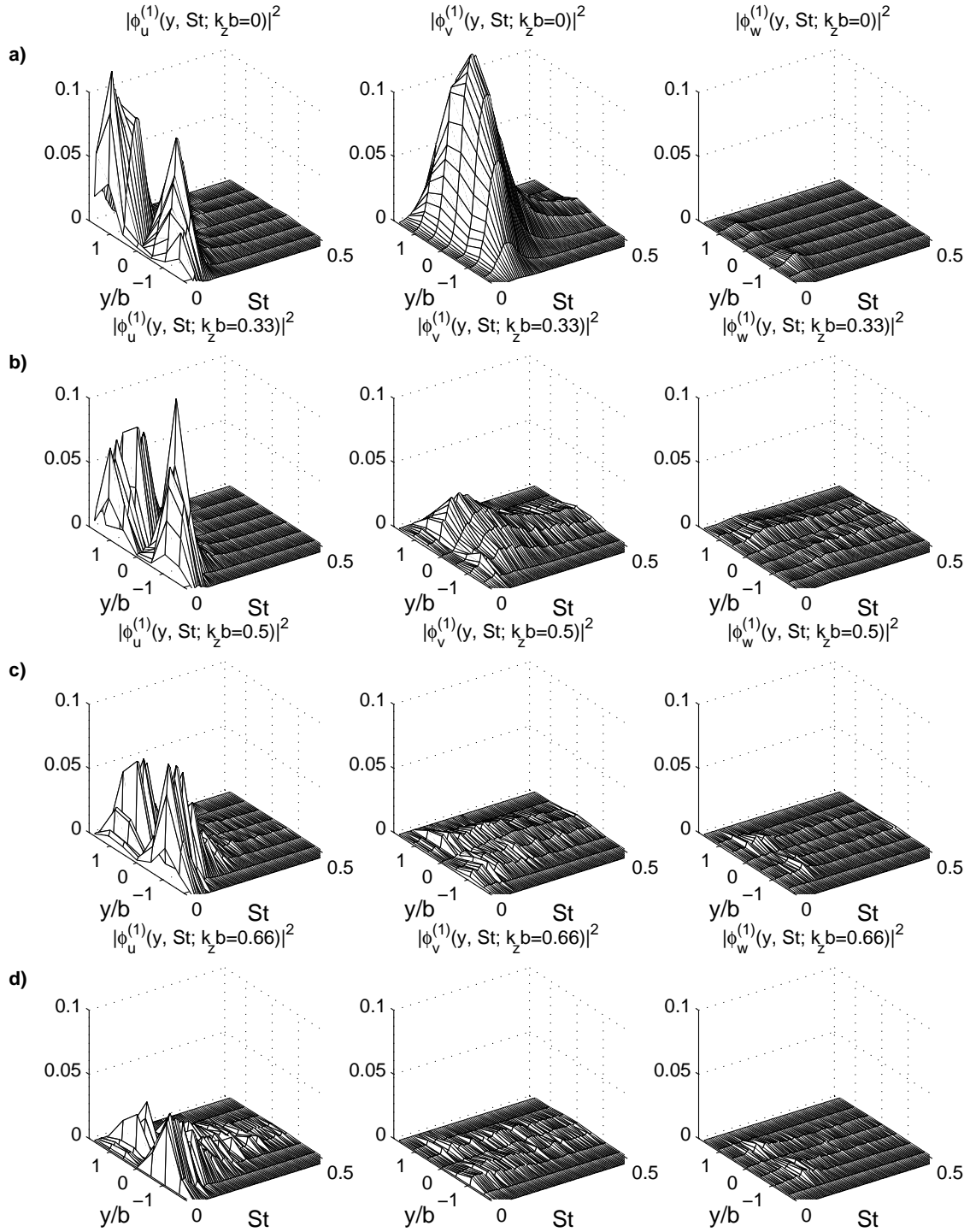
Figure 7.37: Modulus squared of the α-components of the first POD mode $|\phi_\alpha^{(1)}(y, St, k_z)|^2$ for $k_z b = 0, 0.33, 0.5, 0.66$ at $x/D = 70$.
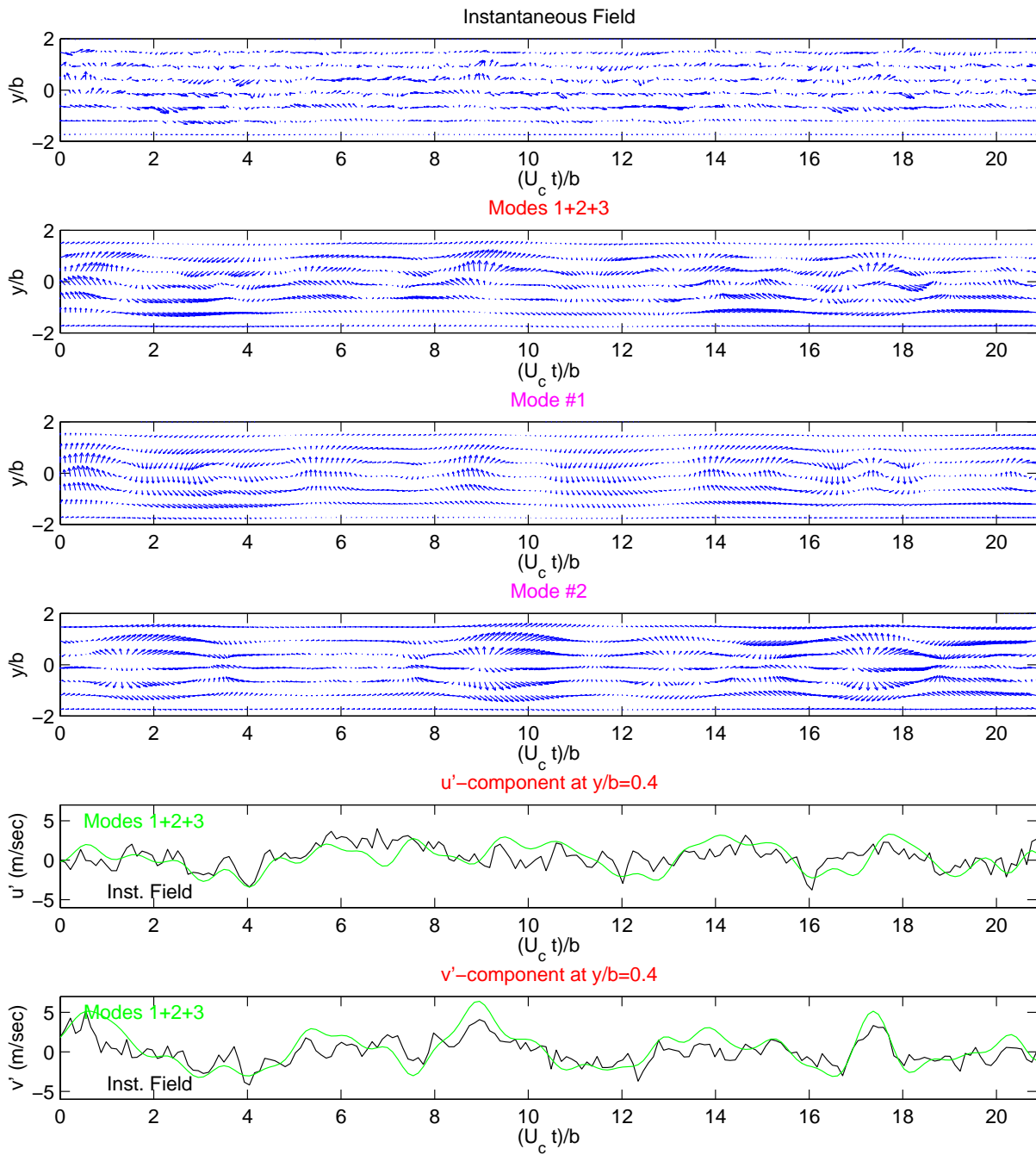
Figure 7.38: Planar (u, v) mode: Instantaneous velocity field, reconstruction with first three POD modes, the first and second POD modes and the comparison of the instantaneous velocity and three-mode reconstruction at $y/b = 0.4$, $0 < U_c t/b < 21$
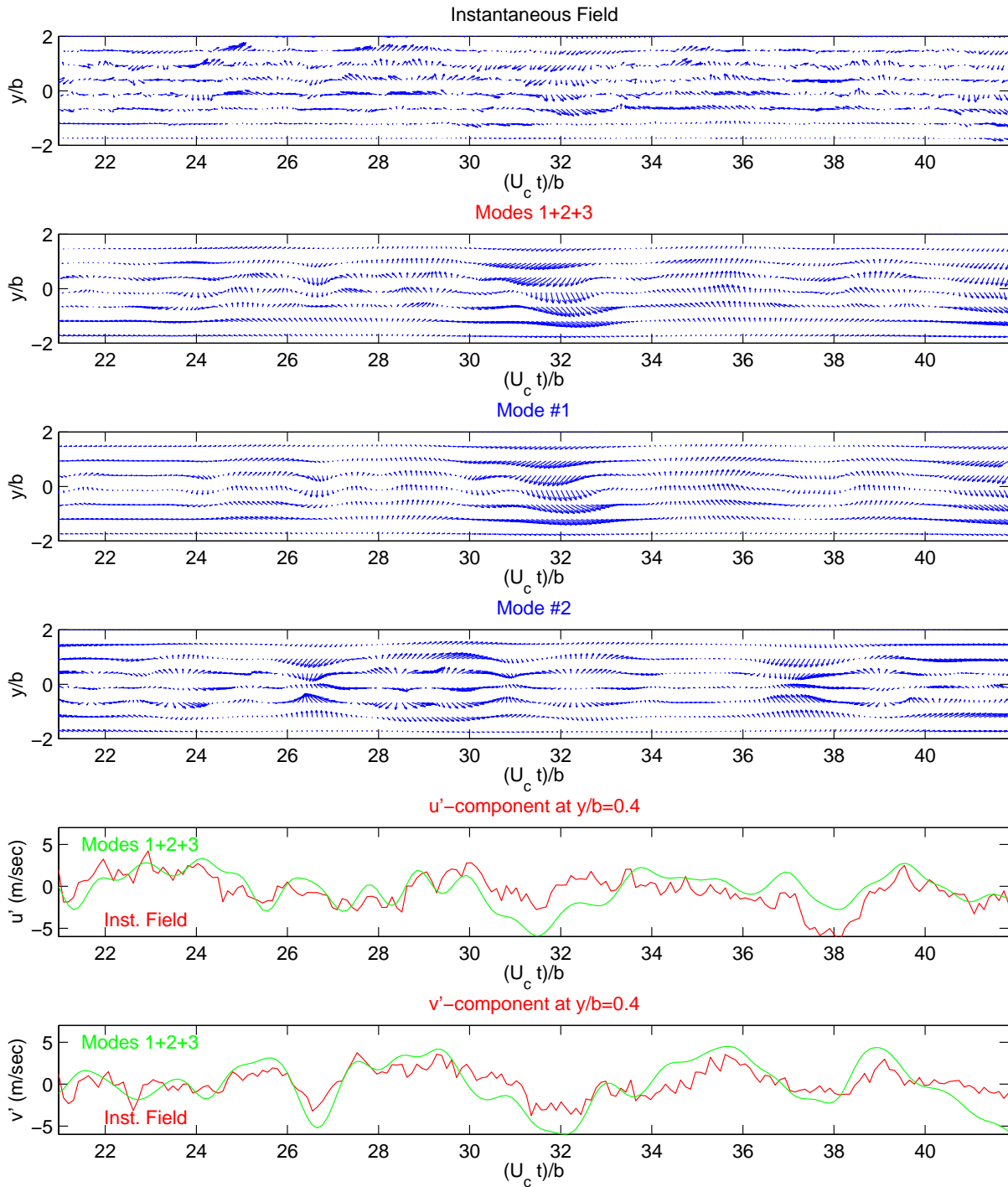
Figure 7.39: Planar (u, v) mode: Instantaneous velocity field, reconstruction with first three POD modes, the first and second POD modes and the comparison of the instantaneous velocity and three-mode reconstruction at $y/b = 0.4$, $21 < U_c t/b < 42$
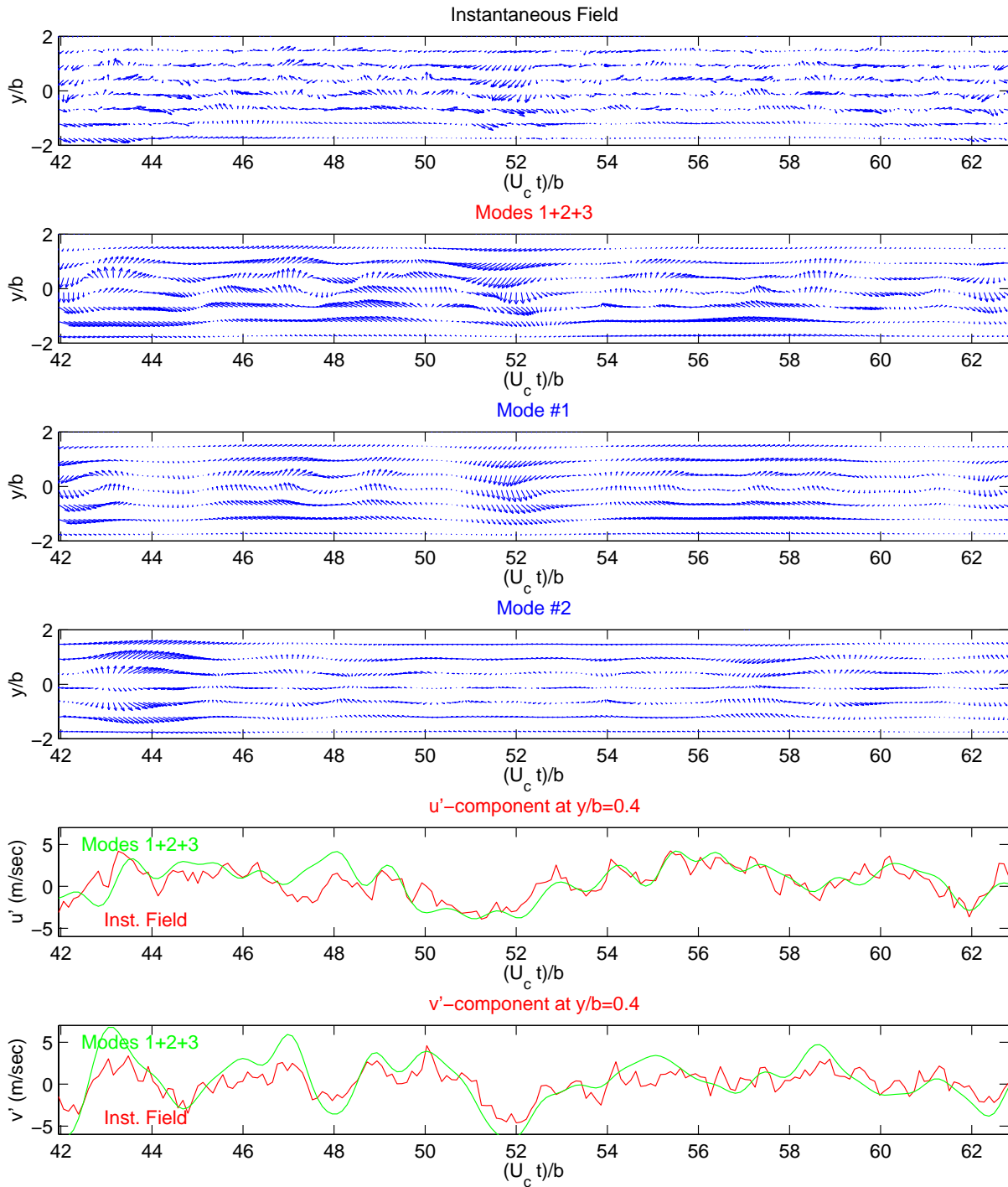
Figure 7.40: Planar (u, v) mode: Instantaneous velocity field, reconstruction with first three POD modes, the first and second POD modes and the comparison of the instantaneous velocity and three-mode reconstruction at $y/b = 0.4$, $42 < U_c t/b < 63$
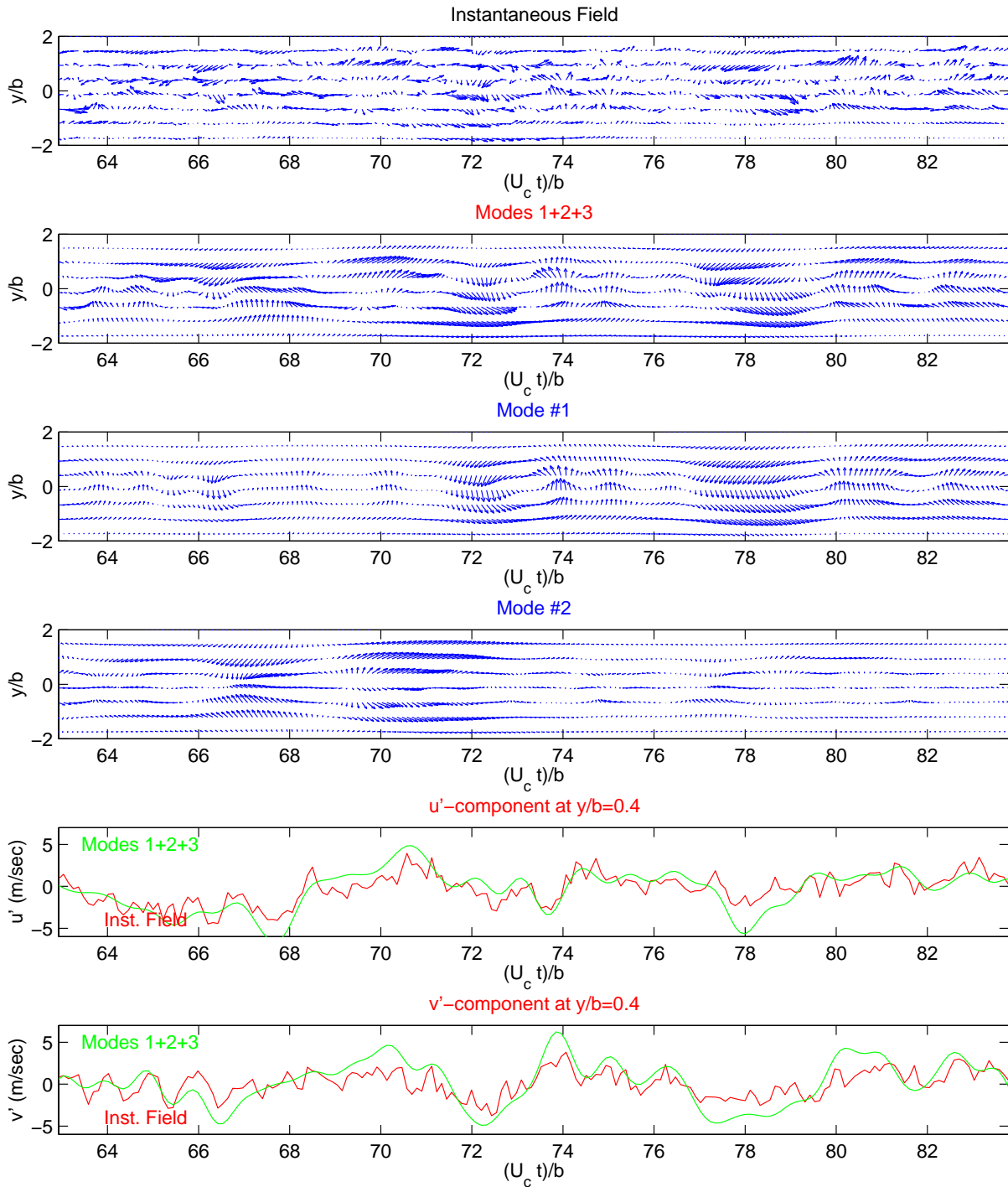
Figure 7.41: Planar (u, v) mode: Instantaneous velocity field, reconstruction with first three POD modes, the first and second POD modes and the comparison of the instantaneous velocity and three-mode reconstruction at $y/b = 0.4$, $63 < U_c t/b < 84$
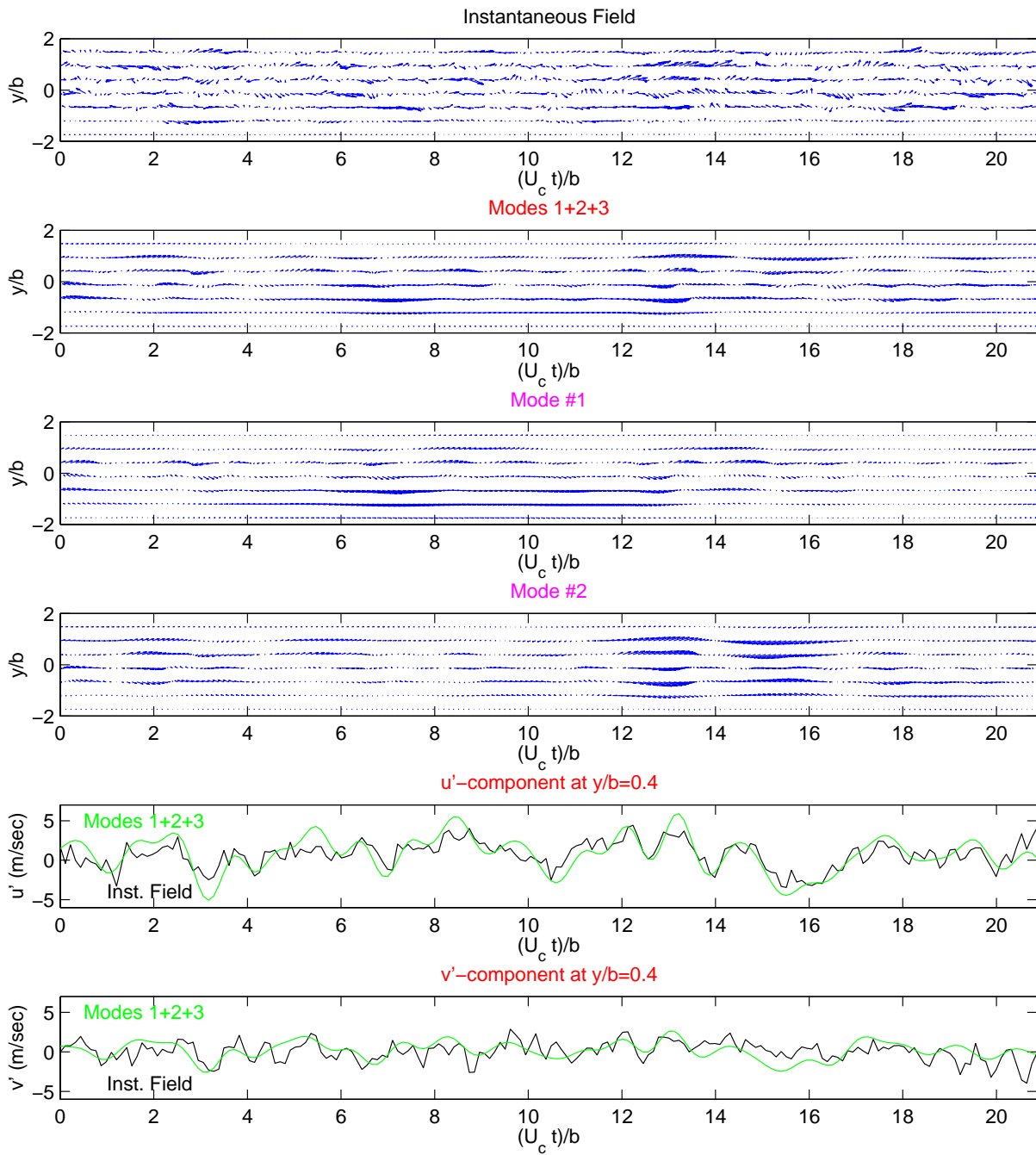
Figure 7.42: Non-planar $k_z b = 0.5$ (u, v) mode: Instantaneous velocity field, reconstruction with first three POD modes, the first and second POD modes and the comparison of the instantaneous velocity and three-mode reconstruction at $y/b = 0.4$
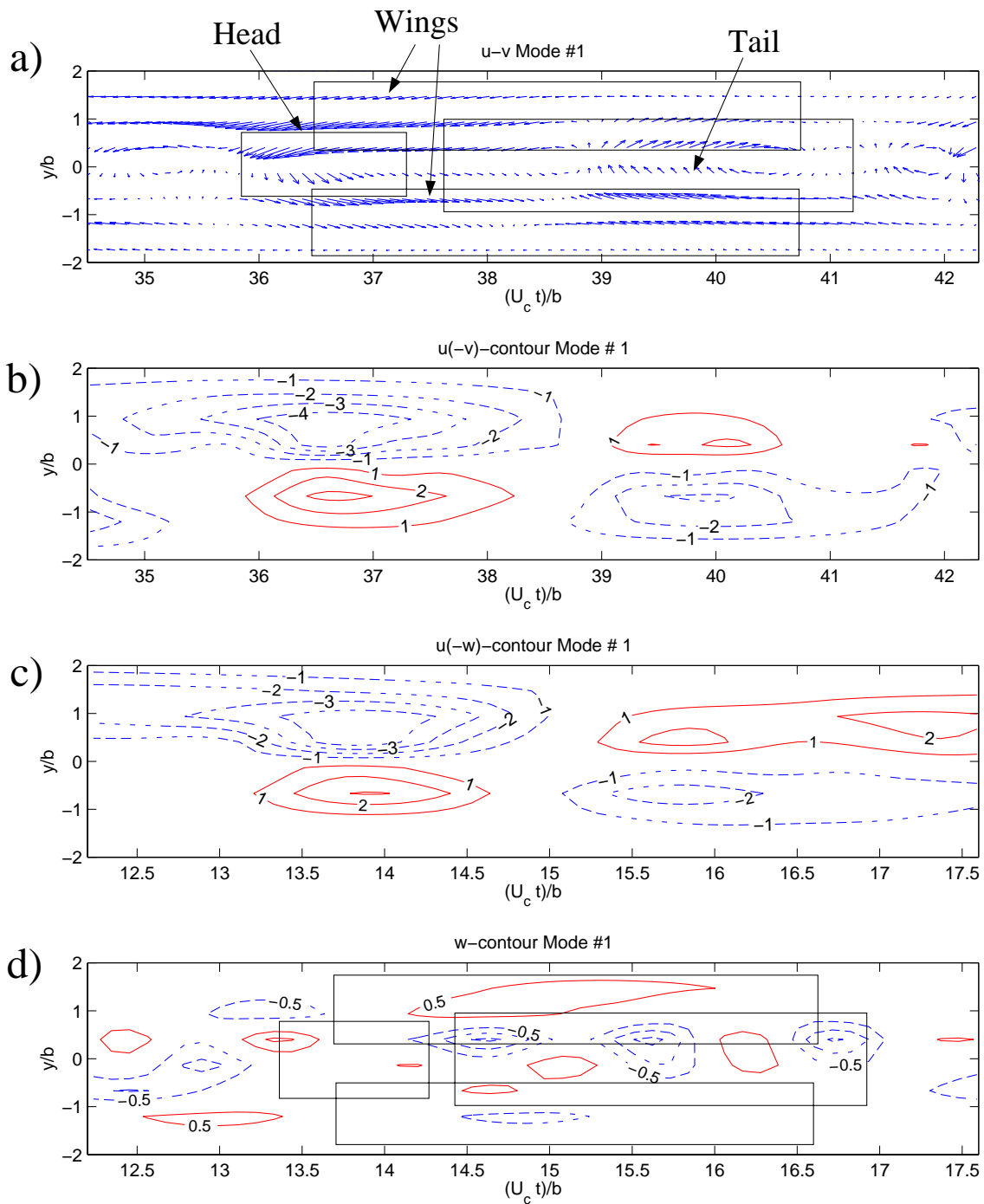
Figure 7.43: Non-planar $k_z b = 0.5$ structure: (u, v) field, $u(-v)$-, $u(-w)$-, and w-velocity fields.

Top View

Streamlines

Nonzero w-flow

Centerline

y

x

Prospective View

z

H

y

x

Back View

H

z   Centerline

y
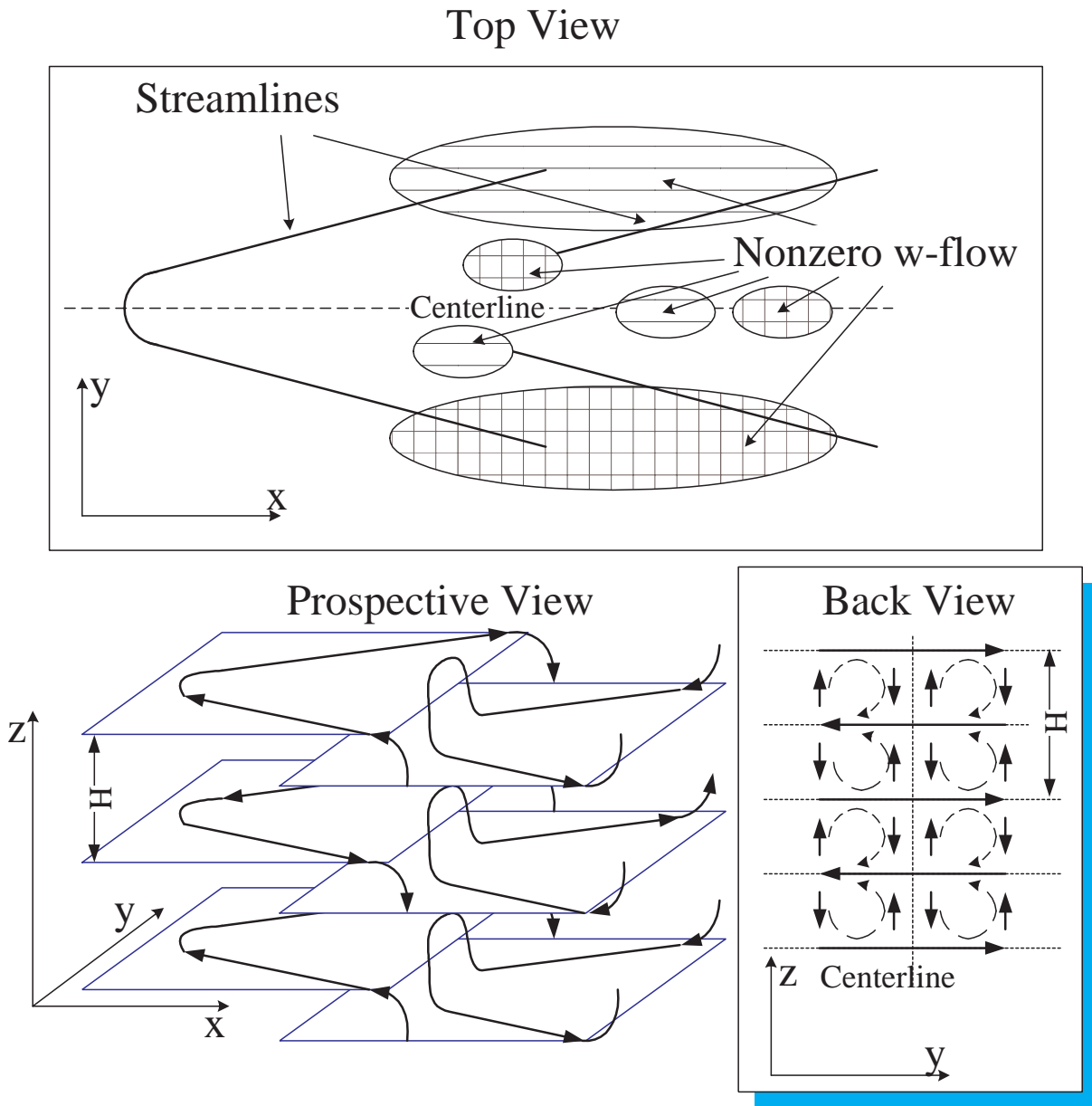
Figure 7.44: Sketch of non-planar $k_z b = 0.5$ structure: Top, Prospective and Back views.
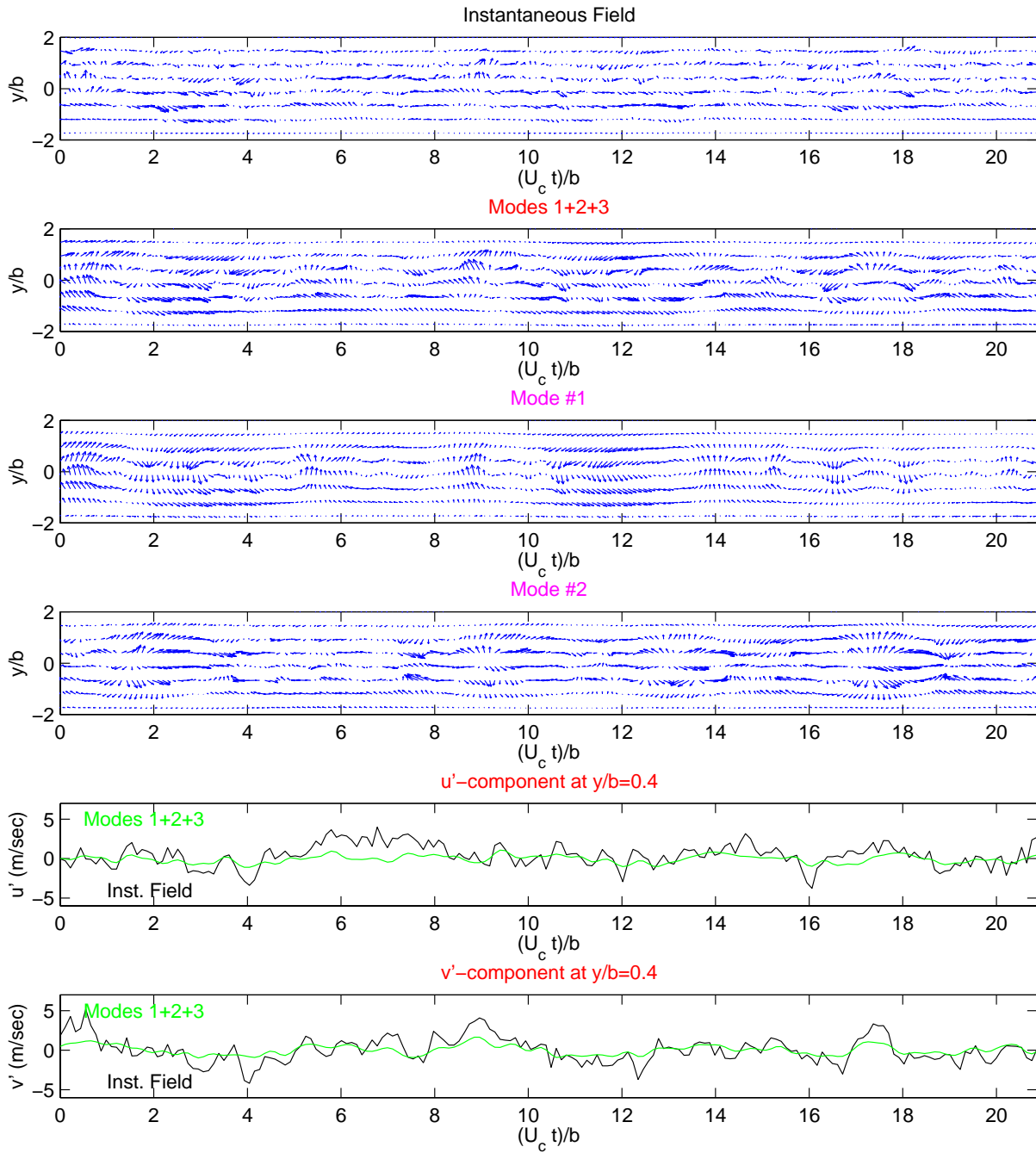
Figure 7.45: Fourier reconstruction of planar (u, v) mode, using the same flow field as in Figure 7.38.

Chapter 8

CONCLUSIONS AND FUTURE WORK

8.1   Conclusions

Experimental investigation of the coherent structure in the self-similar region of the planar turbulent jet is performed by applying the Proper Orthogonal Decomposition (POD) in conjunction with the continuous wavelet transform. Detailed measurements of the spectral cross-correlation matrix $\Phi_{\alpha\beta}(y, y', f, k_z)$ are obtained at several streamwise locations using two spanwise separated x-wire rakes. The obtained matrix is used as an input to compute the POD eigenmodes $\varphi_\alpha(y, f, k_z)$ in the jet. An eigenvalue convergence analysis shows that the first 4 modes account for approximately 90% of the turbulent energy. In addition, the POD modes are found to behave in a self-similar fashion when scaled by the local half-width and the local maximum velocity. This is a sufficient condition for the self-similarity of the coherent structure dynamics in the planar turbulent jet.

The results from the two-rake experiment indicate that the self-similar large-scale structure in the planar jet is three-dimensional in nature. However, it is natural given the geometry of the flow field, to question whether some portion of this underlying structure can be approximated as planar. From the results presented here the answer seems to be yes. The results suggest that the flow supports a planar structure aligned in the spanwise direction ($k_z = 0$) as well as an essentially three-dimensional structure with asymmetrical shape in the y-direction and pseudo-periodically distributed in the spanwise direction. In particular, modal eigenvalue distributions in k_z, St space indicate that a substantial fraction of the energy associated with the u-component POD modes and nearly all the energy associated with the v-component POD modes are due to an essentially planar component of the large-scale structure that extends in the spanwise direction. That is, most of the u and v-component energy is associated with $k_z = 0$ and falls off quite rapidly for $k_z > 0$. The eigenvalues also exhibit a well defined peak in St with tails extending to somewhat higher values of St. This suggests that the planar structure is quasi-periodic and may also exhibit an intermittent behavior. This planar structure is reminiscent of the "spanwise roller" structures noted by Mumford [114] using a pattern recognition method. Measurements of Φ_{12} indicate that large-scale Reynolds stress $\overline{u'v'}$ is governed largely by this planar component of the flow structure.

In order to investigate the topology and dynamics of the structures in the physical domain, phase related temporal coefficients are needed. A novel wavelet reconstruction procedure is used to project the POD modes onto instantaneous flow field realizations, which allows one to calculate these coefficients. The wavelet based reconstruction technique is shown to perform better for finite time records than a more conventional Fourier-based reconstruction technique. The topology of the most energetic extracted structures is investigated in detail. Two types of structures are found: The first involves planar spanwise vortical structures. These tend to cluster in packs of several vortices with alternating rotations. The second is a more complex structure, asymmetric in the cross-stream direction and pseudo-periodic in the spanwise direction. These are topologically similar to an array of streamwise vortices. Thus, the measurements support the scenario of two topologically distinct structures co-existing in the planar jet. This is in general agreement with the topology proposed by Mumford [114], using a pattern recognition technique. The new information about the coherent structures in the jet provided by this study will help our understanding of the dynamics of the jet. Since some important question about origin, interaction and evolution of the structures are still to be answered. The results of the present research can be used to define suitable criteria for a variety of conditional techniques that can be used to address these issues.

8.2   Prospective for Future Work

Since the POD modes provide a complete set of functions which exhibit optimum convergence they can be used to build a low-dimensional model of the planar jet. The approach outlined below is similar to that taken in recent investigations of the dynamics of the boundary layer [15] and the planar turbulent shear layer [142].

8.2.1   Streamwise Direction

The inability to perform direct measurements of the velocity cross-correlation matrix for cases involving streamwise probe separations due to probe wake interference makes analysis of the streamwise coordinate problematic. Since in the self-similar region the spreading rate of the jet $db/dx \approx 0.1$, almost all the existing approaches to investigate jet dynamics are based on the assumption that the flow in homogeneous in streamwise direction. Using the Taylor's hypothesis, the streamwise evolution is then analyzed through the temporal evolution, with the latter one much easier to get experimentally. Physically this is equivalent to imposing wall-like boundary conditions which prevent the jet from spreading. One then expects that the new modified system is locally dynamically similar to the original system. Using this approach is clearly inappropriate for addressing issues related to global dynamics, though. Another approach is to recall that the dynamics of the jet in this region has been proven to be self-similar. Thus, the governing equations can be rewritten in self-similar coordinates and the streamwise direction will become a homogeneous one. Unfortunately, the time is this case will thus become an inhomogeneous coordinate. So there is no clear advantage of one approach against another.

8.2.2 Dynamical Modeling of the Jet

After the spatial orthogonal modes are extracted, the velocity can be decomposed in the series,

$$u_\alpha(x,y,z,t) = \sum_n \sum_{k_x} \sum_{k_z} c_\alpha^{(n)}(t; k_x, k_z) e^{2\pi i k_x x} e^{2\pi i k_z z} \phi_\alpha^{(n)}(y; k_x, k_z) \tag{8.1}$$

This series will be truncated to keep the minimal number of the most energetic modes. Symbolically this can be written as

$$\mathbf{u}(\mathbf{x}, t) \approx \mathbf{u}^N = \sum_n^N c_n(t) \varphi^{(n)}(\mathbf{x}) + \text{smaller scale modes} \tag{8.2}$$

The rest of the modes are considered as a dissipative influence on the large scales. The number of modes kept in the truncation can be varied to investigate the effect of neglected modes. We would like to keep as few modes as possible, but don't want to lose essential physics because of the truncation of dynamically significant modes. The Galerkin procedure will be performed to get a system of equations for the c's. The governing Navier-Stokes equations are symbolically written as

$$NS(\mathbf{u}) = \frac{\partial \mathbf{u}}{\partial t} + L(\mathbf{u}) + Q(\mathbf{u}, \mathbf{u}) = 0, \tag{8.3}$$

where L and Q are linear and quadratic operators, respectively. For explicit expressions of these operators, see [142], for instance. We would like to minimize the error after truncating the series (8.2) by orthogonalizing the N-S equations with the truncated velocity series to the orthogonal basis,

$$(NS(\mathbf{u}^N) \cdot \varphi^{(n)}) = 0 \tag{8.4}$$

In terms of temporal coefficients, the system (8.4) becomes a finite set of ODE's,

$$\frac{dc_n}{dt} = Bc_n + NL(c_n) \tag{8.5}$$

where B is a matrix and NL is a nonlinear matrix operator on c_n.

There still exists an energy transfer from large resolved modes to small unresolved dissipative scales. This interaction can be parametrically described by any simple model, like a Heisenberg spectral model for isotropic turbulence [15]. This model expresses the Reynolds stress of unresolved modes in terms of the strain rate of the resolved modes and is similar to sub-grid scale modeling in the numerical large-eddy simulation approach. The model introduces a parameter γ into the system (8.5) regulating the energy transfer from the large resolved modes to small unresolved ones. Since the exact mechanism of how the energy of the large modes dissipates is not likely to be important (see section 8.2.3), this simple parametric model is widely used to describe the dissipative influence of the small modes. Now we have two parameters to play with: the number of resolved modes N and the Heisenberg parameter γ in order to 'tune-up' our truncated system behavior (8.5) as close as possible to the real one. Also the system (8.5) can be analyzed by means of the theory of dynamical systems to investigate the dynamics of the system.

8.2.3 Viscous Effects

Rigorously speaking, the dynamical model is based on experimental data obtained at one Reynold number, namely $Re = 28,000$. While the set of basis POD functions is still complete, it could become non-optimal for flows with different Re. This could narrow the applicability of the model. But the viscosity effects appear mostly on small scales. Investigations of large-scale structures in different turbulent flows indicate that the shapes of these structures are macroscale-dependent and are primarily a function of the boundary and initial conditions. For the coherent structure, reported in this thesis, the characteristic Reynold number can be computed from the typical rms velocity U^* and the size L of the structure, $Re = U^*L/\nu$. For the planar structure at $x/D = 70$, $Re^{planar} = 5000$. So, the coherent structure is mostly governed by inertia forces, rather than viscous ones. Since the model deals with the first few energetic modes and the rest of the modes are modeled by a dissipative term, the viscosity will not likely change the spatial shape of first few POD modes. Rather, it will mostly effect the values of the tuning parameters in the model (like number of involved modes and the dissipation energy rate from the large-scale modes). Hence it is expected that the set of POD modes will still be close to the optimal set and the application of the model can be relatively easily extended for a range of planar turbulent jets with different Re-numbers.

8.2.4 Checking the Theory

Since we extracted the temporal-spatial behavior of the most energetic structures in the jet, this valuable information provides a rigorous check of the validity of the model predictions. If the system is reasonably small and can be studied analytically or numerically, comparison of the predicted dynamics with the results of the wavelet reconstruction analysis will help in tuning the model and in verifying all the assumptions made while building the model. The wavelet analysis is a very necessary component of this process.

8.2.5 Will the Model Work ?

The dynamical model is heavily based on the experimental data. The number of equations in the model depends on how fast the POD series converges. We need to have a minimum of three modes to model a nonlinear interaction between modes, so the minimum number is $3 \times 2 = 6$ (the factor of two comes from the fact that the temporal coefficients are complex). For more realistic modeling more modes (5..10 modes) should be included. So we potentially face a model with up to 20 equations. Analysis of such system can be quite complicated. In the worst scenario, it would be impossible to analyze the model. The wavelet reconstruction analysis of the experimental data in this case will be the only way to investigate the dynamics of the jet directly. The results of such analysis can help building alternative dynamical models.

Appendix A

LITERATURE REVIEW ON POD AND WAVELET TRANSFORM

A.1 Historical background on POD

Historically, the Proper Orthogonal Decomposition was proposed by Lumley, 1967, [101]. But the method itself is known under a variety of names in different fields: Karhunen-Loève procedure, (Karhunen, 1946, [86]; Loève, 1955, [99]), Principal Component or Hotelling Analysis (Hotelling, 1953, [78]), Empirical Component Analysis (Lorenz, 1956, [100]), Quasiharmonic Modes (Brooks el at., 1988, [31]), Singular Value Decomposition (Golub and Van Loan, 1983, [62]), Empirical Eigenfunction Decomposition (Sirovich, 1987, [129]) and others. Closely related to this technique is *factor analysis*, which is used in psychology and economics (Harman, 1960, [74]).

From the mathematical point of view the POD (3.2) is just a transformation which diagonalizes a given matrix R and brings it to a canonical form $\mathbf{R} = \mathbf{ULV}$, where $\mathbf{L}$ is a diagonal matrix. Therefore the roots of the KL expansion actually go into the middle of the last century. The mathematical content of KL procedure is therefore classical and is contained in the paper by Schmidt [126], which dates to 1907. A complete review of the early history of KL expansion can be found in [133].

A.2 POD: Application to turbulent flows

POD extracts a complete set of orthogonal modes by maximizing the energy of the modes. Any member of statistical ensemble can be expanded on this set, and this series converges as fast as possible. Also POD gives the eigenvalues, which correspond to the kinetic energy of each mode. The requirements of large data storage and automated computer controlled experiments to obtain detailed second-order statistics from the flow delayed the wide application of POD until the last decade of the century.

A.2.1 Turbulent boundary layers

The first attempts to apply the POD to turbulent flow occurred in boundary layers. One of the reasons to look at the boundary layer was the existence of a strong peak in production

of turbulent energy on the outer edge of the viscous sublayer. Kline et al. [90] were first to observe streamwise vortex pairs in the boundary layer near the wall and bursting events associated with them. Bakewell et al. [17] using experimentally obtained 2-point correlation matrix, have sketched dominant structures within the wall region. These consisted of randomly distributed counter-rotating eddy pairs elongated in streamwise direction. They showed that the sublayer and the adjacent wall region play an active role in the generation and preservation of a turbulent shear flow. The nonlinear mechanism of vortex stretching suggests that linearized theories cannot provide an adequate description of the viscous sublayer. Later these structures were identified with burst-like events in the boundary layer. Cantwell [35] provided a detailed discussion of the research of turbulent boundary layer. Aubry et al [15] successfully utilized the experimental POD eigenfunctions of Herzog [75] to create a dynamical systems model of the near-wall region of a turbulent boundary layer. By truncation of the series a low-dimensional system was obtained from the Navier-Stokes equation via Galerkin procedure. This model represented the dynamical behavior of the rolls and was analyzed by methods of dynamical systems theory. The model captured major aspects of the ejection and bursting events associated with streamwise vortex pairs. This paper appeared to be one of the first to provide a reasonably coherent link between low-dimensional chaotic dynamics and realistic turbulent open flow system. Spatio-temporal three-dimensional structures in a numerically simulated transitional boundary layer were examined by Rempfer & Fasel [122] using the POD technique. Λ-shaped vortices were found to be the most energetic modes in the flow. They correspond to physically observed structures and resemble bursting events in fully turbulent boundary layers. It was argued that the POD modes correspond to physically existing structures, when most of the energy is contained in the first mode.

Because of the experimental difficulties in obtaining second-order statistics from the flow, the POD technique has been applied to a number of *computational simulation* results. Moin & Moser [109] made direct numerical simulations of N-S equations in a turbulent channel for 128 x 128 x 128 grid points and Re=3200. The shot-noise expansion proposed by Lumley [103] was used to find the spatial shape of the coherent structure (CS). A dominant eddy was found responsible for 76% of the turbulent kinetic energy. Similar computational research was done by Ball et al. [18] for 24 x 32 x 12 grid points, Re=1500. A "snapshot technique" [129] was applied in order to extract the modes. The eigenfunctions were found as rolls (the most energetic mode) and shearing motions. The first 10 modes captured 50% of the turbulent energy. Rolls provide the mechanism for the transport in channel flows like turbulent 'bursts', while shearing modes were suggested to relate to the instabilities in the flow.

Sirovich & Park [131], Howes et al [79] performed numerical simulations of *Rayleigh-Benard convection* in a finite box for 17 x 17 x 17 grid points. POD technique, snapshot method and group symmetry considerations were applied to investigate CS. Ten classes of eigenfunctions were discovered. The first eigenmode being captured 60% of the energy. Numerically simulated flow in a square duct ($Re = 4800$, grid 767 x 127 x 127) was analyzed by POD in [56]. Two different structures were found. Near the wall this consists of a pair of high and low-speed streaks with the first POD mode seizing 28% of energy. In the corner domain a vortex pair with common flow toward the corner with 43% of the total energy was discovered. It was found that the energy in this region goes from the turbulence back to the mean flow. The flow in duct was found to have a greater degree of organization.

A.2.2 Turbulent jets and shear flows

Payne & Lumley [118] used experimentally obtained 2-point diagonal correlation tensor to extract CS in the turbulent wake behind a circular cylinder. Glauser et al. [57] investigated a large-scale vortex ring-like structure in the mixing layer in axisymmetric jet ($Re \approx 110,000$) at $x/D = 3$ by POD and shot-noise decomposition. The first 3 modes were found to contain almost all the fluctuation energy of the flow. Kirby et al. [88] used a snapshot method for 2-dimensional large-eddy simulation of an axisymmetric compressible jet flow on 240 x 80 point grid for $Re \sim O(10^4)$. They found the first 10 modes hold 94% of the total fluctuation energy. A similar approach was used by Kirby et al. [89] to investigate a simulated supersonic shear flow. Sirovich et al. [130] applied POD to the analysis of digitally imaged 2-dimensional gas concentration fields from the transitional region of axisymmetric jet. Here POD was proposed basically as a methodology for analyzing and treating a large body of experimental and numerical data. Ishikawa et al [83] applied POD and wavelet technique to investigate coherent structures in a turbulent mixing layer. POD procedure revealed the first mode to be the most energetic one, while wavelet transform found low-frequency modulation of vorticity in this mode. Hilberg et al [76] investigated large-scale structures existed in a mixing layer in a narrow channel using a rake of probes. They applied both classical and snapshot POD techniques and were able to identify the largest 2-dimensional mode. Snapshot POD for a conditionally averaged velocity field showed that first two modes contain the largest portion of coherent vorticity. Delville [44] also applied POD to the plane turbulent shear layer. Two rakes of hot-wire probes were used to extract the required correlation matrix from the flow. Vectorial version of the POD was found to give a better presentation of structures in the flow. Different aspects and problems of applying the POD procedure were also discussed. An axisymmetric jet was investigated in [13]. POD modes for near-field pressure in the inhomogeneous streamwise direction were obtained for the first time and observed as growing, saturating and decaying waves. The phase velocity for the first few modes near saturation point were found to be the same $U_p = 0.58U_j$. A characteristic structure was reconstructed using the shot-noise decomposition. It was observed that vortex pairings do not happen periodically and vortex tripling events occur quite often. Citriniti [37] applied POD to an axisymmetric mixing layer in a fully turbulent ($Re = 80,000$) axisymmetric jet. An array of 138 hot wires were used to obtain the correlation data. POD modes were projected onto instantaneous realization of the velocity field at $x/D = 3$ and the temporal coefficients of the corresponding POD modes were investigated. Kopp et al [92] investigated large-scale structure in far field of a wake behind a cylinder ($x/d = 420$, $Re = 1200$). They used a rake of 8 x-wire probes to get the instantaneous velocity field in both cross-stream and spanwise directions. They applied the POD technique to extract the first modes and used the first two as a template for a Pattern Recognition (PR) technique. The structures found via PR and POD were similar and represented negative u-fluctuations with outward v-fluctuation in the cross-stream direction. In the spanwise direction a double roller structure was discovered. A flow field in lobed mixer (mixing enhancement device) was considered by Ukeiley et al [141]. A rake of the probes in the streamwise direction was used to collect data on the correlation matrix. The first POD modes were projected back to instantaneous flow field to get information about multifractal nature of the flow.

A.2.3 POD-based modeling

The optimal mean square convergence of POD modes make them useful as a basis for constructing low-order dynamical models for different applications. Using a truncated number of the POD modes as a basis and projecting them onto the Navier-Stokes equations allows one to reduce the governing PDE to a low-order system of ODE's. The rest of modes are modeled by a dissipative term. Analysis of the obtained system can shed light into the dynamics of the system. Aubry et al. [15] were able to model a turbulent boundary layer by such an approach. The model captured major aspects of the ejection and bursting events associated with streamwise vortex pairs. Aling et al [5] proposed a POD-based technique to construct low-order dynamical models for rapid thermal systems. Gunes et al [70] applied the POD technique to reconstruct the first six modes for numerical time-dependent transitional free convection in a vertical channel. A low-order system of ODE's based on knowledge of the most energetic modes in the flow was able to predict stable oscillations with correct amplitudes and frequencies. The same approach [125] was used to investigate the dynamics of transitional flow and heat transfer in a periodically grooved channel. Ukeiley [142] applied the POD technique in attempt to build a dynamical model of a turbulent mixing layer. This model was based on experimental data from two 12-probe rakes placed in the flow. Two-dimensional spanwise structures along with streamwise vortical structures were extract from the flow. The model correctly predicted the statistical distribution of energy in the cross-stream direction.

It was pointed out by Lumley [103], that the POD mode or 'characteristic eddy' represents the flow coherent structure only if it contains a dominant percentage of energy. In other cases, POD modes do not actually extract the shape of the CS, but rather simply provide an optimum basis to decompose the flow.

Poje & Lumley [119] proposed another technique to obtain information about structures in flow. They decomposed the flow into mean, coherent modes and incoherent small-scale turbulence and applied "energy method" analysis [116] to find the most energy containing large-scale modes. The results compared well the with conventional POD technique.

A.3 Wavelet Transform: Applications to turbulent flows

A.3.1 Turbulence modeling

It is well-known that turbulence has both energy spectrum cascade, which is well-described in Fourier space and spatial intermittent events, localized in space and time (e.g [105]). Consequently, the wavelet property of being local in both physical and Fourier spaces looks really attractive for application in turbulence research. Original Kolmogorov's theory of turbulence [91] was modified to incorporate experimentally discovered properties of real turbulence such as intermittency effects and energy backscatter (transfer of energy from small scales to large scales). A number of so called *hierarchical models* of 2-D and 3-D isotropic turbulence, based on the wavelet decomposition were built. One of the first attempts for 2-D turbulence was made in 1977 [127]. It utilized a *wave-packet* decomposition, which is essentially a wavelet transform. It was pointed out that the convection term in the N-S equations is essentially local in physical space and the pressure term is local in wavenumber space and guarantees the incompressibility. Thus, the Fourier space was divided in number of *shells* $b^n < |\mathbf{k}| < b^{n+1}$, $n = 1..\ln_b \Lambda_K$. Here $b \sim 2$, $\mathbf{k}$ is a wavenumber in Fourier space and Λ_K is Kolmogorov dissipation scale. Wave-

packets were introduced as a functions $\varphi_n(\mathbf{r})$ with their Fourier transform $\Phi_n(\mathbf{k})$ to have a non-zero value only within a corresponding shell. The functions φ_n are local in both Fourier and physical space. The Fourier decomposition in physical space within a shell was used to describe the functions. After projecting the N-S equations into this basis, a system of non-linear ODE's was obtained. After several simplifying assumptions, the interaction between adjacent shells was examined numerically for 4 shells x 26 Fourier mode decomposition within a shell. The resulting energy cascade and temporal intermittency was investigated.

Independently in 1984 [149] essentially the same approach was taken to build a model of 3-D turbulence. A basis function with a non-zero value within a shell was introduced. After inverse transformation, the physical representation was obtained. These *eddies* were distributed in physical space randomly and were allowed to move. After projecting the N-S equations onto this basis a system of non-linear ODE's was investigated. The model was found to exhibit qualitative agreement with experimental data. Later this model was modified using an eddy representation in wavelet form in [150]. This model does not involve any empirical assumptions and possesses some important features of the turbulence, including a $k^{-5/3}$ variation in the wavenumber spectrum. The model describes non-local interactions between the scales and back-scatter of energy from small scales to large scales. It can be used as a basis for subgrid modeling of non-equilibrium turbulence.

In [16] a *hierarchical-tree* model of 2-D turbulence was presented. The cascade of vortices was arranged in a tree-like structure, with smaller 'children' vortices connected to a bigger 'parent' vortex from the previous level. The main difference from the shell-based models was that the distances between 'parent' and 'children' physical vortices were kept fixed. Thus the new variables for this Hamiltonian model were the amplitudes of vortices and the relative angles between adjacent vortices. An almost orthogonal basis of discrete wavelets was used. The model reveals the spatial intermittent events and their fractal properties were obtained. The model showed good agreement with the theoretically predicted energy cascade for 2-D turbulence.

One of the first applications of wavelets in turbulence was done by Farge et al [51], where an optimally constructed wavelet decomposition was proposed to reduce the number of basis functions (modes) required to describe turbulence evolution. Investigating the evolution of a truncated subset of important modes, they have shown better performance of the wavelet decomposition against the standard Fourier decomposition. Another classical paper in this area is [50], where a brief theory and the basic properties of the wavelets and their application to turbulence is well-presented.

In [98] the wavelet transformation was applied to the analysis of different turbulent flows. It was pointed out that the wavelets closely resemble the 'eddy' structures introduced by Lumley [135] as the building blocks for turbulence. The brief theory and basic properties of the continuous wavelet transformation were presented. In shock wave/free turbulence interaction the advantage of the wavelet transform to detect discontinuities of a signal (front of a shock-wave) has been demonstrated. Thus, intermittent events can be easily localized using 'Mexican hat' wavelets. Another example concerning wall turbulence was considered. The wavelet technique was compared with VITA technique [27] for a detection of sweep and ejection events taking places in the boundary layer. It was found that the VITA technique could give false or no detections of these burst-like events and requires some knowledge about the characteristic scales of the events. This is due to the fact that the VITA technique is *a single scale filtered technique.* Because of variable scaled filtered property of the wavelet transformation it detects all the events well and does not require any *a priori information* of the events to be detected. Also

101

a discretized version of the wavelet transformation was proposed as a competitive technique in CFD (versus Fourier based techniques) for flows with large local gradients or discontinuities.

In [20] coherent structures (ejections and sweeps) in a heated turbulent boundary layer were investigated. Regions near the viscous sublayer $y^+ = 7$ and a fully turbulent central region $y^+ = 180$ were considered and both velocity and thermal measurements were taken in these regions using cold and hot wire probes. Several techniques like VITA, WAG (Window Averaged Gradients)[26] and wavelet analysis based on the Morlet mother function were used to analyze the intermittent events. Conditional spectra for cooling (ejection) and heating (sweeps) events were obtained. The ejections were found to be relatively slow more localized events with comparison to more rapid sweep events.

In [106], [107] a discretized version of the three-dimensional wavelet transformation using Lemarie-Meyer-Battle (LMB) wavelet was applied for both experimental (wake behind a cylinder) and numerically simulated turbulent flows. Spatially dependent quantities like total kinetic energy $E(k, x)$, net transfer to the wavenumber k, $T(k, x)$ and total flux through the wavenumber k to all smaller scales, $\pi(k, x)$ were derived using wavelet analysis. Analysis of these quantities from experimental data have shown a significant level of spatial intermittency with large variations from the mean values at smaller scales. Spatial pdf's for the energy distribution and dissipation were obtained and revealed the existence of long exponential tails. Several versions of the wavelet mother function were used to verify the robustness of the results. The wavelet results revealed a multifractal nature of the turbulence at small scales and some fractal statistics (the generalized dimensions) of the multifractal turbulence were calculated. An additive mixed multifractal cascade model was built and was shown to duplicate all the essential results of the experiments. The multifractal behavior of turbulence was also explored in [105].

A similar approach of analyzing the generalized dimensions of turbulence was taken in [95]. Again, the turbulence was treated as a multifractal process and the continuous wavelet transformation was applied to the equations of motion. The author was able to come up with the system of dynamical equations for an evolution of the generalized dimensions based on the dynamics of Navier-Stokes equations. Thus, a model which possesses both multifractal thermodynamical properties and the dynamics inherent to N-S equations was proposed.

An application of the discrete wavelet transform to explore the intermittency in turbulent flows was the purpose of the work reported by [34]. The authors established a firm connection between the intermittent events and underlying coherent structures. Using experimental data for isotropic turbulence behind a grid, they found that the flow exhibits a high degree of intermittency for $Re_\lambda \geq 10$. Also applying a phase-averaged velocity based technique on the wavelet transform, they were able to reconstruct the 'signature' of the coherent structures corresponding to the intermittent events. For an isotropic turbulence a typical size of the small-scale filamentary-like structures have been found as of (4..5) Kolmogorov scales , with these structures capturing about 1% of the flow energy. For a jet-generated turbulence ($Re_\lambda = 250..800$) large-scale structures (vortex rings) from a longitudinal component of velocity as well as small-scale structures (filamentary structures) from a transverse component were found. A strong phase correlation between the large and small scale structures was observed. The universality of a scaling exponents $\xi(p)$ in Kolmogorov's scaling law $|U(x + r) - U(x)|^p \sim r^{\xi(p)}$ for $p = 2..6$ was verified for a grid generated turbulence and turbulent jet flows for moderate Re_λ.

A transition to turbulence in a shear layer was investigated using the continuous wavelet transform in [28]. A pairing process was found to be intermittent in the region where the subharmonic dominates over the fundamental mode, with the intermittency being stronger for large scales of motion.

In [132] flow behind a sphere in a stratified fluid was analyzed for a range of Re and Fr numbers. The Particle Image Velocimetry (PIV) technique was used to get the velocity field. The two-dimensional version of the Morlet wavelet was applied to obtain spatially local length scales, as well as local Re and Fr numbers. Spatial distributions of Re and Fr were found to be similar. Vortex core centers were marked by very low Re and Fr numbers.

In [47] 2-D turbulence from an axisymmetric jet with $Re_D = 4,000$ was investigated. A two-dimensional version of the 'Mexican Hat' wavelet was used to decompose dye concentration pictures. Two different structures, consisting of both large-scale *beads* and small-scale *strings* were observed. Strings were found to be strongly anisotropic structures with an essential lack of self-similarity across scales.

Structures in the initial and transient regions of a planar jet were the focus in [96] and [97]. Small-scale structures within large ones were found, with large-scale structures moving slower than the small ones. Wavelet cross-correlation analysis was developed in this research as well. In [28] a continuous wavelet analysis was applied to investigate transition in a turbulent mixing layer. It revealed that the paring process is intermittent. In [73] intermittent events on different scales in the atmospheric boundary layer were reported by applying the wavelet technique. In [40], [41] several techniques like wavelet transform, VITA and WAG were applied to wind velocity data . Intermittent coherent large and small structures were discovered and investigated. Dynamics of the sweep-ejection process was discussed and the obtained results were found in agreement with previous results. In [63], [66] a shear layer in a region of strong interaction between a fundamental and subharmonic modes was investigated by a continuous Morlet wavelet transform. Intermittent π-shifts in subharmonic phase were discovered. Motivated by the experimental data, a dynamical Hamiltonian model based on structural interactions of vortices was proposed and it was shown that the model exhibits very good agreement with the experiment.

Multiple acoustic modes in an underexpended supersonic rectangular jet were investigated by the wavelet transform in [144]. The acoustic modes were found to exist simultaneously and did not exhibit a mode switching. Detailed wavelet-based analysis of acoustic mode behavior in supersonic jets can be found in [65]

In [87] new methods for investigating complex structures based on fractals and wavelet analysis were presented. The application of the wavelet transform was shown to provide a simple functional description in terms of local length scales and the distribution of velocity and vorticity within turbulence structures. In [72] several techniques for analysis of turbulent flows were discussed. The wavelet transform was found useful to detect intermittent events and turbulent structures in flows.

The wavelet transform was successfully used as a diagnostic tool in seismology [67], cardiology [111], in diagnostics of engine cylinders [146]. In optics, an optical version of wavelet transform (OWT) was introduced in [120]. Also the wavelet transform is actively used in multifractal analysis [14], [12], information theory [104], pattern recognition [94].

A.4   Some other wavelet-like techniques.

A.4.1   Windowed Fourier transformation

The main problem with the Fourier transform as a tool to analyze a temporal evolution of a signal is that the basis functions $\exp(i\omega t)$ do not belong to $L^2(\mathbf{R})$. In other words, they have an infinite span in physical space and provide no information about spatial localization of the signal. This problem could be overcome, if the signal is *windowed* or multiplied by a function with local physical support $w(t)$. This idea was introduced by Gabor in 1946 [55]. The windowed transformation is as follows

$$L(\tau, \omega) = \int f(t)\overline{w}(t - \tau)e^{-i\omega(t-\tau)}dt \tag{A.1}$$

In practice, two kinds of $w(t)$ are widely used: (1) a cosine window $cos(\pi/2\ t)$, $t \in [-1, 1]$ and (2) a Gabor packet $\exp(-t^2/2\sigma^2)$. Transform (A.1) resembles (4.1), but provides *a fixed time window* for any ω. This time window can be varied by an appropriate dilatation of $w(t)$, though.

A.4.2   Variable Integral Time Averaging (VITA)

VITA technique was introduced in 1976 [27]. The idea is to look for a short-time averaging version of RMS of the signal,

$$
\begin{aligned}
var(t, T) &= \frac{1}{T}\int_{t-T/2}^{t+T/2} f(t)^2 dt - \left(\frac{1}{T}\int_{t-T/2}^{t+T/2} f(t)dt\right)^2 \\
\sigma_f &= \lim_{T \to \infty} var(t, T)\ -\ RMS\ of\ the\ signal
\end{aligned}
$$

The event is said to be detected if $var(t, T) > K \cdot \sigma_f$

The technique introduces two parameters which can be varied, T and K. This technique is valid only for *second-order stationary signals*. It uses a fixed time window, which means *low-pass single scale filtering*. Problems with VITA are listed below,

1. Choice of T and K is intricate.

2. Does NOT detect events separated by time less than T.

3. Possible false detections.

4. Smoothing of some events.

A.4.3   Window Averaged Gradients (WAG)

Another technique to detect sudden changes in velocity signal was proposed in [26] and it is based on the analysis of the average gradients.

$$WAG(t, T) = \frac{1}{\sigma_f}\frac{1}{T}\left[\int_{t-T/2}^{t} f(t)dt - \int_{t}^{t+T/2} f(t)dt\right]$$

The event is detected when $WAG(t, T) > \beta \cdot u'_{RMS}$. WAG has similar problems as VITA technique: single scale filtering, applied for stationary signals only.

Appendix B

CONSTANT TEMPERATURE ANEMOMETRY TRANSDUCER

The principal layout for the CTA transducer that was built in house for use in this study is given in Figure B.1. It is a modified version of the transducer used by Citriniti [37]. Four CTA anemometer units are contained on a single to one board along with the built-in low-pass filter for each transducer. The filter cut-off frequency can be set between 1 and 25 kHz. Each X-wire was connected to a transducer by a three-feet thin co-axial cable, manufactured by Belden Wire and Cable Co. (type 8700, NEC type CXC FT1) of three feet length to reduce background noise. The outputs from the transducers were sampled and digitized by a four daisy-chained MicroStar Laboratories Analog/Digital Simultaneous Sample-and-Hold Boards, part number MSXB 028, each capable of acquiring 16 analog signals simultaneously. The total number of channels is 64 channels. The maximum sampling frequency with no detectable phase lag for 48 channels (=24 x-wires × 2 channels-per-x-wire) was found to be 33 kHz/channel.

CONSTANT TEMPERATURE ANEMOMETER
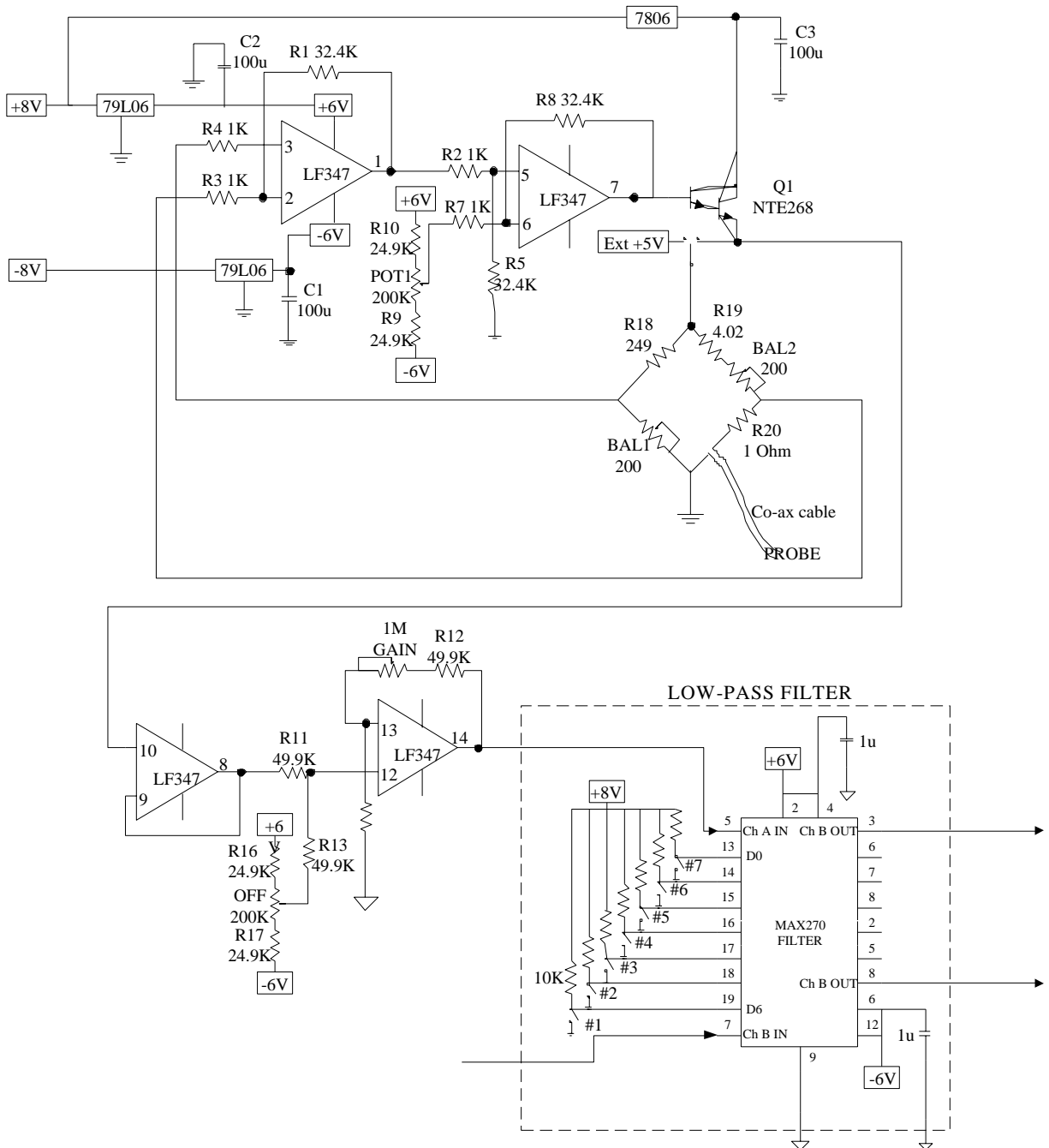
Figure B.1: Schematic layout of the CTA transducer.

Appendix C

LOOK-UP TABLE PROCEDURE

The response of each probe (e_1, e_2) to a known velocity vector (q, θ) in polar coordinates is given as a discrete mapping from the velocity to voltage spaces, $M : (u, v) \longmapsto (e1, e2)$. During the experiment, the inverse mapping $M^{-1} : (e1, e2) \longmapsto (u, v) = (q \cos(\theta), q \sin(\theta))$ gives a way to convert a voltage pair into a velocity vector. See Figure C.1 for a graphical explanation of the mapping.
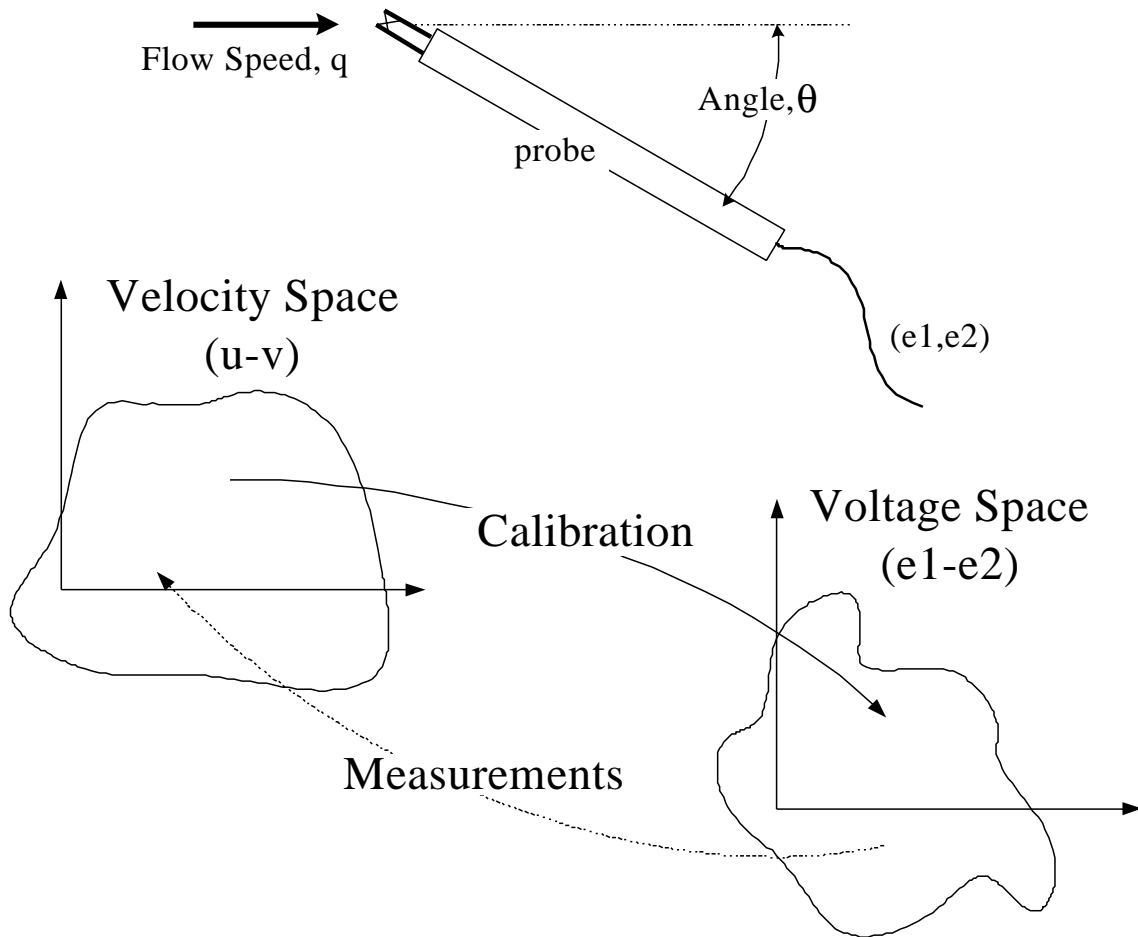
Figure C.1: Mapping procedure.

The fitting surface $(u, v) = f(e_1, e_2)$ for the inverse mapping was found experimentally as follows,

1. From the calibration procedure, a relationship between the velocity and voltages was obtained at finite points $(q_c, \theta_c) = [0..U_0] \times [-45°..45°]$,

$$
\begin{aligned}
e_1 &= e_1(q_c, \theta_c) \\
e_2 &= e_2(q_c, \theta_c)
\end{aligned}
$$

2. Second-order polynomials were fitted though all (e_1, e_2) corresponded to given fixed calibration angles θ_c,

$$
e_1(e_2(q_c); \theta_c) = A(\theta_c)e_2^2 + B(\theta_c)e_2 + C(\theta_c). \tag{C.1}
$$

3. The single wire response for moderate speeds is known to satisfy King's law [61], $E^2 = C_1 + C_2\sqrt{U}$, $U \geq 3$ $m/\sec$. For the small velocities a series of tests showed that the wire response follows a power law, $E \sim U^n$, $n = 3 \div 3.5$. Based on this information, an empirically constructed *Power-King's Law function* was fitted along each line $\theta_c = const$, using the least-square technique,

$$
\begin{aligned}
q(x; \theta_c) &= \left[D(\theta_c)x^{\frac{m}{m-1}} + E(\theta_c)x^{\frac{1}{1-m}} \right]^{2(1-m)} \tag{C.2} \\
&= \begin{cases} \sim x^m, & x \to 0 \text{ (Power Law)} \\ \sim (x + const)^2, & x \to \infty \text{ (King's Law)} \end{cases}
\end{aligned}
$$

where $x = e_1^2(\theta_c) + e_2^2(\theta_c)$, $m = m(\theta_c)$. This empirical function was found to give the best single fitting function for all ranges of q and θ.

4. The coefficient functions $A(\theta)$, $B(\theta)$, $C(\theta)$, $D(\theta)$, $E(\theta)$, and $m(\theta)$ were linearly interpolated for all $\theta = -45°..45°$.

5. The reconstruction procedure for a given pair of voltages (e_1, e_2) solves (C.1) using Newton's method to find θ and a direct substitution into (C.2) gives q. Thus, the velocity vector $(u, v) = (q\cos(\theta), q\sin(\theta))$ is found.

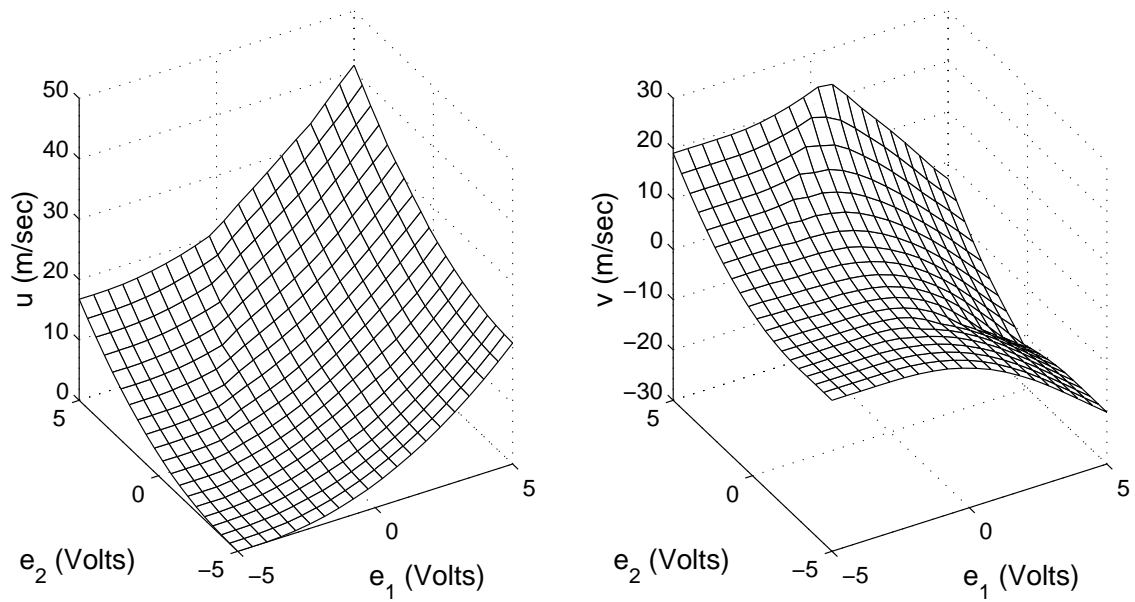An example of the calibration fitting surfaces $u = u(e_1, e_2)$ and $v = v(e_1, e_2)$ is shown in Figure C.2.

108

Figure C.2: Fitting surfaces $u = u(e_1, e_2)$ and $v = v(e_1, e_2)$.

Appendix D

NUMERICAL INTEGRATION

Let the function $f(t) \in C[a, b]$ be given at discrete equally spaced points $\{t_i\}$, $i = 0..N$, with $\Delta t = t_{i+1} - t_i = \Delta t = (b - a)/N = const$. Thus, the continuous integration

$$\int_a^b f(t)dt = \sum_{n=0}^N \int_{t_i}^{t_{i+1}} f(t)dt \tag{D.1}$$

can be approximated by a finite summation by interpolating the function $f(t)$ inside the interval $[t_i, t_{i+1}]$. If the trapezoidal rule is chosen,

$$\int_{t_i}^{t_{i+1}} f(t)dt \approx \frac{\Delta t}{2}[f(t_i) + f(t_{i+1})] \tag{D.2}$$

After substituting (D.2) into (D.1) and rearranging terms, one can get the expression for the integral approximation,

$$\int_a^b f(t)dt \approx \Delta t \left\{ 0.5[f(t_0) + f(t_1)] + ... + 0.5[f(t_{N-1}) + f(t_N)] \right\}$$
$$= \Delta t \left\{ 0.5f(t_0) + f(t_1) + ... + f(t_{N-1}) + 0.5f(t_N) \right\} = \Delta t \sum_{n=0}^N w(n)f(n) \tag{D.3}$$

where $w(n)$ is called a *weighting function*. For the above interpolation,

$w(n) = (0.5, \overbrace{1, 1, .., 1}^{N-1}, 0.5)$ and is called a *trapezoidal weighting function*. Using Taylor's series for $f(t)$ around t_i, $f(t) = f(t_i) + f'(t_i)(t - t_i) + f''(t_i)(t - t_i)^2/2 + ...$ and performing integration (D.2), one can find that

$$\int_{t_i}^{t_{i+1}} f(t)dt = f(t_i)\Delta t + f'(t_i)\frac{\Delta t^2}{2} + f''(t_i)\frac{\Delta t^3}{3} + O(\Delta t^4) \tag{D.4}$$

On the other hand,

$$\frac{\Delta t}{2}[f(t_i) + f(t_{i+1})] = \frac{\Delta t}{2}[f(t_i) + f(t_i) + f'(t_i)\Delta t + f''(t_i)\frac{\Delta t^2}{2} + O(\Delta t^3)]$$
$$= \Delta t[f(t_i) + f'(t_i)\frac{\Delta t}{2} + f''(t_i)\frac{\Delta t^2}{4} + O(\Delta t^3)] \tag{D.5}$$

Subtracting (D.5) from (D.4),

$$\int_{t_i}^{t_{i+1}} f(t)dt - \frac{\Delta t}{2}[f(t_i) + f(t_{i+1})] = f''(t_i)\frac{\Delta t^2}{12} + O(\Delta t^3) \tag{D.6}$$

Finally, performing summation over all time intervals,

$$\int_a^b f(t)dt - \sum_{n=0}^N \int_{t_i}^{t_{i+1}} f(t)dt \approx \sum_{n=0}^N f^{''}(t_i)\frac{\Delta t^2}{12} < \max_{t \in [a,b]} f''(t) \left(\frac{(b-a)}{N}\right)^2 N = C(b-a)\Delta t \quad \text{(D.7)}$$

So, the finite approximation (D.3) is of the first order in Δt.

Appendix E

SELF-SIMILARITY OF THE SECOND POD MODE

In addition to the first mode eigenvalues, the second mode was investigated to investigate the possible self-similarity of the corresponding eigenvalues.

Figure E.1 presents the scaled mode 2, u-component eigenvalues. The figure shows the variation of the planar mode ($k_z = 0$) eigenvalues, $\tilde{\lambda}_1^{(2)}$, with St for $50 \leq x/D \leq 90$. In addition, the variation of $\tilde{\lambda}_1^{(2)}$ with $k_z b$ is shown for four representative values of St over the same streamwise locations. This figure shows that the scaled u-component eigenvalue distribution becomes self-similar for $x/D > 50$

Figure E.2 shows a similar representation of the scaled mode 2, v-component eigenvalues, $\tilde{\lambda}_2^{(2)}$. The variation of the planar mode ($k_z = 0$) eigenvalues with St for selected streamwise locations is shown to exhibit similarity. In addition, the variation with spanwise wavenumber $k_z b$ for selected St also exhibits collapse for the various x/D locations shown. Figure E.2 shows that the v-component mode eigenvalues exhibit similarity scaling for $x/D \geq 50$.

The scaled, w-component, mode 2 eigenvalues are shown in Figure E.3. These figures also show evidence of self- similar behavior for $\tilde{\lambda}_3^{(2)}$. The data suggest that self-similar behavior for the second w-component eigenvalues occurs only for $x/D > 60$.

Although not shown here, all experimentally resolved POD modes were found to exhibit a self-similarity shape in the region $x/D = 50..90$.

Figure E.1: Scaled eigenvalues $\widetilde{\lambda}_1^{(2)}(St, k_z; x/D)$ for the second u-mode.
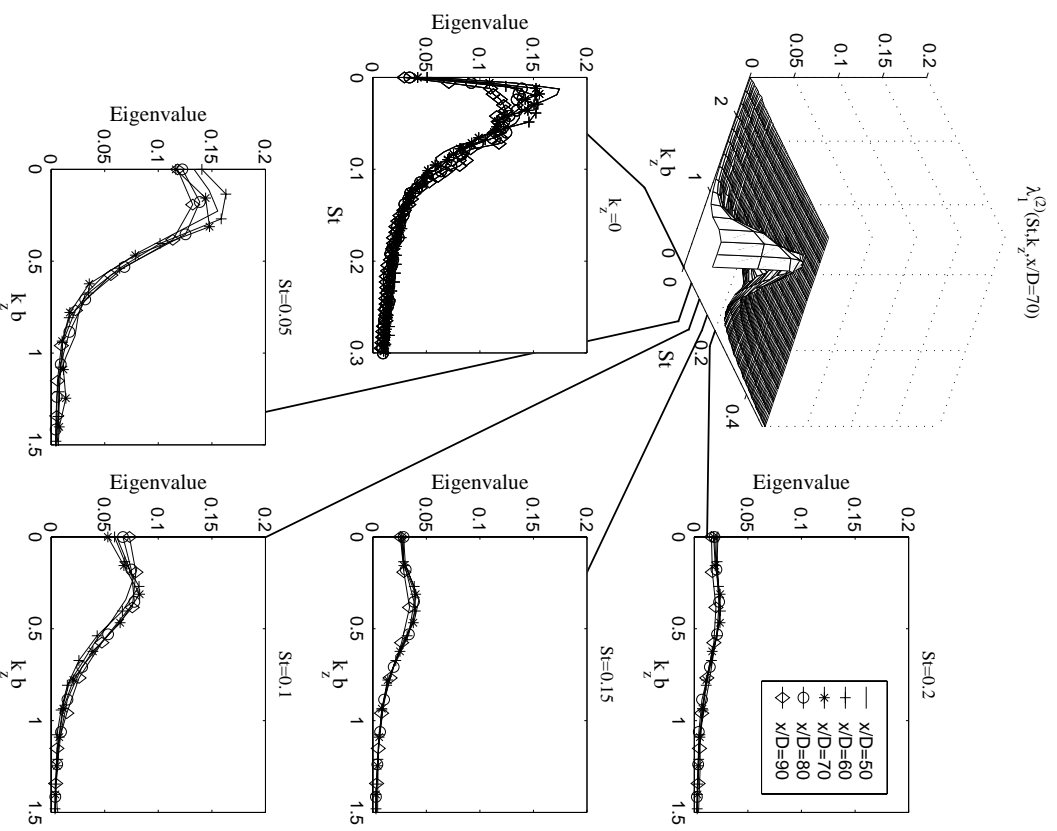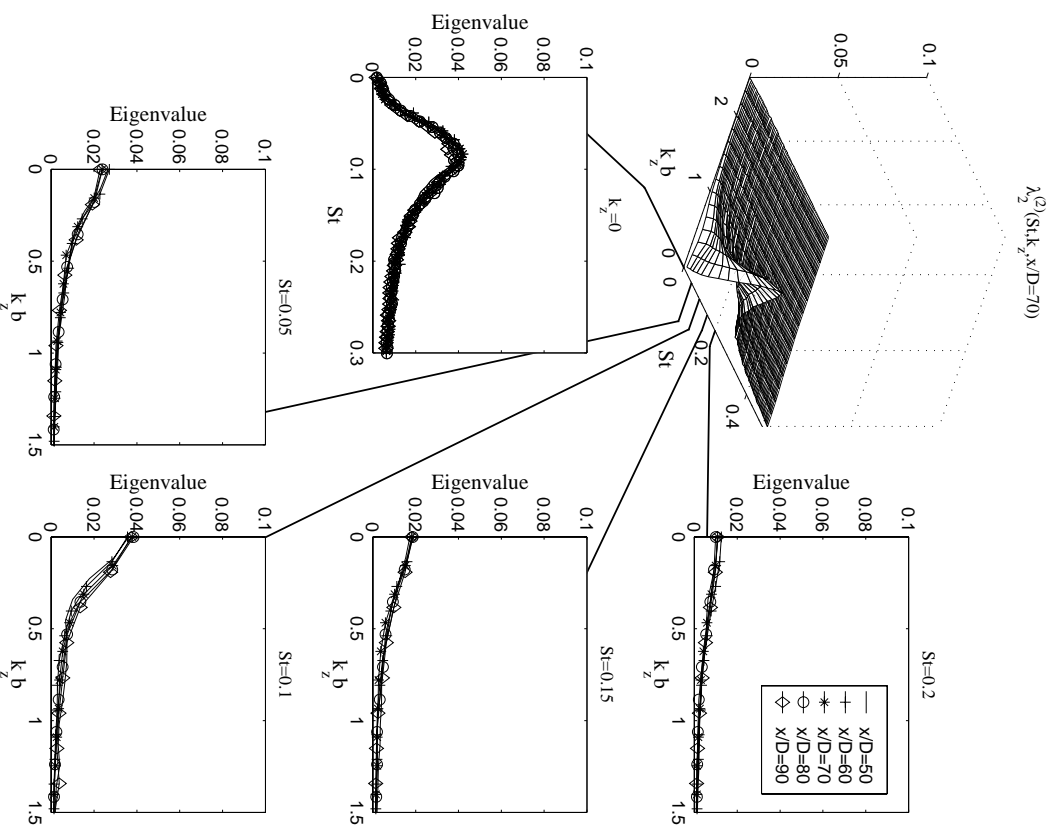
113

Figure E.2: Scaled eigenvalues $\widetilde{\lambda}_2^{(2)}$ ($St, k_z; x/D$) for the second v-mode.
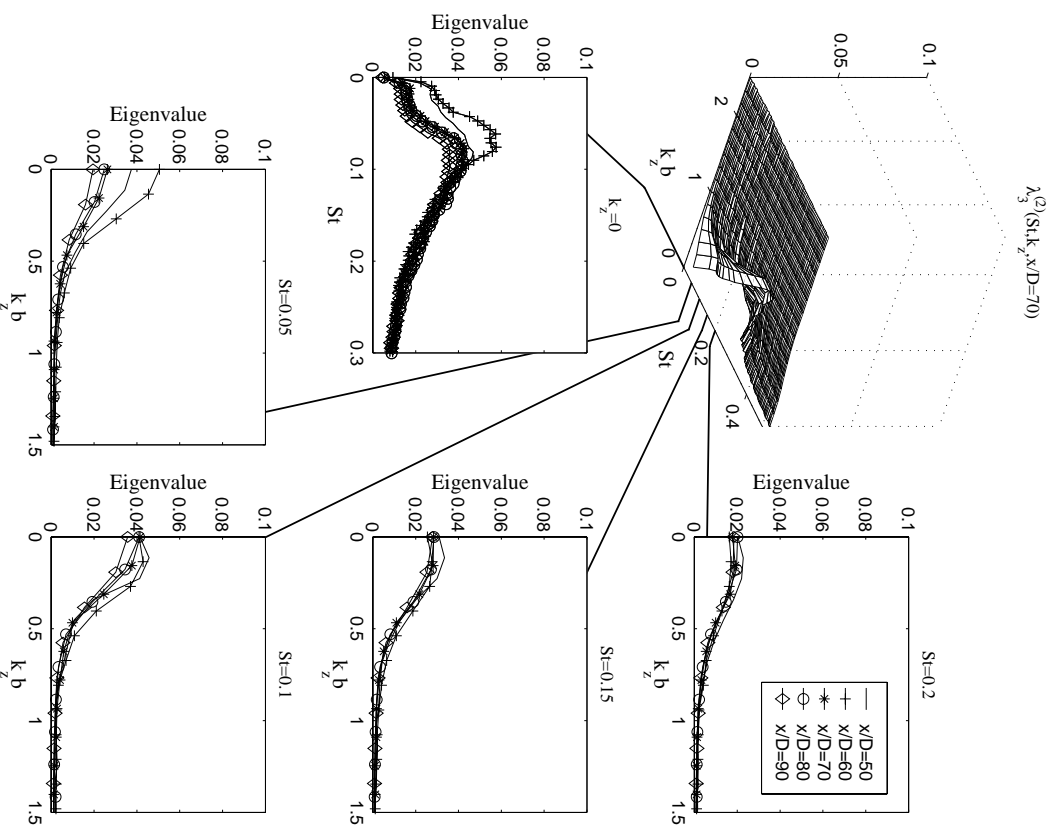
Figure E.3: Scaled eigenvalues $\tilde{\lambda}_3^{(2)}(St, k_z; x/D)$ for the second w-mode.

Bibliography

[1] Abramovich, G.N., 'The Theory of Turbulent Jets', The MIT Press, Cambridge, Mass., 1963

[2] Adrian, R.J., 'On the role of conditional averages in turbulent theory', In: *Turbulence in Liquids: Proceedings of the 4th Biennial Symposium on Turbulence in Liquids*, ed. G. Patteson and J. Zakin, Science Press, Princeton, 1977, pp. 322-332

[3] Adrian R. ,'Conditional eddies in isotropic turbulence', *Phys. Fluids* (1979), **22**(11), pp.2065-2070

[4] Ahmed N., Goldstein H.,'Orthogonal Transforms for Digital Signal Processing', Springer-Verlag, N.Y.(1975)

[5] Aling, H.; Banerjee, S.; Bangia, A.K.; Cole, V.; Ebert, J.; Emami-Naeini, A.; Jensen, K.F.; Kevrekidis, I.G.; Shvartsman, S., 'Nonlinear model reduction for simulation and control of rapid thermal processing', *Proceedings of the 1997 American Control Conference*, **4**, 1997, pp. 2233-2238

[6] V.R Algazi and D.J. Sakrison, 'On the Optimality of the Karhunen-Loève Expansion', *IEEE Trans. Inform. Theory*, (1969), **15**, pp.319-321

[7] Antonia, R.A., Browne, L.W.B., Rajagopalan, S., Chambers, A.J., 'On the organized motion of a turbulent plane jet', *Journal of Fluid Mechanics*, 1983, **134**, pp. 49-66

[8] Antonia, R.A., Chambes, A.J., Britz, D., Browne, L.W.B. 'Organized structures in a turbulent plane jet: topology and contribution to momentum and heat transport', *Journal of Fluid Mechanics*, 1986, **172**, pp. 211-229

[9] Antonia, R.,'Conditional sampling in turbulence measurements', *Ann. Rev. Fluid Mech.*, **13**, 1981, pp. 131-156

[10] Ash. R., Gardner M.,'Topics in Stochastic Processes', Academic Press, N.Y. (1975)

[11] Argoul, F., Arneodo, A., Grasseau, G., Gagne, Y., Hopfinder, E., Frisch, U., 'Wavelet Analysis of Turbulence Reveals the Multifractal Nature of the Richardson Cascade', *Nature*, **338**(6210), 1989, pp. 51-53

[12] Argoul, F., Arneodo, A., Elezgaray, J., Grasseau, G., Murenzi,'Wavelet analysis of the self-similarity of diffusion-limited aggregates and electrodeposition cluster', *Physical Review A,* **41**, 1990, pp. 5537-5560

[13] Arndt, R.E.A., Long, D.F., Glauser, M.N., 'Proper orthogonal decomposition of pressure fluctuations surrounding a turbulent jet', *Journal of Fluid Mechanics*, **340**, 1997, pp. 1-33

[14] Arneodo, A., Grasseau, G., Holschneider, M., 'Wavelet transform of multifractals', *Physical Review Letters*, **61**, 1988, pp. 2281-2284

[15] Aubry, Holmes, Lumley, Stone ,'The dynamics of Coherent Structures in the wall region of turbulent shear layer', *J. Fluid Mech.* (1988), **192**, pp. 115-175

[16] Aurell, E., Frick, P., Shaidurov, V., 'Hierarchical tree-model of 2D-turbulence', *Physica D*, **72**, 1994, pp. 95-109

[17] Bakewell H., Lumley J.,'Viscous sublayer and adjacent wall region in turbulent pipe flows', *Phys. Fluids* (1967), **10**(9), pp. 1880-1889

[18] Ball K., Sirovich K., Keefe L.,'Dynamical eigenfunction decomposition of turbulent channel flow', *Int. J. for Num. Meth. in Fluids* (1991), **12**, pp. 585-604

[19] Bargmann, V., 'On a Hilbert space of analytic functions and an associated integral transform', Part I, *Comm. Pure Appl. Math,* **14**, 1961, pp. 187-214: Part II, *Comm. Pure Appl. Math,* **20**, 1967, pp. 1-101

[20] Benaissa, A., Liandrat, J., Anselmet, F,. 'Spectral contribution of coherent motions in a turbulent boundary layer', *European Journal of Mechanics B-Fluids*, **14**(6), 1995. pp. 697-718

[21] Bendat, J.S., Piersol, A.G., 'Random Data. Analysis and Measurement Procedures', a Wiley-Interscience Publication, John Wiley & Sons, 1986

[22] Berkooz, G., Holmes, P., Lumley, J., 'The proper orthogonal decomposition in the analysis of turbulent flows', *Annual Review of Fluid Mechanics*, **25**, 1993, pp. 539-575

[23] Berkooz, Elengaray, Holmes, Lumley, Poje,'The POD, wavelets and Modal Applications to the dynamics of coherent structures', *Appl. Scientific Research* (1994), **53**, DEC, pp.

[24] Bienkiewicz, B., 'New tools in wind engineering', *Journal of Wind Engineering and Industrial Aerodynamics*, 1996, **65**, pp. 279-300

[25] Bienkiewicz, B., Tamura, Y., Ham, H.J., Ueda, H., Hibi, K., 'Proper orthogonal decomposition and reconstruction of multi-channel roof pressure', *Journal of Wind Engineering and Industrial Aerodynamics,* **54-55**, 1995, pp. 369-381

[26] Bisset, D.K., Antonia, R.A., Browne, L.W.B., 'Spatial organization of large structures in the turbulent far wake of a cylinder', *Journal of Fluid Mechanics*, **218**, 1990, pp. 439-461

[27] Blackwelder, R.F., Kaplan, R.E, 'On the wall structure of the turbulent boundary layer', *Journal of Fluid Mechanics,* 1976, **76**, pp. 89-112

[28] Bokde, A L W., Jordan, D A Jr., Miksad, R W., 'Experimental investigation of the temporal intermittency in the transition to turbulence of a plane mixing layer', *Proceedings of Engineering Mechanics*, *11th Conference on Engineering Mechanics,* **2,** 1996, ASCE, New York, NY, USA. pp. 1070-1073

[29] Bradbury, L.J.S, 'The structure of a self-preserving turbulent plane jet', *Journal of Fluid Mechanics*, **23**(1), 1965, pp. 31-64

[30] Breteton, G.J., 'Stochastic estimation as a statistical tool for approximating turbulent conditional averages', *Phys. Fluids, A*, (1992), **4,** pp. 2046-2054

[31] Brooks, C. L., Karplus, M., and Pettitt, B.M., 'Proteins: a Theoretical Perspective of Dynamics, Structure and Thermodynamics', New York: Wiley, 1988

[32] Brown G., Roshko A.,'On density effects and large structure in turbulent mixing layer', *J. Fluid. Mech.* (1974), **64**, pp. 775-816

[33] Browne, L. W. B., Antonia, R. A., and Chambers, A. J.,'The interaction region of a turbulent plane jet,' *J. Fluid Mech.*, 1984, **149**, pp. 355-373.

[34] Camussi, R., Guj, G., 'Orthonormal wavelet decomposition of turbulent flows: intermittency and coherent structures', *Journal of Fluid Mechanics*, 1997, **348,** pp. 177-199

[35] Cantwell B. ,'Organized Motion in turbulent flow', *Ann. Rev. Fluid Mech* (1981), **13**, pp. 457-515

[36] Cervantes, D.G, Golgschmidt, V.W.,'The apparent flapping motion of a turbulent plane jet-further experimental results', *Trans. ASME J. Fluid Eng.* (1981), **103**, pp. 119-126

[37] Citriniti, J., 'Experimental investigation into the dynamics of the axisymmetric mixing layer utilizing the proper Orthogonal Decomposition', Ph.D Dissertation, SUNY at Buffalo, 1996

[38] Chambers, Adrian, Moin, Steward, Sund,'Karhunen-Loeve expansion of Burger's model of turbulence', *Phys. Fluids* (1988), **31**(9), pp. 2573-2582

[39] Chu H.C. 'An experimental study of nonlinear wave coupling and energy transfer characterizing the transition of a planar jet shear layer', Ph.D. dissertation, University of Notre Dame, 1993

[40] Collineau, S., Brunet, Y., 'Detection of turbulent motions in a forest canopy, Part I: Wavelet analysis', *Boundary-Layer Meteorology,* **65**, 1993, pp. 357-379

[41] Collineau, S., Brunet, Y., 'Detection of turbulent motions in a forest canopy, Part II: Time-scale and conditional averages', *Boundary-Layer Meteorology,* **66**, 1993, pp. 49-73

[42] Daubechies, I., 'Orthonormal bases of compactly supported wavelets', *Communications on Pure and Applied Mathematics,* **41**, 1988, pp. 909-996

[43] Daubechies, I., 'Ten lectures on wavelets', *CBMS Lectures Notes Series, SIAM,* 1991

[44] Delville, J., 'Characterization of the organization in shear layers via the proper orthogonal decomposition', *Applied Scientific Research*, **53**(3-4), 1994, pp. 263-281

[45] Delville, J., Ukeiley, L., Cordier, L., Bonnet, J. P., and Glauser, M., 'Examination of Large Scale Structures in a Plane Mixing Layer. Part 1. Proper Orthogonal Decomposition,' *J. Fluid Mech.*, **391**, 1999, pp. 91-122

[46] Everitt, K.W., Robins, A.G., The development and structure of turbulent plane jets', *Journal of Fluid Mechanics*, **88**(3), 1978, pp. 563-583

[47] Everson, R., Sirovich, L., Sreenivasan, K.R., 'Wavelet analysis of the turbulent jet', *Phys. Lett. A*, **145**, 1990, pp. 314-322

[48] Ewing, D., 'On Multi-Point Similarity Solutions in Turbulent Free-Shear Flows', *Ph.D Dissertation*, 1995, SUNY at Buffalo, Amherst, New York

[49] Scanning the special issue on wavelets, *Proceedings of the IEEE,* **84**(4), 1996

[50] Farge, M., 'Wavelet transforms and their applications to turbulence', *Annual Rev. Fluid Mech.*, **24**, 1992, pp. 395-457

[51] Farge, M, Goirand, E, Meyer, Y., Pascal, F., Wickerhauser, M.V., 'Improved predictability of two-dimensional turbulent flows using wavelet packet compression', *Fluid Dynamics Research*, **10**(4-6), 1992, pp. 229-250

[52] Farge, M, Kevlahan, N, Perrier, V, Goirand, U, 'Wavelets and Turbulence', Proceedings of the IEEE, **84**(4) 1996, pp. 639-669

[53] Flora, J. J. and Goldschmidt, V. W., 'Virtual origins of a free plane turbulent jet,' *AIAA Journal*, **7**(12), 1969, pp. 2344-2346.

[54] Fukunaga K.,'Introduction to Statistical Pattern Recognition', Academic Press N.Y. (1972)

[55] Gabor, D., 'Theory of communication', *J. Inst. Electr. Engin.,* London, **93**(III), 1946, pp. 429-457

[56] Gavrilakis, S., 'Turbulent-field modes in the vicinity of the walls of a square duct', *European Journal of Mechanics, B/Fluids*, **16**(1), 1997, pp. 121-139

[57] Glauser, Lieb, George,'Coherent structure in axisymmetric jet mixing layer', *Turbulent Shear Flows* (1987), **5**, pp.134-145

[58] Glauser, M.N., George, W.K., 'Application of Multipoint Measuremensts for flow chacarterizaton', *Experimental Thermal and Fluid Science*, (1992),**5**(5), pp. 617-632

[59] Goldschmidt, V.W., Bradshaw, P, 'Flapping of a plane jet', *Physics of Fluids*, 1973, **16**, pp.354-355

[60] Goldschmidt, V. W., Young, M. F., and Ott, E. S.,'Turbulent convective velocities (broadband and wavenumber dependent) in a plane jet,' *J. Fluid Mech.*, 1981, **108**, pp. 327-345.

[61] 'Fluid Mechanics Measurements', ed. by R.J. Goldstein, Taylor&Francis, 1996

[62] Golub, G.H., Van Loan, C.F., 'Matrix Computations', Oxford: North Oxford Academic, 1983

[63] Gordeyev, S., Thomas, F.O., Chu, H.C., 'Experimental investigation of unsteady jet shear layer dynamics using a wavelet decomposition', *ASME, Fluid Engineering Division, Unsteady Flows,* **216**, 1995, pp. 167-172

[64] Gordeyev, S., Thomas, F.O. 'Large scale structure in the interaction and similarity region of a planar jet via the Proper Orthogonal Decomposition', *Bull. Amer. Phys. Soc..* **42**(11), 1997, pp. 2115

[65] Gordeyev, S.V, Thomas, F.O., 'Characterization of unsteady aspects of jet screech using a wavelet analysis technique', *Final Project Report for Boeing Corporation,* PO#Z70423, 1997

[66] Gordeyev, S., Thomas, F.O., 'Temporal subhamonic amplitude and phase behavior in a jet shear layer: wavelet analysis and Hamiltonian formulation', to appear in *Journal of Fluid Mechanics*

[67] Goupilland P., Grossmann, A., Morlet, J., 'Cycle octave and related transforms in seismic signal analysis', *Geoexploration,* **23**, 1984, pp. 85-102

[68] Graham, M.D., Kevrekidis, I.G.,'Alternative approaches to the Karhunen-Loève decomposition for model reduction and data analysis', *Computers and chemical engineering,* (1996), **20**, p. 495

[69] Grossmann, A., Morlet, J., 'Decomposition of Hardy functions into square integrable wavelets of constant shape', *SIAM J. Math Anal.,* **15**, 1984, p. 723

[70] Gunes, H.; Sahan, R.A.; Liakopoulos, A., 'Spatiotemporal structures of buoyancy-induced flow in a vertical channel', *Numerical Heat Transfer; A,* **32**(1)**,** 1997, pp. 51-62

[71] Gutmark, E., Wygnanski, I., 'The planar turbulent jet', *Journal of Fluid Mechanics,* **73**(3), 1976, pp. 465-495

[72] Hajj, M R., 'Analysis tools of transitioning and turbulent flows', *Proceedings of Engineering Mechanics, 11th Conference on Engineering Mechanics,* **1,** 1996, ASCE, New York, NY, USA. pp. 434-437

[73] Hajj, M.R., Tieleman, H.W., 'Application of wavelet analysis to incident wind in relevance to wind loads on low-rise structures', *Journal of Fluid Engineering,* **118**(4), 1996, pp. 874-876

[74] Harman, H., 'Modern Factor Analysis', Chicago: University of Chicago Press, 1960

[75] Herzog, S., 'The large scale structure in the near wall region of turbulent pipe flow,' Ph.D. Thesis, 1986, Cornell University.

[76] Hilberg, D.; Lazik, W.; Fiedler, H.E., 'Application of classical POD and snapshot POD in a turbulent shear layer with periodic structures', *Applied Scientific Research,* **53**, 1994, pp. 283-290

[77] Holmes, P.J., J.L. Lumley, and G. Berkooz, 'Turbulence, coherent structures, symmetry and dynamical systems'. Cambridge University Press, Cambridge, 1996.

[78] Hotelling, H, 'Analysis of a complex of statistical variables into principal components', *Journal of Educational Psychology*, (1933) **24**,pp. 417-441, 488-520

[79] Howes, Sirovich, Zang ,'Eigenfunction analysis of Rayleigh-Benard convection', *Bull. Atm. Phys. Soc* (1988), **33**, p. 2261

[80] Hussain A.K.M.F. ,'Coherent structures and studies of perturbed and unperturbed jets', *Lecture Notes in Physics* (1980), **136**

[81] Hussain A.K.M.F.,'Coherent structures-reality and myth', *Phys. Fluids* (1983), **26**, pp. 2816-2850

[82] Hussain A.K.M.F.,'Coherent structures and turbulence', *J Fluid Mech.* (1986), **173**, pp. 303-356

[83] Ishikawa, H.; Kiya, M.; Mochizuki, O.; Maekawa, H., 'POD and wavelet analysis of coherent structures in a turbulent mixing layer', *Transactions of the Japan Society of Mechanical Engineers, Part B*, **63**(610), 1997, pp. 2001-2008 (in japanese)

[84] Kaiser, G., 1994, 'A Friendly Guide to Wavelets', Birkhauser.

[85] Kaplan ,'Conditional sampling technique', *Turbulence in Fluids* (1973), University of Missouri-Rolla

[86] Karhunen, K., 'Zur Spektraltheorie Stochasticher', *Prozessa Ann. Acad. Sci. Fennicae*, (1946), **37**

[87] Kevlahan, N K -R., Hunt, J C R., Vassilicos, J C., 'Comparison of different analytical techniques for identifying structures in turbulence', *Applied Scientific Research*, **53**(3-4), 1994, pp. 339-355

[88] Kirby, Boris, Sirovich,'An eigenfunction Analysis of Axisymmetric Jet Flow', *J of Comp. Phys.* (1990), SEP, **90**, p. 98

[89] Kirby, Boris, Sirovich,'A Proper Orthogonal Decomposition of a simulated supersonic shear layer', *Int. J. for Num. Meth. in Fluids* (1990), MAY, **10**, p. 411

[90] Kline S., Reynolds W., Schraub F, Rundstadler P.,'The structure of turbulent boundary layers', *J. Fluid Mech.* (1967), **30**, pp. 741-773

[91] Kolmogorov, A.N., 'Dissipation of energy in locally isotropic turbulence', *Doklady Akademii Nauk SSSR,* **32**, 1941, pp. 16-18 (reprinted in *Proc. R. Soc. Lond. A,* **434**, 1991, pp. 15-17)

[92] Kopp, G.A.; Ferre, J.A.; Giralt, Francesc, 'Use of pattern recognition and proper orthogonal decomposition in identifying the structure of fully-developed free turbulence', *Journal of Fluids Engineering*, **119**(2), 1997, pp. 289-296

[93] Krischer K., R. Rico-Martinez, J.G. Kevrekidis, H.H Rotenmund, G. Ertl, J.L Hudson, 'Model Identification of a Spatiotemporal Varying Catalytic Reaction', *American Institute of Chemical Engineers Journal*, **39**, 1993, pp.89-98

[94] Kronland-Martinet, R., Morlet, J., Grossman, A., *Int. J. Pattern Recognition and Artificial Intelligence,* Special Issue, *Expert System and Pattern Analysis, 1*, 1987, pp. 273-302

[95] Lewalle, J., 'Wavelet Transforms of the Navier-Stokes Equations and the Generalized Dimensions of Turbulence', *Applied Scientific Research,* 1993, **51**, pp. 109-113

[96] Li, H., Nozaki, T., 'Wavelet Analysis for the Plane Turbulent Jet', *JSME International Journal,* 1995, Series B,**38**(4) pp. 525-531

[97] Li, H., Nozaki, T., 'Application of Wavelet Cross-Coreelation Analysis to a Plane Turbulent Jet', *JSME International Journal,* 1997, Series B,**40**(1) pp. 58-66

[98] Liandrat, J., Moret-Bailly, F., 'Wavelet transform. Some applications to fluid dynamics and turbulence', *European Journal of Mechanics B-Fluids*, **9**(1), 1990 pp. 1-19

[99] Loève , M.M., 'Probability Theory', Princeton, N.J.: VanNostrand, 1955

[100] Lorenz, E.N., 'Empirical Orthogonal Functions and Statistical Weather Prediction', Cambridge: MIT, Department of Meteorology, Statistical Forecasting Project, 1956

[101] Lumley J.,'The structure of inhomogeneous turbulent flows', in *Proceedings of the International Colloquium on the Fine Scale Structure of the Atmosphere and its Influence on Radio Wave Propagation* (ed. A.M.Yaglam, V.I.Tatarsky), Doklady Akademii Nauk SSSR, Moscow, Nauka, 1967, pp. 166-178

[102] Lumley J.,'Stochastic Tools in Turbulence ', Academic Press, New York (1970)

[103] Lumley J. ,'Coherent structures in turbulence', In *Transition and Turbulence* (ed R.E. Meyer) (1981), pp. 215-241, Academic

[104] Mallat, S., 'A theory for multiresolution signal decomposition: the wavelet representation', *IEEE, Trans. on Pattern Anal. Machine Intell.,* **11**, 1989, p. 674

[105] Meneveau, C., Sreenivasan, K.R., 'The multifractal nature of turbulent energy dissipation', *Journal of Fluid Mechanics,* **224**, 1991, pp. 429-484

[106] Meneveau, Charles., 'Analysis of turbulence in the orthonormal wavelet representation', *Journal of Fluid Mechanics,* **232**, 1991, pp. 469-520

[107] Meneveau, C., 'Dual spectra and mixed energy cascade of turbulence in the wavelet representation', *Physical Review Letters* , **66**, 1991, pp. 1450-1453

[108] Mikhlin, S.G., 'Integral Equations', Pergamon Press, Oxford, 1957

[109] Moin, Moser ,'Characteristic-eddy decomposition of turbulence in a channel', *J. Fluid Mech.* (1989), **200** , pp. 471-509

[110] Morlet, J., 'Sampling theory and wave propagation', *Proc. 51st Annual International Meeting of the Society of Exploration Geophysicists,* 1981, Los Angeles.

[111] Morlet, D., Peyrin, F., Desseigne, P., Touboul, P., Rubel, P., 'Time-scale analysis of high-resolution signal-averaged surface ECG using wavelet transformation' *Computers in Cardiology*, Publ. by IEEE, Computer Society, Los Alamitos, CA, USA (IEEE cat n 92CH3116-1). pp. 393-396

[112] Moum, J.N., Kawall, J.G., Keffer, J.F., 'Structural features of the plane turbulent jet', *Physics of Fluid*, 1979, **22**(7), pp. 1240-1244

[113] Moum, J. N., Kawall, J. G. and Keffer, J. F.,'Coherent structures within the plane turbulent jet,' *Phys. Fluids*, 1983, **26** (10), pp. 2939-2945.

[114] Mumford, J.C., 'The structure of the large-scale eddies in fully developed turbulent shear flows. Part 1, the plane jet', *Journal of Fluid Mechanics,* 1982, **118**, pp. 241-268

[115] Oler, J.W., Goldschmidt, V.W., 'A vortex-street model of the flow in the similarity region of a two-dimensional free turbulent jet', *Journal of Fluid Mechanics,* 1982, **123**, pp. 523-535

[116] Orr, W.M., 'The stability or instability of steady motions in a liquid', *Proc. R. Irish Acad. A,* **28**, 1907, p. 259

[117] Otaguro, T., Takagi, S., Sato, H., 'Pattern Search in a turbulent signal using wavelet analysis', *Proc. 21st Japan Symp. on Turbulence*, Tokyo, Japan, 1989

[118] Payne, Lumley ,'Large eddy structure of the turbulent wake behind a circular cylinder', *Phys. Fluids* (1967), **10**(9, part 2), pp. 194-196

[119] Poje, A.C.; Lumley, J.L., 'Model for large-scale structures in turbulent shear flows', *Journal of Fluid Mechanics*, **285,** 1995, pp. 349-369

[120] Pouligny, B., Gabriej G., Muzy, J F., Arneodo, A., Argoul, F., Freysz, E., 'Optical wavelet transform and local scaling properties of fractals', *Journal of Applied Crystallography*, **24**(5), 1991, pp. 526-530

[121] Qin, F., Wolf, E.E, Chang, H.-C., Hwang, C.,'Controlling thermal front propagation on a catalityc water through video feedback', In *Proceedings of the American Control Conference*, **2**, 1993, p. 1302

[122] Rempfer, D.; Fasel, H.F., 'Evolution of three-dimensional coherent structures in a flat-plate boundary layer', *Journal of Fluid Mechanics,* **260**, 1994, pp. 351-375

[123] Reynolds, O., 'On the dynamical theory of turbulent incompressible viscous fluids and the determination of the criterion', *Phil. Trans. R. Soc. London A*, **186**, 1894, pp. 123-161

[124] Rodriguez, Sirovich,'Low-dimensional dynamics for the complex Ginzburg-Landau equation', *Physica D*, nonlinear phenomena (1990), **43**, MAY, 01, n.1 p.77

[125] Sarah, R.A., Liakopoulos, A., Gunes, H., 'Reduced dynamical models of nonisothermal transitional grooved-channel flow', *Phys. Fluids,* **9**(2), 1997, pp. 551-565

[126] Schmidt, E., 'Zur Theorie der linearen und nichtlinearen Integralgleichungen. I Teil: Entwicklung willkülicher Funktion nach Systemen vorgeschriebener', *Mathematische Annalen*, (1907), **63**, pp. 433-476

[127] Siggia, E., 'Original intermittency in fully developed turbulence', *Physical Review A,* **15**(4), pp. 1730-1750

[128] Sirovich, Rodriguez,'Coherent Structures and Chaos: a model problem', *Phys. Letters A* (1987), **120**(5), pp. 211-214

[129] Sirovich ,L, 'Turbulence and the Dynamics of Coherent Structure: I, II and III', *Quarterly Applied Mathematics*, (1987), **45**, p. 561

[130] Sirovich, Kirby, Winter ,'An eigenfunction approach to large-scale transitional structures in jet flow', *Phys. Fluids, A* (1990), **2**(2), pp.127-136

[131] Sirovich, Park ,'Turbulent thermal convection in a finite domain', *Phys. Fluids, A* (1990), **2**, pp. 1649-1668

[132] Spedding, G R., Browand, F K., Fincham, A M., 'Turbulence, similarity scaling and vortex geometry in the wake of a towed sphere in a stably stratified fluid' *Journal of Fluid Mechanics,* **314**(10), 1996, pp. 53-103

[133] Stewart, G.W.,'On the Early History of the Singular Value Decomposition', *SIAM Review*, (1993), **35**, pp.551-566 *Structure Identification in Free Turbulent Shear Flows*,1993 p. 239, Kluwer Academic Publishers

[134] Tangborn, Sirovich, Strett, 'An orthogonal decomposition of finite length chaotic Taylor-Couette flow', *Bull. Atm. Phys. Soc.* (1988), **33**, p .2242

[135] Tennekes, H., Lumley, J.L., 'A First Course in Turbulence', Cambridge: MIT Press, 1972

[136] Theodorsen T.,'Mechanism of turbulence', in *Proc. 2nd Midwestern Conf. on Fluid Mech.* (1952), Ohio State University, Columbia, OH

[137] Thomas. F.O., 'Structure of mixing layers and jets', *Applied Mechanics Review*, 1991, **44**(3), pp. 119-153

[138] Thomas. F.O., Brehob E.G., 'An investigation of large-scale structure in the similarity region of a two-dimensional turbulent jet', *Physics of Fluids,* , 1986, **29**, pp. 1788-1795

[139] Thomas, F.O., Goldschmidt, V.W., 'Structural Characteristics of a developing turbulent planar jet', J*ournal of Fluid Mechanics*, 1986, **163**, pp. 227-256

[140] Townsend A.,'The structure of turbulent shear flow', Cambridge University press, 1952

[141] Ukeiley, L., Varghese, M., Glauser, M., Valentine, D., 'Multifractal analysis of a lobed mixer flowfield utilizing the proper orthogonal decomposition', *AIAA Journal,* **30**(5), 1992, pp. 1260-1267

[142] Ukeiley, L., 'Dynamics of large scale structures in a plane turbulent mixing layer', Ph.D dissertation, Clarkson University, 1995, Report # MAE-311

[143] Vasilyev, O.V., Yuen, D.A., and Paolucci, S., 'The Solution of PDEs Using Wavelets', Computers in Physics, **11**(5), 1997, pp. 429-435.

[144] Walker, S.W., Gordeyev, S.V., Thomas, F.O., 'A wavelet transform analysis applied to unsteady aspects of supersonic jet screech resonance', *Experiments in Fluids,* **22**, 1997, pp. 229-238

[145] Weir, A. D., Wood, D. H. and Bradshaw, P.,'Interacting turbulent shear layers in a plane jet,' *J. Fluid Mech.,* 1981, **107**, pp. 237-260.

[146] Wiktorsson, M., Lindoff, B., Johansson, B., Soderberg, F., 'Wavelet analysis of in-cylinder LDV velocity measurements', *Diagnostics and Modeling in SI Engines SAE Special Publications*, **1212**, 1996. SAE, Warrendale, PA, USA. pp. 1-10

[147] Winant, Drowant, 'Vortex pairing: the mechanism of turbulent mixing-layer growth at moderate Reynolds number', *J. Fluid Mech* (1974), **63**, p

[148] Wygnanski, I., Gutmark, E., 'Lateral motion of the wo-dimensional jet boundaries', *Physics of Fluid* (1971), **14**(7), pp. 327-361

[149] Zimin, V.D., 'Hierarchical model of turbulence', *Izvestia Academy of Science USSR, Atmospheric and Ocean Physics*, **17**(12), 1981, pp. 941-949

[150] Zimin, V., Hussain, F.,'Wavelet based model for small-scale turbulence', *Physics of Fluids*, **7**(12), 1995, pp. 2925-2927 237